

CONTENTS

	Page	
SUMMARY	1	1/A5
INTRODUCTION	1	1/A5
TRANSMITTER EXPERIMENT PACKAGE	2	1/A6
Output Stage Tube	2	1/A6
Power-Processing System	3	1/A7
Variable-Conductance Heat-Pipe System	4	1/A8
TEP Position in Spacecraft	5	1/A9
THERMAL ANOMALIES	5	1/A9
Normal Operating Characteristics	6	1/A10
Anomaly of Day 75	8	1/A12
Anomaly of Day 82	10	1/A14
Anomaly of Day 101	11	1/B1
Anomaly of Day 253	13	1/B3
Similarities and Comparisons	13	1/B3
Reasons for Concern	14	1/B4
STUDIES AND FINDINGS	15	1/B5
Room-Ambient OST Tests	16	1/B6
Computer Studies	17	1/B7
Thermal-Vacuum OST Tests	17	1/B7
CTS In-Orbit Tests	20	1/B10
Room-Ambient VCHPS Tests	21	1/B11
Study of a TEP Anomaly in Progress	23	1/B13
Contractual Investigation	24	1/B14
Analysis of Thermal-Anomaly Transient Behavior	25	1/C1
Assessment of Anomaly Causes	29	1/C5
SUMMARY AND CONCLUSIONS	32	1/C8
APPENDIXES		
A - MAJOR-ACTIVITIES CHRONOLOGY OF CTS TEP THERMAL ANOMALY INVESTIGATING COMMITTEE	38	1/C14
B - TEMPERATURE EFFECTS ON FOCUS MAGNETS	40	1/D2
C - THERMAL OUTPUT OF OST 2022R1 AND OST 2030	45	1/D7
REFERENCES	47	1/D9

Item 830-H-15

NAS 1.60: 1410

APR 11 1979

NASA Technical Paper 1410

COMPLETED
ORIGINAL

Thermal Anomalies of the Transmitter Experiment Package on the Communications Technology Satellite

Robert E. Alexovich and Arthur N. Curren

APRIL 1979

NASA

NASA Technical Paper 1410

Thermal Anomalies of the
Transmitter Experiment Package
on the Communications
Technology Satellite

Robert E. Alexovich and Arthur N. Curren
Lewis Research Center
Cleveland, Ohio



National Aeronautics
and Space Administration

**Scientific and Technical
Information Office**

1979

Blank
Page

SUMMARY

This report details an investigation of the causes of four temporary thermal-control-system malfunctions that gave rise to unexpected temperature excursions in the 12-gigahertz, 200-watt transmitter experiment package (TEP) on the Communications Technology Satellite.

The TEP consists of a nominal 200-watt output stage tube (OST), a supporting power-processing system (PPS), and a variable-conductance heat-pipe system (VCHPS). The VCHPS, which uses three heat pipes to conduct heat from the body of the OST to a radiator fin, was designed to maintain the TEP at safe operating temperatures at all operating conditions.

On four occasions during 1977, all near the spring and fall equinoxes, the OST body temperature and related temperatures displayed sudden, rapid, and unexpected rises above normal levels while the TEP was operating at essentially constant, normal conditions. The temperature excursions were all terminated without TEP damage by reducing the radiofrequency (rf) output power of the OST. Between the anomalies and since the fourth, the thermal control system has apparently functioned as designed.

The results of the investigation indicate the most probable cause of the temperature anomalies is depriving of the arteries in the variable-conductance heat pipes. Further, a mode has been identified in which the TEP, as presently configured, may operate with stable temperatures and with minimum change in performance level.

INTRODUCTION

The Communications Technology Satellite (CTS) was developed in a joint U.S.-Canadian program by NASA and the Canadian Department of Communications (DOC). It was launched by NASA on January 17, 1976. One of the major responsibilities of the United States in the joint program was to provide a 200-watt, 12-gigahertz, 50-percent-efficient high-power transmitter for the spacecraft. A transmitter experiment package (TEP) was provided. It consisted of the output stage tube (OST), the power-processing system (PPS), and the variable-conductance heat-pipe system (VCHPS).

On day 75 of 1977 (Mar. 16) at 19:25 GMT, the OST temperature near the rf output port unexpectedly began to increase rapidly. The body temperature of the OST rose from the normal of 56° C to 75° C at 19:44 GMT. At that time the rf output power was reduced and the body temperature of the OST returned to a safe level. There have been three other similar thermal anomalies - on days 82, 101, and 253 in 1977.

On April 23, 1977, a committee was established to investigate the anomalous in-orbit thermal performance of the TEP. This committee was charged with

- (1) Identifying the probable cause or causes of the anomalous behavior
- (2) Assessing the impact on future performance
- (3) Recommending actions necessary to insure the continued operating capability of the TEP

The thermal anomaly investigating committee was composed of the following representatives of the Communications Research Centre (CRC) of Ottawa and the Lewis Research Center of Cleveland: R. Alexovich - Lewis, Chairman; D. Caswell - CRC; D. Connolly - Lewis; A. Curren - Lewis; E. Edelman - Lewis; L. Gedeon - Lewis; J. Matsushita - CRC; and W. Payne - CRC.

This report details the results of the investigation and the conclusions reached. A chronology of the major activities undertaken by the committee is given in appendix A. Appendixes B and C, by Denis J. Connolly, describe temperature effects on OST magnets and examine the OST body-heat-rejection characteristics.

TRANSMITTER EXPERIMENT PACKAGE

The TEP (ref. 1) is used in the CTS spacecraft transponder to amplify rf output power in the frequency band 12.038 to 12.123 gigahertz. It consists of a nominal 200-watt OST, a supporting PPS, and a VCHPS.

Output Stage Tube

The OST (ref. 2) is a coupled-cavity traveling-wave tube (TWT) that is augmented with a multistage depressed collector (MDC), as shown schematically in figure 1. This class of linear-beam microwave amplifier converts the kinetic energy of an electron beam into rf energy.

An electron beam is formed by convergent optics in the electron gun. The electrons pass through an interaction region of the TWT located between the input and output waveguides. This region of the TWT is composed of cylindrical cavities that are coupled to form a lumped-element transmission line, or slow-wave structure. It contains three line sections separated by terminations (or severs). The beams are focused by magnets placed outside the cavity structure along the transmission line. As the beam exits from the coupled-cavity region of the TWT, it enters the multistage depressed collector (ref. 3). The MDC is used to convert the kinetic energy remaining in the electron beam to potential energy and thus reduce the externally supplied power required to operate the TWT.

Heat produced in the MDC by the residual velocities of the collected electrons is radiated to the collector enclosure and reradiated to space. A combination of internal heat shields and a bellows type of external heat choke is used to reduce the heat flow back to the interaction section of the TWT. Heat produced in the body of the OST can be classified as that associated with the input region and that associated with the output region. The following component losses contribute to the heat produced in the body: cathode heater power, which produces heat in the input region; body current losses, which are a function of rf output power and are divided between the input and output regions; sever losses, which are proportional to rf output and occur at each sever, with the largest part in the output region; and skin-effect losses, which vary exponentially along the OST circuit, are proportional to rf output power, and appear predominantly in the output region of the OST. In addition, there are output window losses and skin-effect losses in an output directional coupler that contribute to output-region-produced heat. The distribution of losses as a function of OST rf output power is determined in appendix C.

The thermal conducting path for removal of OST body heat is shown in figure 2. The OST is supported by an input and an output saddle. The output saddle is larger because skin-effect and beam interception losses are largest in this region of the OST body. The saddles are mounted on the OST baseplate, which then is mounted on the heat-pipe saddle. The whole assembly is finally mounted on the PPS baseplate and the south panel of the spacecraft. Section AA of figure 2 is detailed in figure 3, which shows the conducting paths from the OST body to the heat-pipe saddle and the spacecraft south panel. The thermal interface between the copper bus and the aluminum saddle and that between the aluminum saddle and the OST baseplate are indium-foil shims. The remaining interfaces are RTV silicone elastomer, as shown.

Temperature sensors are located as shown in figure 2: two on the MDC enclosure, one on the TWT body, and one on the output coupler (not shown). The temperature sensors that indicated the abnormally high temperatures during each anomaly are those near the OST output port. In addition to temperature measurements, sufficient electrical measurements were made to determine direct-current electrical input power, beam interception on the body of the OST, and rf output power. A complete list of TEP measurements is given in table I.

Power-Processing System

Electrical power for operating the TEP is delivered to the PPS from the spacecraft bus at nominal supply voltages of 76 and 27.5 volts dc. The PPS (ref. 4) performs the following functions for TEP operation:

- (1) Develops proper operating voltages for the TWT and MDC
- (2) Regulates supply voltages
- (3) Provides fault sensing and protection
- (4) Provides command, control, and sequencing for remote operation.

An exploded schematic of the PPS package is shown in figure 4. The package has outgassing vents in the top cover and side as shown. The high-voltage and low-voltage sections are separated within the package. Heat developed within the PPS is conducted to the TEP baseplate and to the spacecraft south panel. PPS temperatures are measured in two places: on a component board within the PPS and on the PPS baseplate. Electrical measurements are made of the 76-volt dc bus voltage and input current, the 27.5-volt dc supply voltage, and the reference voltage used for all TEP temperature sensors.

Variable-Conductance Heat-Pipe System

The VCHPS (ref. 5) removes heat from the TWT and controls the temperatures of all operating and nonoperating levels of the OST for the range of solar thermal input encountered. The VCHPS (fig. 5) consists of the heat-pipe evaporator saddle; three variable-conductance, gas-loaded heat pipes; the radiator; and the support structure. The plane of the radiator is parallel to the orbital plane. The VCHPS radiator is attached to the spacecraft by means of four struts and four attachment fittings, all of which are designed to thermally isolate the radiator from the spacecraft.

The internal structure of the heat pipes is shown in figures 6 and 7. The pipes are 1.27-centimeter- (0.50-in.-) outside diameter stainless-steel tubes with a 0.07-centimeter- (0.028-in.-) thick wall. The tube is internally threaded with 40 threads per centimeter (100 threads/in.). There is a stainless-steel felt wick 0.127 centimeter (0.050 in.) thick across the inner diameter, with stainless-steel arteries 0.160 centimeter (0.063 in.) in inside diameter attached as shown. Under normal operation at saturated power, 90 percent of the heat-transfer liquid is carried by the arteries. Priming foils, attached to the artery-wick assembly (as shown in fig. 6) and located in the evaporator end of the pipes, are used to vent entrapped gas from inside the arteries. The priming foils are 0.00127-centimeter- (0.0005-in.-) thick stainless steel with 0.0254-centimeter- (0.010-in.-) diameter holes. The heat-pipe saddle is made of aluminum and soldered to the pipes.

The variable-conductance heat pipes are filled with methanol as a working fluid and with a mixture of 90-percent nitrogen and 10-percent helium as a control gas. The gas load in each pipe is adjusted so that the individual heat pipes begin to conduct at progressively higher levels of pipe temperature. The expected performance of the VCHPS is given in figure 8. For steady-state operation at saturation, the body of the OST

rejects 155 watts of heat to produce an expected saddle temperature of approximately 37° C at equinox. The saddle temperature increases with increasing Sun illumination of the radiator. The expected performance at the summer solstice is also shown in figure 8. There are six temperature sensors on the variable-conductance heat pipes, as shown in figure 5. There are three sensors on the adiabatic section of the heat pipes (HP1T, HP2T, and HP3TA).¹ There are three sensors on heat pipe 1: one on the condensor region (HP4T), one at the gas-reservoir end (HP5T), and one on the gas reservoir (HP6T).

TEP Position in Spacecraft

The TEP is mounted within the spacecraft on the south panel, as shown in figure 9. The OST is mounted on the evaporator saddle of the VCHPS, which in turn is mounted on the spacecraft south panel. The OST is positioned so that the multistage depressed collector enclosure protrudes through the aft section of the spacecraft for direct thermal radiation to space from the collector enclosure.

THERMAL ANOMALIES

During 1977 there were four TEP thermal anomalies. There were three anomalies during the eclipse season of the vernal equinox - on days 75, 82, and 101 - and one anomaly during the eclipse season of the autumnal equinox - on day 253. All anomalies exhibited the same general characteristics. Temperatures near the rf output unexpectedly began to increase. The OST operation before and during the temperature rise was constant. There were no changes in electrical input power or rf output power during this time. The OST had reached thermal equilibrium before each thermal anomaly temperature rise. During the thermal anomalies on days 75, 82, and 101, temperatures continued to rise until the rf output power was reduced, at which time temperatures dropped to safe operating limits. The thermal anomaly of day 253 was used to investigate the TEP behavioral response. The operating power profile was controlled during the anomaly rather than simply reduced to minimum rf output. The anomaly characteristics of day 253 differ from those of the preceding three anomalies and are discussed separately in a later section, Study of a TEP Anomaly in Progress. The TEP has fully recovered after each anomaly and exhibits no signs of change or permanent performance degradation.

¹The temperature of the adiabatic section of heat pipe 3 is given as HP3TA to distinguish these data from earlier, improperly processed data for this sensor, which had been designated HP3T.

Data are presented for a normal operating day to serve as a basis for comparison. Similarities and differences between anomalies are discussed, along with reasons for concern.

Normal Operating Characteristics

Data from a normal day for this period, day 89 (Mar. 30), are presented as a basis for comparison. For day 89, two contiguous time segments of data are presented. The first time segment (fig. 10) shows the normal thermal environment of the TEP. The segment begins at 00:00 GMT and extends through 11:30 GMT, a time period during which none of the anomalies occurred. The second time segment presented (fig. 11) corresponds to the $11\frac{1}{2}$ -hour period during which the anomalies occurred on days 75, 82, 101, and 253. The second time segment begins at 11:30 GMT and extends through 23:00 GMT.

During the first time segment (fig. 10), there was a loss of data from 2:00 to 3:10 GMT and again at 9:10 GMT. Figures 10(a) to (c) show the temperatures near the OST rf output port. These temperatures, from 00:00 to 2:00 GMT, were determined by body losses of the OST and the OST thermal control system. They responded to changes in OST operating level, which was from 2 to 55 watts rf output during the period. The temperatures near the OST rf output port fell exponentially to an equilibrium temperature at 7:20 GMT. At this time, temperatures again began to fall in response to the start of spacecraft eclipse by the Earth. At 8:50 GMT, temperatures began to rise after the eclipse and continued to rise slowly until 10:57 GMT, when OST operation was started. Figures 10(d) to (f) show the input power to the OST, the rf output power as measured by a diode detector in the output coupler, and the body current, respectively. At some point during the period of data loss, the OST was shut down and operation was not restarted until 10:57 GMT. During the nonoperating period of the OST, the internal losses and the electrical input power, which was supplied to the cathode heater, were reduced to 3 watts.

The heat-pipe temperatures (figs. 10(g) to (l)) exhibited normal behavior from 00:00 to 11:30 GMT. The adiabatic temperatures of heat pipes 1, 2, and 3 (figs. 10(g), (h), and (i), respectively) showed that only heat pipe 1 reached an operating temperature where the heat pipe was active. This condition existed during the two plateau regions of 26° and 27.5° C (fig. 10(g)). Heat pipes 2 and 3 (figs. 10(h) and (i)) did not exhibit pipe conduction and remained between -25° and -15° C. The active length of heat pipe 1 did not reach the HP4T sensor, which is located on the condenser length of heat pipe 1 (fig. 10(j)). It remained below the usable range of the sensor until after 3:10 GMT. The small radiator area required was consistent with the low level of OST body losses at an rf output power of 55 watts or less. Sensors HP5T and HP6T (figs. 10(k)

and (l)) are located at the gas-reservoir end of heat pipe 1 and on the gas reservoir, respectively. They are far removed from the active length of the heat pipe and so do not respond to changes in OST operation. They reach minimum temperatures of -102° and -75° C, respectively.

During the OST nonoperating period, all heat-pipe temperatures (figs. 10(g) to (l)) responded similarly to the same stimulus. The temperatures of heat-pipe systems increased slowly as the Earth-viewing face of the spacecraft turned toward the Sun. As the spacecraft turned, Sun illumination of the radiator increased because of increased reflection from the Earth-viewing face. At 7:15 GMT the spacecraft entered the Earth's shadow. The adiabatic and condensor temperatures (figs. 10(g) to (j)) fell rapidly, reaching minimums at 8:21 GMT, the end of the eclipse. Sensor HP4T (fig. 10(j)) again exceeded its useful range. The gas-reservoir end and gas-reservoir temperatures of heat pipe 1 (figs. 10(k) and (l), respectively) increased slowly because of the reflected illumination from the Earth-viewing face of the spacecraft, reaching maximums of -34° and -20° C, respectively. At 7:15 GMT, temperature HP5T fell rapidly as the spacecraft entered the penumbra. It reached a minimum of -92° C when the spacecraft left the umbra at 8:19 GMT and rose again to a maximum of -42° C at 9:40 GMT. This increase was due to reflected radiation from the spacecraft Earth-viewing face. At 5:40 GMT, HP6T (fig. 10(l)) reached a maximum of -20° C and fell slowly as the gas reservoir of heat pipe 1 was shadowed by the gas reservoir of heat pipe 2. At 7:15 GMT, the temperature began to fall rapidly because of the Earth eclipse. It reached a minimum of -70° C when the heat input to the gas reservoir equaled the losses. This occurred at 8:40 GMT, 19 minutes after the end of the eclipse. The gas-reservoir temperature rose to a maximum of -52° C at 10:30 GMT.

Data for the second time segment of day 89 are presented in figure 11. The temperatures near the OST rf output port responded to changes in internal OST losses that were a function of rf output power. The temperatures near the OST rf output port (figs. 11(a) to (c)), as well as rf output power (fig. 11(e)) and OST body current (fig. 11(f)) normally followed changes in electrical input power. The electrical input power profile (fig. 11(d)) varied from day to day, being determined by communications operations. Note that OST body temperature (fig. 11(a)) changed only in response to changes in TEPP (input electrical power). Its response resembled that of a first-order system with a time constant of 24 minutes and reached a maximum of 55° C.

The adiabatic heat-pipe temperature HP1T, HP2T, and HP3TA (figs. 11(g) to (i)) rose sequentially as each heat pipe began to conduct its share of the thermal load. They reached operating temperatures of 27° , 31° , and 32° C, respectively, with small changes reflecting varying heat load. The increase in HP4T (fig. 11(j)) followed the increase in HP1T. It occurred as the warm front separating the active and inactive lengths of the pipes passed the HP4T sensor.

Sensors HP5T and HP6T measure the temperatures at the gas-reservoir end of heat pipe 1 and in the gas reservoir, respectively. These data are shown in figures 11(k) and (l). As the shadow created by the east edge of the spacecraft progressed across the VCHPS radiator, temperatures HP5T and HP6T fell, with HP5T falling at a lesser rate until 15:10 GMT. The drop in temperature was interrupted by three observable plateaus beginning at 15:10, 18:20, and 20:30 GMT with temperatures of -84° , -90° , and -102° C, respectively. The last plateau was due to the range limitation of the measurement channel. The changes in rate of HP5T and specifically the first two plateaus were due to changes in the active length of heat pipe 1 that were caused by changes in OST operating level. The temperatures began to rise as the shadow created by the west edge of the spacecraft began to recede, exposing the gas reservoirs and the gas-reservoir ends of the heat pipes first. This sequence occurred as the spacecraft progressed from the 180° orbital position to 270° , as shown in figure 12.

The resolution determined by quantizing heat-pipe adiabatic section temperatures HP1T, HP2T, HP3TA, and HP4T near 30° C is 1.5 degrees C. This would, in the absence of noise, limit the resolution of these measurements. It has been observed that when a measurement is between quantizing levels, its mean value can be interpreted for a given period from the ratio of the fractional time spent at the higher quantizing level to that spent at the lower one. Noise, with zero mean and independent of the quantizing rate, superimposed on the measurement value produces this result. This effect is applicable to all the analog measurements presented in this paper. This method of interpretation was used in assessing the differences between HP3TA and HP1T discussed for days 89, 75, 82, 101, and 253 in the section Similarities and Comparisons.

Anomaly of Day 75

On day 75 of 1977 (Mar. 16) at about 19:25 GMT, with the TEP operating at essentially constant conditions, temperatures near the OST rf output port unexpectedly began to rise. This was the first of the TEP thermal anomalies. The performance and operating characteristics of the TEP for that day are presented graphically in two contiguous time segments of data: The first segment (fig. 13) covers the time period preceding the anomaly, from 00:00 to 11:30 GMT. The second segment (fig. 14) covers the time period containing the anomaly, from 11:30 to 23:00 GMT.

From 00:00 GMT until the start of the eclipse, 7:17 GMT, temperatures near the OST rf output port slowly decreased. These temperatures - the OST body temperature (BODY), figure 13(a); the output waveguide coupler temperature (CPLR), figure 13(b); and the MDC flange temperature (TMDC2), figure 13(c) - reached minimums of 25° , 23° , and 17° C, respectively, before the eclipse. During the eclipse, these temperatures fell rapidly to 9° , 12° , and 3° C, respectively. The TEP was operated only once

from 00:00 to 11:30 GMT on day 75. OST input electrical power (TEPP), figure 13(d); rf output power as indicated by a diode detector in the output waveguide (FRWD), figure 13(e); and OST body current (BODY), figure 13(f) all were zero until 9:05 GMT. The TEP was operated briefly at that time to verify performance after the eclipse.

The VCHPS temperatures (figs. 13(g) to (l)) exhibited normal behavior from 00:00 to 11:30 GMT on day 75. The adiabatic section temperatures of heat pipes 1 (HP1T), 2 (HP2T), and 3 (HP3TA) are shown in figures 13(g), (h), and (i), respectively. Only heat pipe 1 was active and conducting heat during the 11½-hour period. Figure 13(g) indicates HP1T was above 25° C from 00:00 until 1:45 GMT. During this time, HP2T and HP3TA (figs. 13(h) and (i)) remained between -22° and -17° C, indicating that heat pipes 2 and 3 were not active. The active length of heat pipe 1 did not reach sensor HP4T on the condenser portion of heat pipe 1, the temperature of which is shown in figure 13(j).

From 3:00 to 11:30 GMT, all the VCHPS temperatures (figs. 13(g) to (l)) behaved similarly. Temperatures were determined predominantly by spacecraft orbital motion and Sun illumination - not by TEP operation. Temperatures of the heat-pipe system increased slowly as the spacecraft moved from the 270° orbital position to 0°, as shown in figure 12. The Earth-viewing face of the spacecraft turned toward the Sun from 1:50 to 7:17 GMT, and Sun illumination of the radiator increased because of the increased reflection from the Earth-viewing face. At 7:17 GMT, the spacecraft entered the penumbra of the Earth's shadow, and the heat-pipe adiabatic section temperatures (figs. 13(g) to (i)) and the condenser temperatures (figs. 13(j) and (k)) fell rapidly. The adiabatic section temperatures reached a minimum of -35° C and rose slowly after eclipse to 0° C. The gas-reservoir condenser temperature for heat pipe 1, HP5T, dropped rapidly during eclipse to a minimum of -95° C at 8:29 GMT, the end of the eclipse. At 10:00 GMT, HP5T had risen to a maximum of -38° C. The gas-reservoir temperature for heat pipe 1, HP6T (fig. 13(l)) rose slowly to a maximum of -23° C at 5:50 GMT and began to drop slowly as the gas reservoir of heat pipe 1 was shadowed by the reservoir of heat pipe 2. At 7:17 GMT, HP6T began to fall rapidly as a result of Earth-eclipse shadowing to a minimum of -70° C after the eclipse and then rose to a maximum of -41° C at 11:10 GMT.

TEP performance and operating characteristics from 11:30 to 23:00 GMT on day 75 are shown in figure 14. Figures 14(a) to (c) present the time-temperature profiles for the OST body, the waveguide coupler, and the MDC flange, respectively, for this period. At 19:25 GMT, the body temperature began to increase from its normal operating level of 56° C to 75° C at 19:44 GMT. At that time, the OST rf output power was reduced and the body temperature dropped to 70° C by 20:07 GMT. The OST dc input power history for the same period is shown in figure 14(d). From 15:15 to 19:44 GMT when rf power was reduced, the input power was essentially constant at 437 watts. Radiofrequency output power and OST body current (figs. 14(e) and (f)) were also constant during this

period at 2.9 volts (corresponding to 198 W) and 5.2 milliamperes, respectively.

The adiabatic section temperatures of heat pipes 1, 2, and 3 sequentially increased from 14:00 to 17:00 GMT, with the increase in HP1T preceding that in HP2T and the increase in HP2T preceding that in HP3TA (figs. 14(g) to (i)). Temperatures HP1T, HP2T, and HP3TA reached operating levels of 29° , 31° , and 33° C, respectively, and changed only slightly until 18:00 GMT, when HP3TA decreased in response to reduced heat input. Temperature HP4T rose as the warm vapor front passed the sensor location (on the condensing length of heat pipe 1, fig. 14(j)) but remained essentially constant until 18:00 GMT, when it dropped in response to reduced OST losses.

Temperatures HP5T and HP6T (on the gas-reservoir end of heat pipe 1 and on the gas reservoir, respectively, figs. 14(k) and (l)) fell during this period, with HP6T lagging HP5T. Both temperatures reached minimums of -98° C before the unstable increase in OST temperatures began. Temperature HP6T began to increase at 21:47 GMT, well after the anomaly had occurred.

Anomaly of Day 82

On day 82 of 1977 (Mar. 23) at 18:01 GMT the second thermal anomaly was experienced by the TEP. The performance and operating characteristics of the TEP for that day are presented graphically in two contiguous time segments of data: The first segment (fig. 15) covers the period 00:15 to 11:30 GMT, when a number of data losses occurred - from 00:15 to 2:45 GMT and at 4:58 GMT. The second segment (fig. 16) contains the thermal anomaly period and extends from 11:30 to 23:00 GMT.

Temperatures near the OST rf output port - specifically body, coupler, and MDC flange temperatures - are shown in figures 15(a) to (c), respectively. From 00:15 to 1:30 GMT, because of the very low level of rf output, the body and coupler temperatures were 35° C and the MDC flange temperature was 45° C. The input electrical power to the OST (fig. 15(d)) was 180 watts. The rf output diode detector (fig. 15(e)) indicated 0.4 volt, which corresponds to an OST rf output power of 10 watts, while the OST body current was 1.5 milliamperes (fig. 15(f)). During the remainder of the period, from 1:30 to 11:30 GMT, the TEP was not operated, so the temperatures were independent of any operating losses. The body, coupler, and MDC flange temperatures dropped slowly from their low operating levels to 23° , 23° , and 15° C, respectively, before the eclipse. During the eclipse, these temperatures decreased more rapidly and reached minimums of 8° , 10° , and 2° C, respectively.

Heat-pipe adiabatic section temperatures HP1T (fig. 15(g)), HP2T (fig. 15(h)), and HP3TA (fig. 15(i)) did not reach levels that would indicate active heat conduction. This situation is normal for the limited TEP operation noted on day 82. These adiabatic section temperatures responded to changing Sun illumination as expected and rose to a

maximum of 2.5°C at 7:15 GMT but then fell rapidly during the eclipse. They reached a minimum of -37°C at 8:33 GMT. Following the eclipse, the adiabatic section temperatures increased to about -2°C at 11:30 GMT.

Heat-pipe-1 condenser section temperatures HP4T (fig. 15(j)) and HP5T (fig. 15(k)) responded similarly to the adiabatic section temperatures. The maximums for HP4T and HP5T before eclipse were -27°C and -35°C , respectively. During eclipse, HP5T fell to -95°C and rose to a maximum of -42°C after the eclipse. Heat-pipe-1 gas-reservoir temperature HP6T (fig. 15(l)) also responded as expected. It reached a maximum before the start of the Earth eclipse from shadowing by the reservoir of the adjacent heat pipe. During the eclipse HP6T fell to -72°C and increased to a maximum of -50°C by 11:05 GMT.

As stated earlier, the thermal anomaly began at 18:01 GMT, when temperatures near the OST rf output port began to rise rapidly. Figures 16(a) to (c) show the time-temperature profiles of the OST body, output coupler, and MDC flange for this period. The OST body temperature increased from 50°C to 63°C at 19:04 GMT. Radiofrequency output power was reduced at that time and the body temperature dropped to 61°C by 19:10 GMT. The temperatures then stabilized and remained within normal limits for the balance of the operating day. From 17:01 GMT through the unstable temperatures period, the dc electrical input power to the OST (fig. 16(d)), the rf output power (fig. 16(e)), and the OST body current (fig. 16(f)) were constant at 401 watts, 2.6 volts (corresponding to 171 W of rf output power), and 4.4 milliamperes, respectively.

Heat-pipe adiabatic section temperatures HP1T (fig. 16(g)), HP2T (fig. 16(h)), and HP3TA (fig. 16(i)) were essentially constant after initially rising to active levels and displayed only small variations about means of 26°C , 27°C , and 31°C , respectively. Heat-pipe-1 condensing section temperature HP4T (fig. 16(j)) was essentially constant at 25.5°C from 17:32 to 21:43 GMT. Temperatures HP5T (fig. 16(k)) and HP6T (fig. 16(l)) reached a minimum of -102°C before the anomaly began and remained at that level throughout the anomaly.

Anomaly of Day 101

The third thermal anomaly experienced by the TEP was on day 101 of 1977 (Apr. 11). As with the first two anomalies, the performance and operating characteristics of the TEP for that day are presented graphically in two contiguous time segments of data: The first segment (fig. 17) covers the time period 00:00 to 11:30 GMT. During this period, there occurred several short data-loss intervals characterized by sharp spikes on the curves. (The data from 3:00 to 4:10 GMT are not available.) The second

segment (fig. 18) covers the time period during which the anomaly took place, from 11:30 to 23:00 GMT.

From 00:00 to 11:30 GMT, the temperatures near the OST rf output port were relatively stable. The temperatures of the OST body, output waveguide coupler, and MDC flange (figs. 17(a) to (c), respectively) were only slightly perturbed by the very short eclipse period, from 7:25 to 8:00 GMT. OST dc electrical power input, TEPP; rf output power, FRWD; and OST body current, BODY, for the period 00:00 to 11:30 GMT are presented in figures 17(d) to (f), respectively. As indicated, there was no TEP operation during that time. With no self-heating, the heat-pipe adiabatic section temperatures all increased very slowly from a minimum of -25°C to 6°C . These temperatures - HP1T, HP2T, and HP3TA - are shown in figures 17(g) to (i), respectively. The temperatures increased as the spacecraft rotated from the 270° orbital position to 60° (fig. 12). The slow increase in temperature was interrupted by the short eclipse period. Heat-pipe-1 condenser temperature HP4T and HP5T (figs. 17(j) and (k), respectively) and the gas-reservoir temperature HP6T (fig. 17(l)) behaved like the adiabatic section temperatures. The minimums for all these temperatures were below -50°C .

The third TEP thermal anomaly began at 18:43 GMT on day 101. At that time, temperatures near the OST rf output port unexpectedly began to rise. Figures 18(a) to (c) present the time-temperature profiles for the OST body, the waveguide coupler, and the MDC flange, respectively. With essentially unchanged OST operating conditions, the OST body temperature (fig. 18(a)) rose to 70°C at 18:56 GMT. At 19:00 GMT, the OST rf output power was reduced to zero. The body temperature continued to rise briefly, peaking at about 73°C at 19:02 GMT before starting to fall. By 19:15 GMT, the temperature had fallen to about 60°C , and TEP operation was resumed at about 110 watts of rf output power at 12.080-gigahertz center-band frequency. The body temperature continued to drop at these operating conditions, reaching about 57°C at 19:21 GMT, where it stabilized and remained within the normal range during the balance of the operating day.

From 17:03 GMT through the period of unstable OST temperatures (to 19:00 GMT), the OST dc electrical input power, the rf output power, and the OST body current (figs. 18(d) to (f)) were constant at 450 watts, 2.9 volts (corresponding to 202 W of rf output power), and 5.7 milliamperes, respectively. The data dropout at 20:33 GMT was due to an interruption in telemetry transmission at that time. Heat-pipe adiabatic section temperatures HP1T, HP2T, and HP3TA (figs. 18(g) to (i), respectively) were essentially constant after initial turnon, displaying only small variations about means of 28° , 29° , and 33°C , respectively. These temperatures remained at these values until well after the unstable OST temperature (anomaly) period. The heat-pipe-1 condenser temperature HP4T (fig. 18(j)) was constant at 28°C from 15:23 GMT until loss of telemetry transmission.

Heat-pipe-1 condenser and gas-reservoir temperatures HP5T and HP6T (figs. 18(k) and (l), respectively) fell to -98° and -102° C, respectively, before the OST temperature anomaly period and remained at those levels until data loss occurred at 20:33 GMT.

Anomaly of Day 253

The TEP thermal anomaly of day 253 is described in a later section of this paper, Study of a TEP Anomaly in Progress.

Similarities and Comparisons

All the TEP thermal anomalies have had some commonality of occurrence and have exhibited the following similar characteristics:

(1) All the anomalies have occurred during the spacecraft Earth-eclipse seasons of the year. Figure 19 shows the time of occurrence within the eclipse seasons, along with the Sun angle with respect to the spacecraft orbital plane, for each anomaly.

(2) All the anomalies have occurred between 14:20 GMT (day 253) and 19:25 GMT (day 75) while the spacecraft was in the 90° -to- 180° orbital quadrant. Figure 20 shows the orientation of the spacecraft with respect to the Sun for each anomaly.

(3) All the anomalies have occurred after the gas-reservoir end of heat pipes 1 and 2 became shadowed by the body of the spacecraft. This shadowing occurred when the Sun angles with respect to the spacecraft orbital plane (and therefore the radiator plane) were between -2° and 8.1° , as indicated in figures 19 and 20. The heat-pipe radiator is shadowed by the spacecraft body for orbital positions between 90° and 270° at all Sun angles greater than -3° , as indicated by the configuration detailed in figure 21. The observed magnitude of spacecraft roll about the axis parallel to the south and Earth-facing panels was less than $\pm 1^{\circ}$.

(4) All the anomalies have been preceded or accompanied by an abnormal difference in the temperatures of the adiabatic sections of heat pipes 3 and 1 (HP3TA and HP1T, respectively). For convenience, this temperature difference has been plotted separately for this report and is designated as HP31A on the figures. Figure 22(a) shows HP31A for the period 11:30 to 23:00 GMT on day 89, a "normal" day. Note that, for the normal day, HP31A did not exceed 4 degrees C during the entire period. Figures 22(b) to (e) present the HP31A time profile for the period 11:30 to 23:00 GMT (approximately) on the anomaly days 75, 82, 101, and 253, respectively. At point A in each figure, HP31A increased from its previous level to an abnormal value of 3.9 degrees C. At point B, HP31A increased to between 4 and 5.6 degrees C. Then at point C, which corresponds

to the beginning of the unstable OST temperature (anomaly) period, HP31A decreased to about 4 degrees C. An intensive review of all the CTS flight telemetry data throughout the vernal and autumnal spacecraft eclipse seasons and the intervening period (days 55 to 288, 1977) confirmed the normal characteristics and the anomaly period similarities. It was, in fact, this data review and the recognition of the anomaly period similarities of days 75 and 101 that led to the discovery of the anomaly of day 82, which had not been noticed previously. This anomaly had apparently been terminated fortuitously without TEP damage in the normal schedule of operations on day 82.

(5) All the anomalies except that of day 253 have exhibited similar transient response characteristics. (The transient response of the anomaly of day 253 was influenced by the OST input power profile used in conducting in-orbit tests, as is detailed in a later section of this paper, Study of a TEP Anomaly in Progress.) The transient response of the OST body temperature during the anomaly of day 75, shown in figure 23, is used to illustrate similarities: The thermal anomalies began with a sudden and rapid initial rise in OST body temperature (point A, fig. 23), followed by an exponential increase (curve portion A-B) that asymptotically approached a period of linear temperature increase (curve portion B-C). At point C, the body temperature responded to reduced input power by a period of linear temperature reduction (curve portion C-D), which was followed by an exponential reduction to a stable operating temperature.

Reasons for Concern

All anomalies have exhibited the same unstable temperatures near the OST rf output port. The region of thermal instability has produced initial rates of temperature rise of 0.41 to 1.52 degrees C per minute. The rates have not, for the temperatures encountered, shown any evidence of asymptotic limiting or an upper temperature bound. The results of elevated operating temperatures have been investigated to determine reversible and irreversible effects that could lead to failure or permanent degradation of the TEP and/or the supporting system. The effects of elevated operating temperatures are presented with respect to the OST body and in order of increasing limiting temperatures.

Input rf signals to the OST are provided by means of semirigid coaxial lines that use an internal Teflon dielectric. The dielectric has been cured to temperatures of 100° C because higher temperatures produce dielectric shrinkage, which results in input signal mismatches. The degree of mismatch is a function of the time-temperature product. This temperature will lag the OST body temperature and will be reached when the body temperature exceeds about 105° C.

Nonmetallic materials used in the fabrication of the OST are listed in table II. These materials have been tested at 125° C and 1.33×10^{-4} pascal (10^{-6} torr) for

24 hours. They are expected to change little, if at all, during operations at or below 125°C .

The OST is focused by means of samarium-cobalt magnets. An investigation of temperature effects on OST focusing, presented in appendix B, led to the following conclusions:

(1) Operation for several hours at or below 150°C will have no noticeable irreversible effect on the magnets used for focusing.

(2) Reversible changes that produce increases in beam interception on the body have sensitivities peculiar to each tube. However, body current at saturation probably will not exceed 10 milliamperes for body temperatures below 100°C .

Indium was used between thermal conducting interfaces, as shown in figures 2 and 3. Body temperatures of 156°C (melting point of indium) would result in permanent loss of interface pressure and failure of the thermal conducting path.

STUDIES AND FINDINGS

The studies pursued in this investigation took several separate, but closely related, courses. Ambient and vacuum ground tests were performed on flight-type TEP components in an attempt to produce, in a controlled laboratory setting, temperature signatures like those observed on the TEP during the anomalies. This was done by simulating a number of reasonable forms of equipment failure. To complement these hardware tests, a computer study of the modeled TEP was made in an attempt to analytically identify the most probable cause of the anomalies. All pertinent in-orbit telemetry data from the TEP for a time period well preceding the first anomaly to well after the fourth one was reviewed to fully characterize the temperature excursions as well as the pre- and postanomaly conditions. Only limited data were available from prior in-orbit operation because use of the TEP during earlier eclipse seasons had been suspended because a spacecraft supporting power subsystem had failed. A review of these data revealed that there had been no earlier anomalous performance and that the anomalies had occurred only during the seasons when the spacecraft was eclipsed by the Earth. In-orbit TEP operation exercises were performed that included attempts to intentionally precipitate thermal anomalies and to manipulate an actual anomaly in progress. The commercial developer of the VCHPS was engaged as a technical consultant to investigate possible VCHPS malfunctions and to assess the possible relation of the malfunctions to the observed anomalies. In addition, a rigorous analysis of the OST body temperature transients observed during the unstable periods was performed to help identify the cause of the anomalies.

These studies and the findings derived from them are detailed in the following sections of this paper.

Room-Ambient OST Tests

Output stage tube 2030, which is essentially identical in configuration to the OST on CTS, was selected for a series of room-ambient tests. This OST is shown in figure 24, and structural details are identified in figures 1 and 2. The tube was thermally instrumented as shown in figure 25 and was mounted on a water-cooled baseplate calorimeter. The multistage-depressed-collector portion of the OST was cooled by means of a fan. The thermocouple assemblies used were copper-constantan (ANSI symbol T) fabricated with 24-gage (0.051-cm (0.0201-in.) diam) Teflon-insulated wires. The thermocouples were electrically grounded to the OST and were attached by means of an epoxy cement (Eccobond 285/Catalyst 11, products of Emerson and Cuming, Inc., Canton, Mass.). The reference junction temperature was oven controlled at 66⁰ C. After appropriate electrical, instrumentation, and radiofrequency connections were made, the body portion of the OST was completely surrounded with insulating material to minimize convection heat losses. The insulating material was expanded polystyrene spheres averaging 0.32-centimeter (0.125-in.) diameter, and the minimum thickness of coverage was 5.1 centimeters (2 in.). Finally, a suitable power supply, OST driver (rf input to OST), and rf output power-cooled load were appropriately connected. Temperature and electrical data (48 channels) were recorded on command by means of an analog scanner (scanning time, ~10 sec) that produced digital readouts in engineering units on paper tape.

As already stated, this test series was conducted in an attempt to reproduce for study the TEP temperature characteristics observed during the anomalies. Early speculation as to the cause of the anomalies included the possibility of thermal interface separations within the OST itself. As a consequence, in addition to a baseline data test with the normal OST configuration, a number of separate tests were made, each with a different major OST thermal interface compromised. The interfaces intentionally compromised were those between the longitudinal, copper OST thermal bus bars and the aluminum mounting saddles at the rf input and output ports (fig. 3) and those between the OST baseplate and the baseplate calorimeter. (Of course, in this configuration the baseplate calorimeter fulfilled the function of the VCHPS mounting saddle in the CTS spacecraft.) The interfaces were compromised by loosening the connecting screws to relieve clamping pressure. For good failure simulation, the joints were gently tapped to encourage separation. In each test, the TEP was operated at saturated rf output power at centerband frequency.

Because of the masking effects of convective and conductive heat transfer in the room-ambient interface separation tests, a close approximation of the OST temperature characteristics during an in-orbit anomaly was neither anticipated nor realized. As expected, each test resulted in measured OST body temperatures higher than those identi-

fied as normal in the baseline test. The temperature characteristics that most closely resembled the anomaly data were those from the test in which the OST baseplate was separated from the baseplate calorimeter. Only in that test did the OST body temperature continue to rise very rapidly until the rf output power was reduced by the operator, as was the case in the in-orbit anomalies.

Computer Studies

A multinode (603 nodes) digital computer program that thermally modeled the CTS TEP was operated in a number of failure-simulating modes in an attempt to identify analytically the thermal interface failure most likely to have produced the OST body temperature anomaly signature observed in orbit.

A number of cases were run in which thermal interface separations were simulated by the technique of greatly decreasing the thermal contact conductance at these interfaces. Interfaces examined in this fashion included the connections between the OST body and the mounting saddles (figs. 1 and 2) at the input and output waveguide positions and also those between the mounting saddles and the OST baseplate. Heat-pipe failures were simulated by reducing the program conductance to the heat-pipe vector to zero, resulting in a heat-pipe "dryout." Computer cases were run that simulated failures of heat pipes 2 and 3 and also of all three pipes (fig. 5).

The validity of all the computer simulations depends on many factors, including the modeling method, the masses and thermal properties of the materials involved, and the thermal conductance values used at the thermal interfaces. As with the room-ambient OST test results, computer simulation did not closely approximate the OST temperature characteristics during an in-orbit thermal anomaly. Although in each simulation there was a rise in OST body temperature, only the cases with simulated heat-pipe failures produced a temperature signature like that observed during an in-orbit anomaly.

Thermal-Vacuum OST Tests

In an effort to more accurately study the effects of OST thermal interface failures on the temperatures measured on the tube and to assess their possible relation to the observed anomalies, OST 2030 instrumented as for the room-ambient OST tests was subjected to a number of thermal-vacuum tests. The test facility used for this testing program is located at the Lewis Research Center and is shown schematically in figure 26.

The vacuum chamber of the CTS OST thermal-vacuum test facility (TVTF) (ref. 6) is a horizontal, cylindrical vessel approximately 1.8 meters (6 ft) long by 1.2 meters

(4 ft) in diameter. The vessel walls are equipped with appropriate vacuum system feed-through fittings for required instrumentation and with rf, electrical, and cooling line connections. The chamber is equipped with sorption and vac-ion pumps for fore and primary pumping functions, respectively. The pumping capability of the facility is such that a pressure less than 1.33×10^{-3} pascal (10^{-5} torr) was maintained during all the OST testing described here. Attached electric heaters permit vacuum bakeout of the vessel to 200°C with the OST removed. In addition to the equipment for measuring thermal characteristics (to be described), accessory facility equipment included an rf driver and appropriate OST power supplies. As in the room-ambient OST tests, temperature and electrical data (48 channels) were recorded on demand by means of an analog scanner (scanning time, ~ 10 sec) that produced digital readouts in engineering units on paper tape.

A thermally isolated aluminum calorimeter to which the OST baseplate was attached by means of RTV 11, a silicone rubber product of General Electric Co., was mounted inside the TVTF. This calorimeter, which simulates the OST mounting platform (heat-pipe saddle) in the CTS spacecraft, was used to control the OST baseplate temperature and also to measure the heat rejected from the tube body. The calorimeter has an internal silicone-fluid flow system formed by an arrangement of interconnecting drilled holes designed to maintain relatively uniform OST baseplate temperatures. The temperature of the silicone fluid, and consequently the OST baseplate temperature, was regulated by means of a closed-loop heat-exchanger system located outside the vacuum vessel. The temperature of the OST baseplate - calorimeter interface was measured by means of two thermocouples. The OST body heat-rejection rate was determined experimentally on the basis of the coolant properties, flow rate, and temperature change through the calorimeter. The coolant flow rate and temperature change were measured by means of a turbine-type flowmeter and a thermopile device, respectively.

As is shown schematically in figure 26 and photographically in figure 27, a liquid-nitrogen-cooled copper jacket surrounded the MDC portion of the OST when the tube was in position for testing in the TVTF. The MDC rejected heat by radiation to this jacket as a simulation of radiation to space in in-orbit operation. A water-cooled, microwave rf load located outside the TVTF was used to calorimetrically measure the output power of the OST. Since the cooling water was the rf-absorbing medium, output power could be experimentally determined on the basis of thermal properties, water flow rate, and temperature change through the load. As with the baseplate calorimeter, the coolant flow rate and temperature change were measured by means of a turbine type of flowmeter and a thermopile device, respectively.

Several of the tests that were performed with the OST in the TVTF are listed in table III. Tests 1 to 16 were attempts to produce OST temperature characteristics like those during an in-orbit thermal anomaly by compromising thermal interfaces or

reducing cooling. Figure 28 shows the body temperature characteristics when the clamping force was removed from the OST baseplate - calorimeter thermal interfaces by loosening the connecting screws and gently tapping the joints to encourage separation. Although, as expected, the body temperature increased rapidly in each of the two cases shown, the initial rate of temperature rise was about 4.5 degrees C per minute - much greater than the characteristic observed during an in-orbit anomaly. Also, the body temperature during the test approached a maximum (because some thermal interface contact remained), but the temperature during an in-orbit anomaly did not display a tendency to maximize. Figure 29 shows the OTS body temperature response to loosening the interfaces between the copper OST bus bars and the aluminum mounting saddles in three ways. The initial rate of temperature increase for the range covered in these cases (~ 6.5 to 8.7 deg C/min) was again much greater than that during an in-orbit anomaly.

Because the rates of body temperature increase during these tests were much higher than those during an actual OST thermal anomaly and because it is unlikely that a thermal interface would open and close in orbit, the compromised-interface explanation was considered extremely improbable. Therefore, testing emphasis was subsequently directed toward simulating the malfunction of the OST thermal control system, specifically the VCHPS.

Temporary malfunction of the VCHPS was simulated by operating the OST at normal conditions until essentially thermal equilibrium was achieved and then suddenly reducing the coolant flow rate in the TVTF baseplate calorimeter. The normal operating conditions were a nominal saturated rf output power of 200 watts, a center-band frequency of 12.080 gigahertz, and an OST baseplate temperature of about 56° C.

Figure 30 shows the OST temperature response when cooling was reduced to zero and to 20 and 50 percent of the level required to achieve the OST baseplate equilibrium temperature of about 56° C. The closest approximation to the body temperature profiles in an in-orbit OST anomaly appears to lie between the curves for cooling reductions to 20 and 50 percent. Therefore the temperature profiles of the OST body, the waveguide coupler, and the MDC flange for cooling reductions to 20 and 50 percent are shown in figure 31. This figure also shows the approximate initial temperature change rates for these quantities - both for these tests and for the actual OST thermal anomalies of days 75, 82, and 101 (1977). The cooling reduction curves shown in figure 31 roughly approximate the in-orbit anomaly characteristics. From this, then, it can be inferred that the anomalies may be caused by a temporary reduction in VCHPS effectiveness of between about 50 and 80 percent.

CTS In-Orbit Tests

Shortly after the first observed TEP thermal anomaly on day 75 of 1977 (Mar. 16) an in-orbit test was performed in an attempt to precipitate another anomaly in a way that would identify the "triggering" conditions. During this test, on day 92 (Apr. 2, 1977), the TEP was operated at the same general time of day and over a range of conditions that was thought to typify the TEP operating profile of day 75. Starting at 18:00 GMT (1:00 p.m. EST) the TEP was operated for 20 minutes at saturated rf output power (~ 220 W) at center-band frequency (12.080 GHz) with an unmodulated carrier. Then, in successive 20-minute periods, the TEP was operated at center-band frequency with color-bar modulation and a 1-kilohertz audio tone at rf output power levels of 150, 180, 190, 195, 200, 205, 210, 215, 220 (saturation), 215, 210, 205, 200, 195, 190, 180, and 150 watts. The test was concluded at 00:20 GMT (7:20 p.m. EST) with a repeat of the first 20-minute portion of the test.

During the entire test, all the measured TEP temperatures and electrical characteristics remained at levels that, from experience with the TEP (ref. 4), were within normal ranges for the operating conditions.

This testing sequence did not identify the causes or triggering conditions for the TEP anomaly of day 75. Nevertheless, the results implied that the cause of the anomaly was probably related to earlier operating and/or environmental conditions as well as to the conditions of the time of the anomaly.

Partially because of the small Sun angle relative to the CTS orbital plane (and the VCHPS radiator panel) on day 75, the temperature of the VCHPS radiator fell to near the freezing point of methanol (-98° C) before the anomaly on that date (figs. 14(k) and (l)). The sensor locations at which those temperatures were measured are shown in figure 5. To investigate the possible relation between these low radiator temperatures and the TEP thermal anomaly, a second CTS in-orbit test sequence was performed on day 114 of 1977 (Apr. 24).

This test sequence was started at 12:38 GMT (8:38 a.m. EDT) when the TEP was put in "standby" mode (50-percent heater power; all high voltages off). The TEP had been operating at about 160 watts rf output power for at least 3 hours before that time. In addition, the heaters attached to the TEP were turned off at 13:00 GMT to accelerate the cooling process. From 12:38 to 16:46 GMT, when the heaters and the TEP were turned back on, the VCHPS temperatures indicated by sensors HP5T and HP6T (fig. 5) had fallen from -42.2° and -38.4° C to -102° and -94.8° C, respectively (and had been at the lower temperatures for at least 20 min). The TEP rf output level was quickly raised to saturation (~ 200 W) with color-bar carrier modulation and 1-kilohertz audio tone at center-band frequency, and all the TEP temperatures were continuously monitored until 20:00 GMT (4:00 p.m. EDT). Although temperatures HP5T and HP6T re-

mained near their low levels during this period, at about 18:46 GMT all the TEP temperatures reached and remained at equilibrium values that were within recognized normal ranges for the operating conditions. As with the first in-orbit CTS TEP test to precipitate a thermal anomaly, no direct causes or triggering conditions were identified. It was concluded, however, that if methanol freezing was related to the anomaly, it had to be in combination with other conditions in a pattern not yet identified.

A third in-orbit test was conducted on day 247 of 1977 (Sept. 4). Test conditions were selected to produce conditions favorable to the triggering of a TEP anomaly that could then be directly manipulated and studied in real time. One of the purposes of the study was to determine a level of operation (rf output power level) at which a stable, safe OST body temperature could be achieved and maintained during an anomaly. The test began at 12:00 GMT (8:00 a.m. EDT) with a 2-hour period of TEP operation at the dc beam (zero rf output power) condition. This period was preceded by about 3.5 hours of noncontinuous use of the TEP at rf output power levels ranging from 0 to about 130 watts. The dc beam operation period was followed by operation at near-saturated rf output power (~ 200 W) with unmodulated carrier at center-band frequency. This operating condition was maintained until 24:00 GMT (8:00 p.m. EDT), during which time no anomaly was observed.

Room-Ambient VCHPS Tests

Each anomaly was preceded by, or accompanied by, an abnormal temperature difference between the adiabatic sections of heat pipes 1 and 3. The normal value for this quantity, designated herein as HP31A, is from 0 to 3 degrees C when all heat pipes are active at or near the saturated rf output power operating condition for the TEP. The condition that all heat pipes are active is satisfied when $HP1T > 25^{\circ}\text{C}$ and $HP3T > HP2T > HP1T$, where the symbols are the adiabatic section temperatures of heat pipes 1, 2, and 3. The abnormal values noted for the temperature difference HP31A during the anomalies were about 4 degrees C or greater. This characteristic is described more completely in the section THERMAL ANOMALIES.

An experimental program was undertaken at Lewis to investigate what VCHPS operating conditions would give rise to these anomaly-period temperature differences. The flight backup VCHPS assembly (serial number 004), which has thermal characteristics like those of the flight assembly, was taken from storage and positioned in an appropriate test stand (fig. 32). Details of the VCHPS construction and its specifications are noted in reference 5. The OST was simulated by an oxygen-free, high-conductivity copper thermal model (fig. 33). The model was made in four separate blocks, which together approximated the heat capacity of the flight OST. The four

blocks, each of which was designed to simulate the heat load from its corresponding section of the OST, were drilled and fitted with electrically insulated heater coils, as shown. The blocks were then separately mounted on aluminum saddle support blocks in the same manner as shown in figure 3. The saddle blocks were also mounted on an OST baseplate in the same way the flight OST was assembled. The aluminum saddles and baseplate were taken from a CTS OST not selected for flight. Both the saddle blocks and the baseplate were split longitudinally to permit unsymmetrical thermal loading of the VCHPS. One test was performed before the saddles and baseplate were split.

The simulated OST was instrumented as was OST 2030 in the room-ambient OST tests. For the VCHPS tests, however, the simulated-OST thermocouples were peened in place rather than attached by epoxy cement. In addition to the thermistors and platinum resistor thermometers shown in figure 5, a number of thermocouples were also attached to the VCHPS and monitored during the tests. The VCHPS thermocouples were all made of the same material and attached in the manner described for the OST used in the room-ambient OST tests. One thermocouple was located on the top of each heat pipe (1, 2, and 3) near the OST electron gun end of the heat-pipe saddle. These thermocouples are shown in figure 33 and are designated, respectively, as HP1,sdl.; HP2,sdl.; and HP3,sdl. Thermocouples were also positioned on the side of each heat pipe's adiabatic section within 1.27 centimeters (0.5 in.) of the thermistor location plane. These instruments were designated, respectively, HP1,side; HP2,side; and HP3,side. Finally, thermocouples HP1,bot.; HP2,bot.; and HP3,bot. were attached to the bottoms of the heat pipe within 1.27 centimeters (0.5 in.) of the thermistor location plane. (The thermistors were located on the bottoms of the heat pipes.) The VCHPS adiabatic section is shown in figure 34.

Before the test, the simulated OST was wrapped in glass-wool insulation (fig. 35) and then submerged in insulation (expanded polystyrene spheres averaging 0.32-cm (0.125-in.) diam) to minimize convection heat losses. Testing consisted of applying heat to the individual blocks of the simulated OST by means of four separate, regulated dc power supplies; establishing desired VCHPS operating conditions; and monitoring temperatures. Each test was continued to thermal equilibrium or to the point where the temperatures changed by less than 1 degree C for at least 15 minutes.

The results of the room-ambient tests are tabulated in table IV. The first test was the "normal" (or baseline) test, in which a heat load approximating that of the flight OST operating at saturated rf output power (220 W) was applied to the heat-pipe saddle. Although the measured heat-pipe temperatures were not representative of in-orbit temperatures because of the differences in environment, the differences in temperature between heat pipes are considered reasonably representative. The difference in temperature between heat pipes 3 and 1 at the adiabatic section were within the normal in-orbit range, 0 to 3 degrees C.

The second test (table IV) was one in which all the heat was applied on the heat-pipe-3 side of the saddle (before the saddle and baseplate were split). This test was made to simulate the failure or separation of the thermal interface between the OST baseplate and the heat-pipe saddle. Even with this unsymmetrical heating, the temperature differences between heat pipes were within the normal in-orbit range.

A modification of the second test (test 3 in table IV) repeated the same unsymmetrical heat load on the heat-pipe saddle, but with the OST body saddles and baseplate split as shown in figure 3. During this test the heat pipes "turned on" (or became active), as indicated by abrupt temperature increases to operating levels at the adiabatic section in reverse order (3, then 2, then 1) from the other tests. The temperature differences between heat pipes were still within the normal range.

The fourth test was one in which a heat load representative of the flight OST was applied with heat pipe 1 not operating. The heat-pipe assembly was first tilted from horizontal by rotating it on the axis of the heat-pipe saddle until the inert-gas-reservoir end of the radiator was about 3.8 centimeters (1.5 in.) lower than the adiabatic section. The gas reservoirs of heat pipes 2 and 3 were then heated by means of attached tape heaters to keep these pipes temporarily inactive. Approximately 216 watts was then applied to the heat-pipe saddle and quickly resulted in arterial depriming of heat pipe 1. The saddle heat input was then reduced to 158 watts, and the heat was removed from the gas reservoirs. Heat pipes 2 and 3 responded rapidly and assumed the heat load, while the system tilt prevented the arteries of heat pipe 1 from repriming. The differences in temperature between HP3, side and HP1, side and between HP3T and HP1T measured in test 4 were 5.7 and 5.6 degrees C, respectively, strongly similar to the observed in-orbit anomalies.

Test 5 was identical to test 4, except that in test 5, heat pipes 1 and 2 were caused to fail by arterial depriming in the same manner as heat pipe 1 was caused to fail in test 4. The heat-pipe temperature differences for this test were 7.8 to 8.9 degrees C, significantly higher than those during OST thermal anomalies. Test 6 was conducted at a reduced heat load to the heat-pipe saddle and with all three heat pipes operating with arteries deprimed. The heat-pipe temperature difference for this test was 2.3 degrees C, which is within the normal in-orbit range of 0 to 3 degrees C.

Study of a TEP Anomaly in Progress

A TEP thermal anomaly began at about 14:20 GMT (10:20 a.m. EDT) on day 253 of 1977 (Sept. 10) while the TEP was in uplink control from Lewis. This anomaly, like the earlier three, was characterized by a sudden, rapid rise in OST body temperature while essentially constant operating conditions were being maintained.

TEP operation by Lewis began at 12:45 GMT when the TEP was driven to saturated rf output power (~ 200 W) at center-band frequency (12.080 GHz). This was preceded by a period of about 2 hours during which the OST was inactive in a "standby" status. At 12:45 GMT, none of the three heat pipes of the VCHPS were active; that is, their adiabatic section temperatures were all less than 25° C. The temperature at the gas-reservoir end of the heat-pipe system radiator was about -61° C. At about 13:37 GMT, at the same TEP operating conditions, all the heat pipes became active. By 14:12 GMT, the OST body temperature had stabilized at about 51° C, and there was virtually no temperature difference between the adiabatic sections of heat pipes 3 and 1 (HP3T - HP1T = HP31A).

At 14:20 GMT, the OST body temperature began to rise above the level at which it had previously stabilized, with no change in TEP operating conditions. At 14:32 GMT, the body temperature had increased to 55.5° C and HP3T - HP1T was 3.9 degrees C. During the next several hours, the anomaly characteristics as functions of OST rf output power and VCHPS temperatures were studied. Pertinent operating conditions and temperatures for this period are shown in curve form in figure 36, and an outline of the events is given in table V. The HP31A profile for the period is shown in figure 22(e). Telemetry data for the $11\frac{1}{2}$ hours before 11:37 GMT on day 253 are not available, in contrast to the other anomaly days.

To briefly summarize the study of the anomaly on day 253, the OST body temperature twice was reduced by reducing the rf output power and then increased; the anomaly condition was retrigged on both occasions. Further, the maximum heat-rejection capacity of the VCHPS during an anomaly was identified by trial. This residual heat-rejection capacity is about 106 watts, which corresponds to an rf output power level of about 140 watts at the center-band frequency.

Contractual Investigation

A contract effort for the analysis and investigation of possible failure modes of the CTS TEP heat-pipe system, contract NAS3-21012, was negotiated with the developer of the VCHPS, the Defense and Space Systems Group of TRW, Redondo Beach, California. The principal TRW investigator was Dr. Bruce D. Marcus. The results of this investigation are presented in reference 7.

All the CTS flight data, ground-test results, analytical conclusions, and other relevant information presented in this report were made available to Dr. Marcus for his study. His considerations for possible heat-pipe malfunction modes concentrated on arterial depriving but included the effects of methanol - the heat-pipe working fluid - freezing under thermal load near the condenser end of the heat pipes. Also included

were the effects of surface-tension-induced surface flow toward the condenser along continuous vapor-liquid interfaces (Marangoni flow) and gas evolution within the arteries - either or both of which could contribute to arterial depriming.

Although the contract summary report does not identify specific mechanisms for heat-pipe arterial depriming that are consistent with all the CTS TEP thermal anomaly characteristics, it notes that only condenser freezing under thermal load has been experimentally shown, in normal gravity, to result in arterial depriming. The report also suggests that the anomalous OST body temperature "runaway" characteristic must be the result of the depriming of all three VCHPS heat pipes, probably in the order of their designated numbers. The residual heat-transfer capacity during the anomaly period is the open-artery (wick and groove active only) capacity of the heat pipes. This limited capacity may vary with the amount of methanol available in the heat pipes. The VCHPS system will return to normal thermal heat capacity when the thermal load is reduced and enough liquid methanol becomes available to reprime the heat-pipe arteries.

Analysis of Thermal-Anomaly Transient Behavior

Under the assumption that the thermal anomalies were induced by a loss or reduction in the heat transfer through the OST-VCHPS baseplate interfaces, the transient behavior was analyzed to determine the heat flow to the baseplate interfaces. The generality of the analysis was such that the cause could be attributed to an increase in OST-VCHPS baseplate interface resistance (figs. 2 and 3) or failure of the variable-conductance heat pipes.

The thermal network was represented by a lumped-element equivalent network shown in table VI. Any complex linear network with any number of physically realizable elements and two input-output terminal sets (ports) can be represented by a network of three complex elements (ref. 8). The three complex elements were the resistance R_B and two parallel sets of resistance and a thermal mass. The OST was represented by the network equivalent of two heat sources, two masses, and three resistances, as shown in table VI.

The heat sources were divided into two components as described in appendix C. Source one (port 1) represented the heat flow to the input saddle, and source two (port 2) represented the heat flow to the output saddle. Temperature differences with respect to the cooling (heat pipe) saddle of the copper bus (fig. 3) above the aluminum saddles were used as the port 1 and port 2 temperatures. The resistances R_A , R_B , and R_C are equivalent elements that represent the combined effects of the OST, the supporting thermal-mechanical structure, and the packaging. The thermal mass of the OST was divided into two equivalent elements. The network constants were determined experi-

mentally from thermal-vacuum tests on OST 2030.

The distributed internal heat-loss components Q_1 and Q_2 were obtained from thermal tests conducted before launch on OST 2022R1 and OST 2030. The Q_1 and Q_2 values from the flight OST, 2022R1, are given in figure 37 as functions of OST rf output power at center-band frequency. The values used in the analysis are given in table VI. With OST 2030, the resistances R_A , R_B , and R_C were determined from the steady-state parts of thermal-vacuum tests 9 to 16 (table III). Best-fit values were used for the range 50 watts to saturated output power. Small corrections were made to R_A and R_C to match normal steady-state flight data for OST 2022R1. After thermal equilibrium was attained in thermal-vacuum tests 9 to 16 (table III), failure of the OST-VCHPS baseplate interface or heat-pipe system was simulated by stopping the coolant flow and purging the coolant lines to the test baseplate. The equivalent thermal capacitances C_A and C_C were determined from the thermal resistance R_B , the heat-loss components Q_1 and Q_2 , and the change in temperature with time dT/dt . This resulted in the set of lumped-element values given in table VI.

The analysis of the day 75 anomaly transient is used to illustrate the approach. The anomalies of days 82, 101, and 253 were treated in like manner. The times used in the analysis of the day 75 anomaly transient are shown in figure 23. Table VI summarizes the quantities derived from data during the transients. At $t = A$, an initial value of Q_B , the heat flow from point 2 to point 1 through R_B (sketch on table VI), is determined by means of circuit analysis, from which is obtained

$$Q_B = \frac{Q_2 R_C - Q_1 R_A}{R_A + R_B + R_C} = 6.8 \text{ W} \quad (1)$$

where Q_1 is 22 watts and Q_2 is 116 watts. The value of Q_C , the heat flow through R_C , at $t = A+$ is

$$Q_C = Q_2 - Q_B - \left(\frac{\Delta T}{\Delta t} \right)_{A+} C_C = 19.5 \text{ W} \quad (2)$$

where Q_2 is 116 watts and $(\Delta T/\Delta t)_{A+}$ is 1.36 degrees C per minute, and

$$Q_A = \frac{-Q_B R_B + Q_C R_C}{R_A} = -23.9 \text{ W} \quad (3)$$

The heat flow through the baseplate at $t = A+$ is

$$Q_{TOT} = Q_A + Q_C = -4.3 \text{ W}$$

Continuing with the time period $t = BC$ in figure 23, the heat flow through the baseplate is determined as follows: The slope of body temperature during this period is very nearly constant, and therefore its average value is used. During a period of constant slope, if R_A and R_C are not changing with time, $\Delta T_1/\Delta t$ and $\Delta T_2/\Delta t$ will asymptotically approach equal values, such that $(T_1 - T_2)$ is constant. During the period $t = BC$

$$\begin{bmatrix} 1 & -1 & 0 \\ 0 & 1 & 1 \\ R_A & R_B & -R_C \end{bmatrix} \begin{bmatrix} Q_A \\ Q_B \\ Q_C \end{bmatrix} = \begin{bmatrix} Q_1 - mC_A \\ Q_2 - mC_C \\ 0 \end{bmatrix} \quad (4)$$

where

$$Q_A = \frac{-1}{\Delta} [(Q_1 - mC_A)(R_B + R_C) + (Q_2 - mC_C)R_C] = 17.8 \text{ W} \quad (5)$$

$$Q_C = \frac{-1}{\Delta} [(Q_1 - mC_A)R_A + (Q_2 - mC_C)(R_A + R_B)] = 91 \text{ W} \quad (6)$$

based on values of

$$\Delta = -(R_A + R_B + R_C)$$

$$Q_1 = 22.5 \text{ W}$$

$$Q_2 = 119 \text{ W}$$

$$m = 0.32 \text{ deg C/min}$$

The heat flow through the baseplate during the period $t = BC$ is

$$Q_{TOT} = Q_A + Q_C = 108.8 \text{ W}$$

During the same period Q_B is

$$Q_B = Q_2 - Q_C - mC_C = 6.94 \text{ W} \quad (7)$$

With this value of Q_B as an initial condition, the heat flow through the baseplate at

$t = C+$ can be determined. With $m = -1.51$ degrees C per minute, Q_2 is 8 watts and, from equation (7), Q_C is determined to be 100.5 watts and

$$Q_A = \frac{(Q_C)(R_C) - (Q_B)(R_B)}{R_A} = 23.2 \text{ W} \quad (8)$$

The heat flow through the baseplate at $t = C+$ is the sum of Q_A and Q_C , or 123.8 watts. By using equations (5) and (6) for the period of constant slope between points C and D, the heat flow through the baseplate can be determined. With $Q_1 = 12$ watts, $Q_2 = 8$ watts, and $m = -1.03$ degrees C per minute, the heat flow through the baseplate was found to be 125.1 watts.

This same analytical procedure applied to the transients of days 82, 101, and 253 yielded the results shown in table VI. The operations of days 82 and 253 preclude determinations as complete as those obtained for days 75 and 101. A steady-state determination of the maximum heat flow through the baseplate that produces stable body temperatures is given for comparison. The major uncertainties in this analysis are the uncertainty of the total body losses at saturation - within ± 10 watts (appendix C) - and the quantizing and noise errors of the multiplexed telemetry measurements. Thermal configuration OST 2030 is closely representative of the flight OST, 2022R1.

The heat flow through the OST-VCHPS baseplate during the anomaly transients can be reconstructed during the periods of unstable temperature as follows:

(1) Day 75: The heat flow through the baseplate fell to nearly zero (at $t = A+$). (The negative value of initial heat flow was due to measurement inaccuracies and limitations of the analysis and was interpreted as zero.) The heat flow exponentially recovered to 109 watts and remained between 109 and 125 watts from $t = B$ to $t = D$. During this time it exhibited a saturation characteristic where heat flow through the baseplate was independent of body temperature. For $t > D$, the heat flow through the baseplate became less than 125 watts and decreased exponentially as body temperature fell.

(2) Day 82: The heat flow fell to 75 watts (at $t = A+$) and exponentially recovered to 111 watts. It remained between 111 and 109 watts from $t = B$ to $t = C+$, during which time it exhibited a saturation characteristic where heat flow through the baseplate was independent of body temperature.

(3) Day 101: The heat flow fell to zero (at $t = A+$) and exponentially recovered to 100 watts. It remained between 100 and 123 watts from $t = B$ to $t = D$, during which time it again exhibited a saturation characteristic where heat flow through the baseplate was independent of body temperature. For $t > D$, the heat flow through the baseplate became less than 123 watts and decreased exponentially as body temperature fell.

(4) Day 253: The heat flow fell to 103 watts. During subsequent tests, the maximum

steady-state heat flow rate Q_{critical} that did not produce unstable OST body temperatures was determined as 106 watts.

It was concluded that the transient behavior during the thermal anomalies was produced by a function where heat flow through the baseplate for $Q > Q_{\text{critical}}$ is a weak function of, or independent of, OST body temperature. The value of Q_{critical} appears to be reproducible within the limits of this analysis. The best determination of Q_{critical} is believed to be 106 watts, the value determined experimentally during the steady-state tests of day 253. (Although Q_{critical} was attained when the OST rf output power was about 140 W at center-band frequency (12.080 GHz), this critical heat-rejection rate may be attained at different rf output power levels at other frequencies. As indicated in fig. 37, at the upper-band-edge (12.123 GHz) and lower-band-edge (12.038 GHz) frequencies, Q_{critical} will be attained at rf output powers of 127 and 157 W, respectively. These OST body heat-rejection rates as a function of frequency were determined experimentally in thermal-vacuum tests with OST's 2022R1 and 2030.)

Assessment of Anomaly Causes

The following abnormal conditions were hypothesized and examined as possible causes of the observed anomalous performance of the TEP:

- (1) Measurement failure
- (2) Sun illumination of the temperature sensors
- (3) Change in OST electrical input power, with constant rf output power
- (4) Change in rf output power, with constant OST electrical input power
- (5) Increases in thermal resistance of the interface between the OST body and the VCHPS mounting saddle
- (6) Depriming of the variable-conductance heat pipes

It is unlikely that a failure of the thermal measurements in the TEP could account for the observed thermal behavior because the only element common to the temperature sensors near the OST rf output port is the supply voltage for the sensors. If this were to fail, its effect would also be observable in the readings of eight other temperatures. This effect was not observed. It is improbable that the three anomalous temperature readings are the result of independent failures of the three temperature sensors located near the OST rf output port. Sun illumination of these temperature sensors was readily eliminated as a possible anomaly cause because of the orientation of the spacecraft at the time of the occurrences (fig. 20) and the location and orientation of the OST within the spacecraft (figs. 5 and 9). The sensors are internal to the spacecraft body, which is enclosed in a multilayer thermal blanket. The sensors were shielded from direct Sun illumination by the OST body at the anomaly times (fig. 2).

Changes in OST electrical input power or changes in rf output power that could produce increased internal losses are also unlikely because multiple independent failures would be necessary to produce the observed performance. Ground-test data and analysis have shown that a change in input power of 100 watts would be required to produce the rate of temperature change observed. Figures 14(d), 16(d), and 18(d) indicate that OST dc electrical input power was constant from well before each anomaly through the period of unstable temperatures for days 75, 82, and 101, respectively. This constancy was further substantiated by constant current indicated on the spacecraft 76-volt bus for each of these periods (data not shown). Figures 14(e), 16(e), and 18(e) indicate that the OST rf output power for the anomaly periods was also constant. In addition, there were no recorded reductions in ground-received signal strength that could be associated with a loss of rf output power. OST body current data (figs. 14(f), 16(f), and 18(f)) for these periods indicate that internal OST losses from electron beam interception were constant. Hence, it was concluded that it is improbable that the observed anomalous temperature excursions were caused by changes in OST input or output power.

Possible causes of the TEP thermal anomalies were examined comprehensively. The logic diagrams used present a systematic evaluation of all reasonable potential contributing factors or combinations and sequences of factors. These diagrams are presented in figure 38. Each diagram is addressed to a separate, distinguishable aspect of the overall thermal anomaly, which precedes and includes the unstable OST body temperature period. These aspects include the three recognizable sequential changes (figs. 38(a) to (c)) in the quantity HP31A as described earlier in item 4 of the section Similarities and Comparisons. Other aspects diagrammed were the OST body temperature increase (fig. 38(d)), the waveguide coupler temperature increase (fig. 38(e)), and the MDC flange temperature increase (fig. 38(f)). In the diagrams, each potential contributing factor is assessed by means of all the information available - including flight data, ground-test results, and analysis.

Evaluations performed with the use of these diagrams clearly indicated a temporary functional failure of the variable-conductance heat pipes by the mechanism of arterial depriming. To carry this concept further, the logic diagram presented in figure 38(g) was constructed to help identify and assess the most probable factors contributing to the heat-pipe depriming phenomenon.

At this point, it was not possible to positively identify a cause or causes of the depriming of the heat-pipe arteries that would be consistent with all the observations made in the section Similarities and Comparisons. To further complicate the assessment, depriming may be caused, not by a single factor, but by combinations or sequences of contributing factors. It is clear, however, that mechanical imperfections of the heat pipes may be dismissed as contributing factors because of their satisfactory performance after the anomalies. Therefore, manufacturing defects, structural damage, and also

heat-pipe fluid leakage are indicated as "not credible" causal factors in figure 38(g).

It has been demonstrated (ref. 7) that freezing the condenser section of the CTS heat pipes can cause arterial depriming in normal gravity. This cannot be identified as a principal causative factor, however, since on day 253 the anomaly began before the reservoir temperature approached the methanol freezing point. Further, if heat-pipe freezing were the anomaly cause, heat pipe 3 should freeze and experience depriming first, since it carries the smallest heat load of all the pipes and has a larger effective radiator surface than heat pipe 1. And, in fact, heat pipe 1 deprived first. Further, reservoir temperatures have dropped below freezing (figs. 11(k) and (l)) without anomalies occurring. Consequently, fluid freezing has been assessed as a "not credible" causal factor in figure 38(g).

A surface fluid flow caused by a temperature-gradient-induced surface-tension gradient is termed Marangoni flow. The VCHPS temperature distribution resulting from the partial shadowing of the radiator by the spacecraft during the 90° to 180° spacecraft orbital quadrant (figs. 12 and 20) was favorable to induce methanol flow on the open surfaces (fillets and excess-fluid reservoirs) toward the reservoir ends of the heat pipes. The resultant accumulation of frozen methanol at the ends of the heat pipes could reduce the working-fluid inventory. Since heat-pipe freezing was not consistent with all the anomaly occurrences, however, this effect was not considered credible as the sole causal factor. In the absence of freezing, Marangoni flow would reduce the contribution that the fluid fillets and excess-fluid reservoirs make to the heat-pipe capacity (ref. 7). This effect must be judged to be not credible (fig. 38(g)) as a sole anomaly cause, since TEP thermal anomalies would then be experienced on consecutive days with similar conditions.

Gas evolution within the arteries may be an important contributing factor to the depriming of the heat-pipe arteries, as indicated in reference 7. The solubility in methanol of the noncondensable control gas in the pipes (90-percent nitrogen - 10-percent helium) decreases with pressure and temperature. Therefore, the heat-pipe cooldown during the eclipse periods is favorable to gas saturation of the methanol in the pipes and the nucleation of gas bubbles within the arteries. This effect will be most pronounced in the segments of the arteries that have been inactive longest, specifically the reservoir ends of the heat pipes, and will result in the greatest accumulation of bubbles in those segments. When the thermal load is increased as TEP operation resumes, the advancing gas-vapor front may encompass the bubbles in the arteries of the now-active segments of the heat pipes. If the bubbles do not dissolve or vent quickly enough to prevent depriming, heat pipe 1, which becomes active first, might be expected to deprime first. This occurrence would cause the gas-vapor fronts of heat pipes 2 and 3 to advance into previously inactive segments of those pipes, thereby making them susceptible to arterial depriming because of the bubbles in those segments. It would appear

from this that the occurrence of arterial depriming and resulting TEP thermal anomalies would depend on the length of the TEP inactive period before an eclipse (affecting heat-pipe cooldown) and the operating conditions imposed at TEP start-up. Spacecraft shadowing of the VCHPS radiator in the 90° to 180° orbital quadrant (figs. 12 and 20) would also appear to favor arterial gas-bubble formation at or near the usual TEP turn-on time. This suggests that anomaly occurrences are related to daily TEP operating profiles and are therefore random during the eclipse periods, which is consistent with the anomaly occurrences. On this basis, the bubble formation explanation for arterial depriming seems the most likely. Without further study, however, the effect must be considered as unknown, as shown in figure 38(g).

SUMMARY AND CONCLUSIONS

The Communications Technology Satellite (CTS), which was developed in a joint U.S.-Canadian program by NASA and the Canadian Department of Communications (DOC), was launched into an equatorial, geosynchronous orbit in January 1976 and is stationed at 116° W longitude. The United States provided a 200-watt, 12-gigahertz, 50-percent-efficient transmitter experiment package (TEP) for CTS. The TEP consists of an output stage tube (OST), a power-processing system (PPS), and a variable-conductance heat-pipe system (VCHPS).

On four occasions in 1977 - March 16, March 23, April 11, and September 10 - several measured OST temperatures displayed sudden, rapid increases not normal for the TEP operating conditions and inconsistent with the design of the thermal control system. Between these anomalies and after the fourth, the TEP thermal control system has apparently functioned essentially as designed.

A review of the characteristics of the TEP thermal anomalies, a brief description of some parts of the investigation pursued, and a summary of the conclusions reached and recommendations offered are presented in this section. The investigation included the use of flight-type TEP components in ambient and thermal-vacuum ground tests, analytical studies, intensive flight data review, and CTS in-orbit tests. The purpose of the investigation was to determine the most probable cause of the anomalies and to identify procedures or TEP operating modes that will preclude damage to the OST from the occurrence or continuation of the anomalies and that will minimize their negative impact on CTS users.

The following features of the observed TEP thermal anomalies were noted:

1. All the anomalies were characterized by sudden, unanticipated, and rapid increases in OST body temperature and two other temperatures near the OST radiofrequency (rf) output port while the TEP was operating at essentially constant normal con-

ditions. These increases resulted in abnormally high temperatures for the operating conditions.

2. All the anomalies occurred after relatively long periods of constant, normal OST rf power levels.

3. The anomalies occurred at different OST rf output power levels (160 and 220 W). Because of this, the anomalies occurred at different OST body temperatures (48° and 57° C) and rates of heat rejection from the OST baseplate (120 and 155 W).

4. All the anomalies occurred near the spring and fall equinoxes. During these periods, the Sun angle with respect to the Earth's equator (and the VCHPS) is relatively small. For the anomaly days, the Sun angle ranged from -2° to 8° .

5. All the anomalies occurred during the quadrant of the spacecraft orbit in which CTS approaches the point where it is directly between the Earth and Sun. During this orbital quadrant, the inboard VCHPS surface becomes increasingly shadowed by the spacecraft itself.

6. All the anomalies, except that for day 253, were preceded by temperatures at the extremity of one of the three VCHPS heat pipes (the only one instrumented) that were at or below the freezing point, -98° C, of the methanol working fluid.

7. All the anomalies were preceded or accompanied by a sudden abnormal increase in the difference in measured temperatures between the adiabatic sections of two of the VCHPS heat pipes. Specifically, this temperature difference, HP31A, for heat pipes 3 (longest) and 1 (shortest) increased from its normal level (0 to 3 deg C) to 3.9 degrees C or greater when the TEP was operating at or near the saturated rf output power level. This was followed by a second increase to about 5.2 degrees C. At the beginning of the unstable rise in OST body temperature, this temperature difference dropped to less than 4.2 degrees C.

If this abnormal temperature difference is interpreted as symptomatic of arterial depriming, HP31A measured before and during the unstable state of each thermal anomaly shows that the heat pipes deprimed in sequential order. First, HP31A became greater than 4.2 degrees C. This increased temperature difference was always accompanied by a step increase in OST body temperature as heat pipe 1 deprimed. The adiabatic section of heat pipe 1 then cooled slightly, and heat pipes 2 and 3 warmed slightly as they assumed the additional heat load previously conducted by heat pipe 1. (This warming could not be due to either heat pipe 2 or 3 depriming, for that would result in no change or a decrease in HP31A, respectively.) Next, the temperature difference increased an additional 1.5 to 2 degrees C as heat pipe 2 deprimed. The temperature of the adiabatic section of heat pipe 1 did not change, but the temperature of heat pipe 3 increased as it conducted the additional heat load previously conducted by heat pipe 2. (This warming could not be due to heat pipe 3 depriming for that would reduce its adiabatic section temperature and thereby reduce HP31A.) Heat pipe 3 then deprimed and

HP3TA decreased, resulting in a reduction of HP31A. At this point the unstable rise in OST body temperature began. Thus, the heat pipes deprimed in designated numerical order.

8. All the anomalies were terminated without apparent TEP damage by reducing the OST rf output power.

9. The TEP recovered completely after each anomaly and showed no indications of degradation or changes in performance.

Test and analysis findings were as follows:

1. Thermal-vacuum tests with an OST essentially identical to the one on the CTS suggest that anomalies are probably not caused by thermal-interface failures. In addition to the improbability of a separated interface reestablishing integrity to recover from an anomaly, the resulting rates of OST body temperature increase would be significantly higher than those observed during the anomalies.

2. The thermal-vacuum tests that most closely approximated the anomaly temperature profiles were those in which the baseplate cooling was abruptly reduced from that required for thermal equilibrium at normal temperatures. This suggests that the anomalies are caused by abrupt temporary reductions in VCHPS effectiveness.

3. Room-ambient tests with a flight-type VCHPS suggest that the abnormally high temperature differences between the adiabatic sections of heat pipes 3 and 1 observed before or during the anomalies are caused by arterial depriming of heat pipe 1 or heat pipes 1 and 2. None of the other reasonable causes examined, including separation of the interface between the OST baseplate and the heat-pipe saddle and asymmetric heating of the heat-pipe saddle, yielded similar results.

4. Room-ambient tests with the flight-type VCHPS show that the temperature difference between the adiabatic sections of heat pipes 3 and 1 (HP31A) depends on the priming states of the heat-pipe arteries. Specifically, with all arteries primed, the difference was 1.1 degrees C; with heat-pipe-1 arteries deprimed the difference was 5.1 degrees C; with heat-pipe-1 and -2 arteries deprimed the difference was 7.8 degrees C; and with all arteries deprimed, the difference was 2.3 degrees C.

5. The temperature differences between the adiabatic sections of heat pipes 3 and 1 observed before the thermal anomalies suggest the following behavior: The first increase of HP31A to 3.9 degrees C was due to heat pipe 1 depriming. This increase resulted from a temperature increase in heat pipe 3 as it assumed that part of the heat load previously carried by heat pipe 1. The second increase of HP31A to 5.2 degrees C was due to heat pipe 2 depriming after heat pipe 1. This caused the adiabatic section temperature of heat pipe 3 to increase as it assumed the thermal load previously conducted by heat pipe 2. Finally, the reduction of HP31A when the unstable OST body temperature state began was due to heat pipe 3 depriming, which resulted in a reduction of the heat-pipe-3 adiabatic section temperature. Thus, the unstable OST body temper-

ature state of the anomalies was preceded by heat pipes 1, 2, and 3 depriming, in that order.

6. The TEP thermal anomaly of September 10, 1977 (day 253) was controlled by the Lewis staff and was used to investigate the thermal characteristics directly. During the unstable OST body temperature state of this anomaly, the body temperature was a stable function of rf output power only to about 140 watts. When the OST rf output power was increased beyond this critical level, the body temperature exhibited an unstable increase. This indicated a maximum VCHPS heat-rejection capacity of approximately 106 watts (140 W rf output power at center-band frequency), beyond which the body temperature became unstable. This characteristic of flow-limited heat rejection would be a consequence of the VCHPS arteries depriming.

7. A rigorous analysis of the OST body temperature transients shows that the VCHPS heat-rejection capacity dropped to a low of 0 to 75 watts and recovered exponentially to a near constant level (100 to 127 W), which is a weak function, or possibly independent, of TEP operating temperatures. The agreement of this analysis with the test results of (anomaly) day 253 is excellent. This again is characteristic of limited fluid flow within the heat pipes caused by arterial depriming.

Although no consistent explanation for heat-pipe depriming and subsequent recovery has been identified, the bulk of the available evidence suggests that this phenomenon is the cause of the TEP thermal anomalies and the subsequent return to normal VCHPS operation. In addition, the evidence reveals that depriming is associated with the low VCHPS radiator temperatures experienced during the spacecraft vernal and autumnal eclipse seasons (days 55 to 102 and 241 to 288, respectively) and while the spacecraft is in the 90° to 180° orbital position. These conditions, in combination, give rise to the lowest VCHPS solar heat input levels of the year.

The physical mechanisms causing VCHPS depriming are unknown. However, it is believed, based on observation, that the phenomenon is associated with low temperatures of the VCHPS radiator near the gas reservoirs. All the TEP thermal anomalies have occurred during low-temperature extremes at the gas-reservoir end of the heat pipes. The extent to which spacecraft cooling during the eclipse by the Earth contributes to the necessary set of conditions is unknown. The Earth eclipses have ranged from 25 minutes on day 101 to 73 minutes on day 82. For all the anomalies the heat pipes have deprimed in sequential order, with the one closest to the spacecraft (heat pipe 1) depriming first and the one farthest from the spacecraft (heat pipe 3) depriming last. It is highly unlikely that the causes of depriming in each heat pipe are independent yet reproducible sequentially. It is far more probable that all the heat pipes have the same limitations in an environment that is encountered sequentially by heat pipes 1, 2, and 3. Low-temperature extremes are produced sequentially from heat pipe 1 to heat pipe 3 by the shadow of the Earth-viewing edge of the spacecraft moving across the gas reservoir

in sequence. This shadowing by the edge of the spacecraft body occurs for all Earth-Sun angles, with respect to the radiator plane, greater than -3° . Anomalies have occurred for Sun angles between -2° and 8.1° . The OST body temperatures for all the anomalies, corresponding to depriming of heat pipe 3, have entered the unstable state in the orbital quadrant in which the radiator is shadowed by the spacecraft and after the gas-reservoir end of heat pipe 2 had been shadowed. Hence, it is concluded that a necessary condition for heat-pipe depriming is low temperature extremes, which are caused by shadowing of the gas-reservoir end of the VCHPS radiator.

A number of potential contributing factors to the depriming of the heat-pipe arteries were considered. These factors included freezing of the heat-pipe condensing sections, fluid migration caused by temperature-gradient-induced surface-tension effects (Marangoni flow), and gas evolution caused by rapid chilling. No single or sequential series of mechanisms for arterial depriming is consistent with all the TEP thermal anomaly characteristics. Even though the bulk of the data is consistent with arterial depriming, the factors that cause the arteries to deprime have yet to be identified.

The following recommendations are made to provide a partial basis for establishing procedures and operating modes for the TEP:

1. Procedures and operating modes should, within existing spacecraft and ground-system operating constraints, be established to protect the TEP.
2. Procedures and operating modes should be established for the time periods and OST rf output power levels for which unstable OST body temperatures are most likely to occur. The anomalous unstable temperature state is most likely to occur on those days when the Sun angle with respect to the VCHPS radiator plane is between -3° and 9° . Consideration of spacecraft yaw attitude errors results in a span of Sun angles of -4° to 10° with respect to the orbital plane. This Sun angle span occurs daily from 14:00 to 19:30 GMT. The anomalous unstable OST body temperature state will occur only for rf output power levels greater than 127, 140, and 157 watts at upper-band-edge, center-band, and lower-band-edge frequencies, respectively.
3. One of the following sets of conditions should be used in determining if the unstable OST body temperature state is imminent or in progress:
 - a. $HP1T > 25^{\circ} \text{ C}$, $HP3TA > HP2T > HP1T$, and $HP3TA - HP1T \geq 4.1$ degrees C (noting that $HP3TA - HP1T = HP31A$) and these conditions have existed for more than 10 minutes. The temperatures $HP1T$, $HP2T$, and $HP3TA$ are measured at the adiabatic sections of heat pipes 1, 2, and 3, respectively.
 - b. The OST body temperature is greater than 75° C for more than 10 minutes.
 - c. In the absence of reliable telemetry, the integrated average rf output power is greater than that which generates more than 106 watts of heat to be rejected through the VCHPS. The corresponding rf output power for this limiting condition is 127 watts at the upper-band-edge frequency condition (12.123 GHz), 140 watts at the center-band

frequency condition (12.080 GHz), or 157 watts at the lower-band-edge frequency condition (12.038 GHz).

4. In the absence of reliable telemetry, cumulative operating time should be limited to 127 minutes when the heat rejection rate through the VCHPS is greater than 106 watts. The cumulative operating time should be measured from "first turnon," where first turnon is defined as first TEP operation after the OST has attained thermal equilibrium at the standby (collector voltages off) condition. This period is the minimum time required for the OST body temperature, in the region of the output, to rise to 105° C when the TEP is operated at the saturated-rf-output-power, center-band-frequency condition.

Lewis Research Center,
National Aeronautics and Space Administration,
Cleveland, Ohio, September 26, 1978,
610-22.

APPENDIX A

MAJOR-ACTIVITIES CHRONOLOGY OF CTS TEP THERMAL ANOMALY INVESTIGATING COMMITTEE

Date	Activity
Wed., Apr. 20, 1977	Committee formed to investigate TEP anomaly
Sun., Apr. 24	CTS in-orbit test to attempt to precipitate TEP anomaly by freezing VCHPS
Wed., Apr. 27	U.S.-Canadian teleconference (via CTS) to discuss TEP anomaly investigation. Participants: R. Alexovich, A. Curren, E. Edelman, and L. Gedeon (NASA Lewis); J. Matsushita, T. Payne, Y. Wehrle, and D. Caswell (Canada, CRC).
Tues., May 3	Ambient tests with OST 2030 begun at Lewis
Fri., May 6	OST 2030 ambient tests completed
Mon., May 9	Meeting held to review TEP anomaly analytical and experimental work to date. Participants: H. Mark, R. Alexovich, A. Curren, G. Smolak, J. Hemminger, and D. Connolly Preparations begun for OST 2030 thermal-vacuum testing
Thurs., May 19	Thermal-vacuum tests with OST 2030 begun at Lewis
Thurs., May 26	B. Marcus (TRW) at Lewis for briefing on proposed anomaly-related VCHPS investigation support contract
Fri., June 10	A. Curren met with D. Petrash (NASA Lewis) to examine behavior of indium-foil thermal interface seals on OST in vacuum
Wed., June 15	Previously unnoticed TEP anomaly on March 23 discovered during flight data review
Thurs., June 16	Preparations begun for ambient VCHPS tests
Fri., June 17	Thermal-vacuum tests with OST 2030 completed VCHPS support contract approved
Mon., July 11	Ambient VCHPS tests begun at Lewis
Mon., Aug. 15	U.S.-Canadian teleconference (via CTS) to discuss TEP anomaly investigation progress and plans. Participants: R. Alexovich and A. Curren (NASA Lewis); B. Marcus (TRW), E. Stepandic (GE), J. Matsushita, T. Payne, V. Wehrle, and D. Caswell (Canada, CRC).
Tues., Aug. 16	VCHPS ambient tests completed

Date	Activity
Wed., Aug. 24, 1977	Memorandum issued requesting preemption of normal TEP operations in the event of an anomaly occurrence during autumn eclipse period (8-29-77 to 10-15-77)
Wed., Aug. 31	Memorandum issued defining special TEP operating instructions in the event of an anomaly occurrence during period 8-29-77 to 10-15-77
Sun., Sept. 4	CTS in-orbit test to attempt to precipitate TEP anomaly
Sat., Sept. 10	TEP thermal anomaly occurred, starting at 15:20 GMT; Lewis staff assumed uplink control for study
Tues., Nov. 29	Supplementary thermal-vacuum tests begun with OST 2030
Mon., Dec. 12	Supplementary thermal-vacuum tests with OST 2030 completed
Fri., Feb. 10, 1978	Memorandums issued requesting preemption of normal TEP operations and defining operating instructions in the event of an anomaly occurrence during spring eclipse period (2-26-78 to 4-14-78)

APPENDIX B

TEMPERATURE EFFECTS ON FOCUS MAGNETS

Denis J. Connolly

Temperature effects on permanent magnets fall into three categories:

(1) Metallurgical changes may be caused by exposure to too high a temperature. Such changes require extremely high temperatures and will not be of concern here.

(2) Irreversible losses are defined as partial demagnetization of the magnets that is caused by either high or low temperatures. They are recoverable by remagnetization. The degree of irreversible losses depends on the temperature to which the magnets are exposed, the exposure time, the history of the magnets, the magnetic circuit they are in, and of course the magnet material. Irreversible losses can be reduced by prestabilization (preheating and remagnetization).

(3) Reversible losses are changes in flux that are reversible with temperature. The flux loss, which is due to a temperature increase, is spontaneously regained when the magnet cools to the initial temperature. Reversible losses also refer to partial demagnetization of the magnets caused by high temperature. However, the reversible loss is spontaneously regained when the magnet cools to the original temperature.

In this appendix we first discuss reversible losses in the type of focus magnet used in the CTS OST (samarium cobalt). The reversible temperature coefficient is about -0.045 percent per degree C. We then discuss the irreversible losses in samarium-cobalt magnets. For temperatures of 150° C or less and exposure times of a few hundred hours or less, the irreversible losses are negligible ($\ll 1$ percent). Finally, we discuss the sensitivity of beam interception current to magnet temperature increase. The temperature increase necessary to trip the 10-milliampere body current relay may be as high as several hundred degrees C.

Reversible Losses in Focus Magnets of CTS OST

The focus magnets used in the CTS OST were made by Raytheon of samarium cobalt. According to Dr. Wyreck of Raytheon (private communication), the reversible temperature coefficient of their samarium-cobalt magnets from near-room temperature to a few hundred degrees C is -0.045 percent per degree C, with different batches having the same temperature coefficient within ± 5 percent.

Several other samarium-cobalt magnet manufacturers claim reversible temperature coefficients from -0.04 to -0.06 percent per degree C. A value in this range can therefore be used for the CTS OST magnets with a high degree of confidence.

Irreversible Losses in Focus Magnets of CTS OST

According to Litton drawings, the CTS OST focus magnets were temperature stabilized to 200°C . Dr. Wyreck states that, for magnets so stabilized, exposure to 150°C for 1000 hours would not result in significant irreversible losses.

Dr. Wyreck's statements were based on a study by Dayton University published in 1974 (ref. 9). The study involved the thermal aging characteristics of samarium-cobalt magnets. The samples tested were purchased from two suppliers: General Electric and Raytheon. However, the lots are not identified according to manufacturer in the report. Table VII and figure 39 were taken from reference 9. Table VII shows results for several lots prestabilized at 200°C and aged for 3046 hours at 150°C . In each case the loss is well under 1 percent. Figure 39 shows that even this modest loss occurs rather late in the test period.

This information leads to the following conclusion: For exposure times less than a few hundred hours and temperatures less than 150°C , the irreversible loss in magnetization of the CTS OST magnets will be negligible.

Effect of Reversible Loss in Magnetization on Beam

Interception Current (Body Current)

It may be useful to estimate the magnet temperature at which the body current relay (set at 10 mA) would shut down the OST because of a body current increase resulting from a reversible decrease in focusing fields. During the recent thermal anomalies, OST 2022 experienced temperature increases of about 30 degrees C with no observable increase in body current. (The resolution of the telemetry channel is 0.06 mA). However, it is not reasonable to conclude that the body current is insensitive to magnet temperature over a wide range.

The electron beam is guided through the beam tunnel by a periodic-permanent-magnet (PPM) focusing stack. If the PPM fields have a high degree of azimuthal symmetry and axial periodicity and satisfy certain criteria on shortness of the period, their effect is very much like that of a uniform solenoidal field with the same rms value of axial magnetic field strength B_z . The beam radius varies inversely with B_z . More generally, the PPM stack acts as a series of magnetic lenses. Local imperfections in the focusing fields show up as eccentricity, or defocusing, several cavities downstream from the imperfection. Each tube is hand focused by placing numerous small magnetic shunts on the focusing stack at positions where they give evidence of reducing beam interception. When this process is complete, the electron flow follows a serpentine path through the beam tunnel that is determined by the aggregate effect of the initial imper-

fections in the PPM stack, launching conditions, and the intentional imperfections introduced in the focusing operation. The focusing process is considered complete when the beam interception is acceptably low.

In the situation described, radial excursions in electron flow will still tend to be inversely proportional to B_z . However, the increase in beam interception caused by a local decrease in magnetic field strength may be many times larger than a uniform, axially symmetric analysis would indicate.

A lower bound on the sensitivity of beam focusing to magnetic field strength can be estimated as follows: Assume the electron flow initially follows a normal distribution with radius, that is,

$$J = \frac{I_0}{\pi b^2} e^{-r^2/b^2} \quad (B1)$$

where

- J beam current density
- I_0 beam current
- b characteristic radius
- r radial position

Since the radial position of the beam electrons is a characteristic of a large population subjected to many independent influences, equation (B1) may be based on statistical principles without even considering the physics of the problem. The characteristic radius b will be considered unknown. The beam current I_0 is approximately 70 milliamperes. The beam interception I_b is now given by

$$I_b = \int_0^{2\pi} \int_a^\infty J r \, dr \, d\theta = I_0 e^{-a^2/b^2} \quad (B2)$$

where

- a tunnel radius
- θ azimuthal coordinate

Equation (B2) is plotted in figure 40. The beam interception current, at saturation conditions, on well-focused CTS tubes, is about 4 milliamperes. From figure 40, the characteristic radius b is thus about 0.04 centimeter (0.015 in.). The increase in b that would be required to increase I_b to 10 milliamperes (the value required to trip the overcurrent relay) appears from figure 40 to be 20 percent. In general, the sensitivity

of I_b to changes in b is about 1 milliampere per 3-percent increase in b . If the beam and focus fields were axisymmetric, this would imply that the sensitivity of I_b to changes in field strength B was about 1 milliampere per 3-percent decrease in B .

From the previously established sensitivity of field strength to temperature rise, the sensitivity of interception current to magnet temperature (assuming axisymmetry) would be about 1 milliampere per 65 degrees C (0.015 mA/deg C). Expressing equation (B2) as a function of temperature yields

$$I_b \approx I_0 e^{-a^2/b_0^2 [1 + \alpha(T - T_0)]^2} \quad (B3)$$

where

b_0 b at reference temperature T_0

α 0.0005

T_0 a reference temperature taken as 50° C

Based on equation (B3), the temperature rise necessary to reach 10 milliamperes body current is approximately 400° C. This is too high to be realistic because the reversible temperature coefficient of samarium-cobalt magnets increases rapidly above about 250° C. The result does, however, indicate that the magnets might reach 250° or 300° C before the OST shut down automatically. Since the CTS output stage tubes all had asymmetries imposed on the focusing array in order to achieve minimum interception current, they may behave substantially differently than indicated by this result - at least for small temperature changes. This is illustrated by the limited experimental data available in which the same OST was operated in a vacuum at the same electrical conditions but different baseplate temperature. The data are listed here.

OST	Condition	Sensitivity of beam current to changes in effective beam radius, mA/deg C
2025	Thermal-vacuum test	+0.04
2030	Thermal-vacuum test	-.03
2022R1	In space during anomalies	0±0.06

The spread in the data introduces more uncertainty, so we will hedge further and state the following conclusion: The temperature at which the body current relay (on OST 2022R1) shuts off is not likely to be much below 100°C because body temperature has already increased to 75°C or 80°C with no noticeable change in body current. On the other hand, a temperature as high as several hundred degrees C may be required for automatic shutdown. This statement is broad enough that it also applies to OST 2030.

APPENDIX C

THERMAL OUTPUT OF OST 2022R1 AND OST 2030

Denis J. Connolly

Output stage tube OST 2022R1 is part of the CTS transmitter experiment package presently experiencing thermal anomalies in space. OST 2030 is being used in experimental efforts to determine the cause of these thermal anomalies. Therefore the waste heat outputs of OST 2022R1 and OST 2030 were estimated to determine whether the two OST's are appreciably different in this regard and also to estimate how the flow of waste heat is divided between the input and output saddles (fig. 2).

The waste heat generated by output stage tubes of the type used on CTS can be grouped into four categories:

(1) Cathode heater power - This loss can be accurately measured and is about 4 watts on each OST. It will be assumed to flow out entirely through the input saddle.

(2) Beam interception power - This loss cannot be measured since the energy with which the intercepted electrons impact must be estimated. The distribution of beam interception power between the input and output saddles must also be estimated.

(3) Internal rf losses - These losses are estimated from computer calculations and cold-test measurements.

(4) External rf losses (in the output waveguide instrumentation coupler used to measure forward and reflected power) - These losses can be fairly accurately calculated from cold-test measurements and are about 5 percent of the rf output power.

The total heat rejected by an OST can be measured during thermal-vacuum tests. Accurate thermal-vacuum test data are available for OST 2030. OST 2022R1 was not retested in a thermal-vacuum environment after its final hot-refocus operation because of a schedule problem. However, electrical data obtained at TRW, coupled with the results of the pre-hot-refocus thermal-vacuum tests, allow us to fix the total waste heat output of OST 2022R1 within ± 10 watts with a high degree of confidence.

Estimates of the waste heat generated by OST 2022R1 and OST 2030 are given in table VIII. The estimates are constructed so that the total heat flow to the baseplate adds up to the known value - a measurement in the case of OST 2030, and a measurement with correction for refocusing in the case of OST 2022R1. Thus the main reason for this exercise is to apportion the experimentally determined heat flow between the input and output saddles. The basis for the estimates is described in the following section.

Basis for Estimates

The estimates of waste heat generation for the OST's had the following basis:

(1) Heater dissipation - The electrical power supplied to the heater was measured. It was between 4.00 and 4.25 watts for either OST.

(2) Beam interception power - The beam interception current was measured. With no rf output the current was about 1.5 milliamperes on both tubes, and the electrons impacted with the full initial energy of 11.3 kilovolts. With no rf drive the power was assumed to be divided evenly between the input and output saddles.

With full rf output the body current increased substantially because of the defocusing effects of strong rf fields. Therefore the increased body current occurred mainly in the output region of the OST, where the rf fields are strongest. The average energy of the impacting electrons was near the average kinetic energy in the output region of the OST (~8 kV). Therefore the additional body current at full rf power was assigned an impact energy of 8 kilovolts. Most of the resulting additional power (90 percent) was assigned to the output saddle. The remaining 10 percent was assigned to the input saddle.

(3) Internal rf losses - The internal rf loss was zero when there was no rf drive. At full rf power the internal rf loss was between 30 and 50 percent of rf output power. Because this is the loss term that we are least capable of estimating accurately, the internal rf loss was assigned whatever value was required to achieve the proper total. Most of the rf loss occurred in the output region of the OST, where the rf currents are greatest. Therefore the resultant waste heat flow was assigned mainly (90 percent) to the output saddle.

(4) External rf losses - The percentage loss in the rf output coupler was measured by Litton. They quote 0.2 decibel (~4.5 percent) for both tubes. The methods used are probably accurate to within ± 0.05 decibel.

REFERENCES

1. Alexovich, Robert E.: Performance of the 12 GHz, 200 Watt Transmitter Experiment Package for the Hermes Satellite. NASA TM-73804, 1977.
2. Kosmahl, Henry G.; McNary, B. D.; and Sauseng, Otto: High Efficiency, 200-Watt, 12-Gigahertz Traveling Wave Tube. NASA TN D-7709, 1974.
3. Kosmahl, Henry G.: A Novel, Axisymmetric, Electrostatic Collector for Linear Beam Microwave Tubes. NASA TN D-6093, 1971.
4. Early Performance of the 12-GHz, 200-Watt Transmitter Experiment Package in the Communications Technology Satellite. NASA TM X-3555, 1977.
5. Farber, B. F.; et al.: Transmitter Experiment Package for the Communications Technology Satellite. (TRW Defense and Space Systems Group; NASA Contract NAS3-15839.) NASA CR-135035, 1977.
6. Curren, Arthur N.: Thermal Characteristics of the 12-Gigahertz, 200-Watt Output Stage Tube for the Communications Technology Satellite. NASA TP-1344, 1978.
7. Marcus, B. D.: CTS TEP Thermal Anomalies - Heat Pipe System Performance. (TRW Defense and Space Systems Group; NASA Contract NAS3-21012.) 1977.
8. Reza, Fazlollah M.; and Seely, Samuel: Modern Network Analysis. McGraw-Hill Book Co., Inc., 1959.
9. Mildrum, Herbert F.; and Strnat, Karl J.: Research to Investigate the Aging Characteristics of Samarium Cobalt Magnets. UDRI-TR-74-18, Univ. Dayton Research Inst., 1974. (AFML-TR-74-50, AD-779033.)
10. Campbell, W. A., Jr.; Marriott, R. S.; and Park, J. J.: An Outgassing Data Compilation of Spacecraft Materials. NASA RP-1014, 1978.

TABLE I. - TEP TELEMETRY MEASUREMENTS AND RANGES

[All temperature sensors are thermistors unless otherwise indicated.]

Cathode heater voltage, V dc	0 to 10
Cathode voltage, kV dc	0 to -15
Beam current, mA	0 to 100
Body current, BODY, mA	0 to 15
Anode voltage, V dc	0 to 600
Collector 4 voltage, kV dc	0 to -10
Collector 5 voltage, kV dc	0 to -10
Collector 7 voltage, kV dc	0 to -10
Collector 1 current, mA	0 to 15
Collector 2 current, mA	0 to 15
Collector 3 current, mA	0 to 25
Collector 4 current, mA	0 to 25
Collector 5 current, mA	0 to 25
Collector 6 current, mA	0 to 25
Collector 7 current, mA	0 to 25
Collector 8 current, mA	0 to 40
Collector 9 current, mA	0 to 40
Collector 10 current, mA	-10 to 5
PPS component temperature, °C	-55 to 150
PPS baseplate temperature, °C	-55 to 100
TWT body temperature ^a , BODY, °C	-15 to 150
MDC temperature at position 1 ^a , TMDC1, °C	25 to 225
MDC temperature at position 2 ^a , TMDC2, °C	-15 to 150
Coupler temperature ^a , CPLR, °C	-15 to 150
Reflected rf power ^a , W	0 to 25
Forward rf power ^a , V dc	0 to 5
Envelope internal pressure, µA	0 to 10
Housekeeping bus current, A	0 to 1.5
Experimental bus current, A	0 to 10
Signal conditioning reference voltage, V dc	0 to 5
Heat pipe 6 temperature ^b , HP6T, °C	-100 to 95
Heat pipe 1 temperature, HP1T, °C	-75 to 80
Heat pipe 2 temperature, HP2T, °C	-75 to 80
Heat pipe 3 temperature, HP3TA, °C	-75 to 80
Heat pipe 4 temperature, HP4T, °C	-75 to 80
Heat pipe 5 temperature ^b , HP5T, °C	-100 to 95
Shutdown fault indicator, V:	
Normal	5
Pressure trip	3
Body-current trip	1.5
Undervoltage trip	0

^aSensors in OST.^bPlatinum resistance thermometers.

TABLE II. - NONMETALLIC MATERIALS USED IN OST FABRICATION (FROM REF. 10)

[Samples tested for 24 hr at 120⁰ C in 1×10⁶-torr atmosphere.]

Material	Manu- facturer ^a	Total weight loss, percent	Collected volume of condensable material, percent	Cure conditions		
				Time, hr	Temp- erature, °C	Atmos- phere
Hardware: laminated FR-4 G-11 epoxy/fiber glass	A	0.31	0.01	-----	---	-----
Sealants:						
RTV 11 silicone	B	.91	.55	24	150	Air
Stycast 2850 FT/9	C	.25	.01	-----	---	---
Adhesives:						
Eccobond 56C/9	C	.42	.03	16	65	Air
Epoxy-Patch Kit 0151 A/B	D	.78	.02	24	25	Air
Lefkowitz 46/LM-52	E	1.04	.08	3	66	Air
Tape: Mystik Tape 7361 Kapton/Silicone ADH/F	F	.92	.27	115	25	0.013 N/m ²
Paint: Sperex SP-101 VHT High Temperature; coating, white silicone	G	0.29	.01	.25	25	Air

^aManufacturer list:

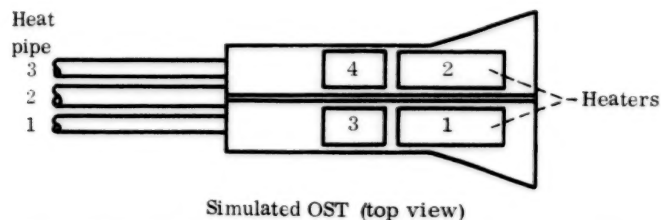
- A The Mica Corp., Culver City, Cal.
- B General Electric Co., Silicone Products Dept., Waterford, N. Y.
- C Emerson and Cuming, Inc., Pennsauken, N. J.
- D The Dexter Corp., Hysol Division, Clean, N. Y.
- E Leffingwell Chemical Co., Berea, Cal.
- F The Borden Co., New York, N. Y.; Mystik Tape, Northfield, Ill.
- G Sperex Corp., Gardena, Cal.

TABLE III. - OST THERMAL-VACUUM TESTS

Test	Test description ^a		
	OST rf output power, W (nom.)	OST baseplate temperature, °C (nom.)	Configurations/sequences
1	200	35	OST baseplate - calorimeter interface unclamped
2	↓	↓	OST baseplate - calorimeter interface unclamped on waveguide side only
3			OST bus bar - saddle interfaces on waveguide side unclamped
4			OST bus bar - saddle interface at out- put waveguide position unclamped
5			All OST bus bar - saddle interfaces unclamped
6		56	Thermal equilibrium attained. Then coolant flow reduced to zero and lines purged
7		56	Thermal equilibrium attained. Then cooling reduced to 20 percent
8		56	Thermal equilibrium attained. Then cooling reduced to 50 percent
9		55	} Thermal equilibrium attained. Then coolant flow reduced to zero and lines quickly purged
10		45	
11	100	45	
12	100	35	
13	50	40	
14	50	30	
15	0	35	
16	0	25	

^a For all tests, the OST was operated at center-band frequency, 12.080 GHz.

TABLE IV. - SUMMARY OF RESULTS OF ROOM-AMBIENT VCHPS TESTS
(EQUILIBRIUM DATA)



Simulated OST (top view)

Reading or instrument	Tests					
	1	2	^a 3	4	5	6
	Normal case; 158 W; symmetrical heating (all heat pipes on)	Asymmetrical heating; 159 W; all on HP3, side; all heat pipes on	Asymmetrical heating; 158 W; baseplate over HP1 removed; all heat pipes on	Symmetrical heating; 158 W; HP1 failed; HP2 and HP3 on	Symmetrical heating; 158 W; HP1 and HP2 failed; HP3 on	Symmetrical heating; 38 W; all heat pipes failed
Heater 1, W	60.6	0	0	60.6	60.6	18.2
Heater 2, W	68.9	131.1	129.5	68.9	68.9	19.6
Heater 3, W	14.3	0	0	14.3	14.3	0
Heater 4, W	14.5	28.0	28.0	14.5	14.5	0
HP1, s.d.l., °C	51.4	50.8	51.2	54.3	59.7	60.0
HP2, s.d.l., °C	51.7	51.4	51.7	54.2	59.0	59.3
HP3, s.d.l., °C	52.1	52.8	53.2	54.3	57.4	58.6
HP1, side, °C	49.7	48.9	49.6	47.1	46.7	45.6
HP2, side, °C	49.8	49.7	50.0	51.8	50.0	46.9
HP3, side, °C	51.1	51.8	52.6	52.8	55.6	47.9
HP1, bot., °C	50.6	49.6	50.2	47.9	47.4	45.7
HP2, bot., °C	50.2	50.2	50.2	52.5	50.7	46.8
HP3, bot. ^b , °C	49.6	50.4	51.2	51.3	54.1	46.5
BODY, °C	84.4	54.4	62.6	90.4	107.4	82.2
HP1T, °C	45.6	44.4	47.8	44.4	43.3	44.4
HP2T, °C	46.7	46.7	48.3	50.0	46.7	45.6
HP3T, °C	46.7	46.7	50.0	50.0	51.1	46.7
HP4T, °C	46.7	45.6	48.3	46.7	44.4	43.9

^aHeat-pipe turnon order: 3-2-1.

^bInstrument not electrically grounded.

TABLE V. - EVENT CHRONOLOGY FOR
[TEP operations all at center-band frequency]

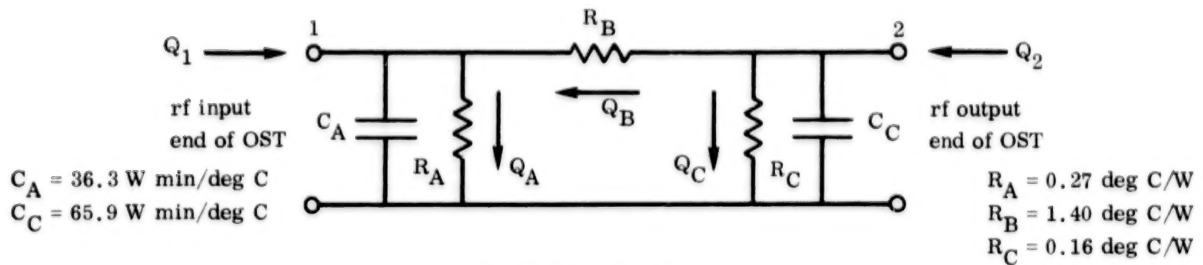
Time		Telemetry						
GMT	EDT	Radio-frequency output power, W	OST body temperature, BODY, °C	Coupler temperature, CPLR, °C	Flange temperature, TMDC2, °C	Heat-pipe-1 adiabatic temperature, HP1T, °C	Heat-pipe-2 adiabatic temperature, HP2T, °C	Heat-pipe-3 adiabatic temperature, HP3TA, °C
12:45	8:45	-----	-----	-----	-----	-----	-----	-----
12:47	8:47	198.4	26.6	25.1	22.9	-9.4	-9.4	-9.4
13:02	9:02	203.5	42.3	46.3	33.9	-7.6	-9.8	-10.3
13:12	9:12	201.5	45.8	55.3	43.1	27.1	- .3	-4.5
13:42	9:42	190.7	49.9	68.1	59.2	30.7	30.7	25.5
14:02	10:02	198.5	50.9	71.7	63.4	29.0	29.0	27.1
14:20	10:20	-----	-----	-----	-----	-----	-----	-----
14:22	10:22	196.2	52.2	73.4	66.5	30.7	32.6	32.6
14:27	10:27	194.3	54.5	74.0	67.6	28.9	30.7	32.6
14:32	10:32	196.7	55.5	74.6	68.1	30.7	32.6	34.6
14:57	10:57	204.6	63.9	79.2	74.8	28.9	30.7	32.8
15:02	11:02	146.1	64.9	79.7	76.4	29.0	30.9	32.6
15:07	11:07	177.9	65.5	79.7	77.1	28.9	30.7	34.6
15:42	11:42	185.3	70.1	82.5	81.8	28.9	30.7	32.6
15:47	11:47	163.7	71.2	82.7	85.0	28.9	30.7	30.9
15:57	11:57	160.7	70.3	82.5	82.5	27.1	28.9	32.6
16:23	12:23	197.1	70.7	82.5	82.5	27.1	28.9	30.7
16:28	12:28	213.7	71.7	84.0	83.2	27.1	28.9	30.7
16:33	12:33	134.1	74.6	86.3	84.7	27.3	29.0	32.6
16:38	12:38	128.7	73.6	-----	-----	-----	-----	-----
16:43	12:43	124.0	72.3	-----	-----	-----	-----	-----
16:48	12:48	138.5	71.4	-----	-----	-----	-----	-----
16:53	12:53	133.8	70.7	-----	-----	-----	-----	-----
16:58	12:58	133.6	69.3	-----	-----	-----	-----	-----
17:03	13:03	133.8	69.1	-----	-----	-----	-----	-----
17:08	13:08	199.5	68.1	80.4	81.1	-----	-----	-----
17:13	13:13	206.7	70.7	82.5	81.8	-----	-----	-----
17:18	13:18	153.6	72.8	84.7	83.2	-----	-----	-----
17:23	13:23	141.4	72.8	83.2	84.0	-----	-----	-----
17:30	13:30	139.0	71.2	81.8	84.0	-----	-----	-----
17:35	13:35	141.4	70.7	81.1	83.2	-----	-----	-----
17:40	13:40	143.6	70.1	80.4	82.5	-----	-----	-----
17:45	13:45	149.0	69.3	80.4	82.5	-----	-----	-----
17:51	13:51	141.1	69.1	80.4	81.8	-----	-----	-----
17:55	13:55	~0	68.3	79.0	81.8	-----	-----	-----
18:00	14:00	↓	64.4	73.4	80.4	-----	-----	-----
18:05	14:05	↓	61.3	68.1	77.7	27.1	28.9	30.7
18:10	14:10	↓	59.7	-----	-----	-----	-----	-----
18:52	14:52	↓	46.8	47.4	60.7	-----	-----	-----
19:11	15:11	↓	44.3	43.8	58.1	25.5	25.5	22.4
19:42	15:42	↓	41.8	40.3	55.0	23.9	25.5	14.1
19:47	15:47	205.3	41.3	-----	-----	-----	-----	-----
20:01	16:01	201.6	48.9	60.2	60.7	-----	-----	-----
20:16	16:16	199.4	52.5	69.6	67.1	25.5	27.1	25.9
21:04	17:04	191.1	57.6	77.7	72.8	27.1	30.7	32.6
21:14	17:14	199.0	58.1	78.4	72.3	-----	-----	-----
21:19	17:19	199.0	58.7	79.0	72.8	25.6	27.3	34.6
20:20	17:20	-----	-----	-----	-----	-----	-----	-----
20:32	17:32	-----	-----	-----	-----	-----	-----	-----

TEP (THERMAL ANOMALY) DAY 253

(12.080 GHz) with color-bar modulation.]

data				Events and comments
Heat-pipe-1 condenser temperature, HP4T, °C	Heat-pipe-1 reservoir-end temperature, HP5T, °C	Heat-pipe-1 gas-reservoir temperature, HP6T, °C	Temperature difference, HP3T - HP1T, HP31A, °C	
-----	-----	-----	-----	Lewis began uplink operation
-42.6	-63.2	-59.9	0	First telemetry hard-copy data
-46.2	-66.5	-63.2	-2.7	Heat pipes still inactive (<25° C)
-16.4	-69.6	-63.2	-31.6	Heat pipe 1 becomes active
-30.7	-75.7	-69.6	-5.2	All heat pipes now active
29.0	-79.9	-70.1	-1.9	Near thermal stability
-----	-----	-----	-----	Approximate end of thermal stability
30.7	-81.5	-75.7	1.9	Thermal anomaly period
30.7	-84.3	-75.7	3.7	
30.7	-84.3	-75.7	3.9	↓
28.9	-84.3	-78.7	3.9	
29.0	-85.4	-79.9	3.6	rf output power reduced
28.9	-87.1	-81.5	5.7	-----
28.9	-89.7	-84.3	3.7	-----
28.9	-----	-87.1	2.0	rf output power reduced
28.9	-92.3	-----	5.5	-----
27.1	-92.3	-89.7	3.6	rf output power increased
27.1	-92.3	-89.7	3.6	TEP at saturated rf output power
27.3	-93.2	-90.7	5.3	rf output power reduced to ~134 W
-----	-----	-----	5.5	Stable body temperature
-----	-----	-----	3.6	↓
-----	-----	-----	-----	↓
-----	-----	-----	-----	rf output power increased
-----	-----	-----	5.5	Anomaly retriggered
-----	-----	-----	5.5	rf output power reduced
-----	-----	-----	3.6	rf output power at ~140 W
-----	-----	-----	5.1	Apparent stable condition
-----	-----	-----	5.1	↓
-----	-----	-----	3.6	
-----	-----	-----	5.1	↓
-----	-----	-----	3.6	rf output power reduced to zero
-----	-----	-----	3.6	Zero rf output power
27.1	-94.8	-97.2	3.6	↓
-----	-----	-----	3.6	
-----	-----	-----	1.7	
25.5	-97.2	-101.7	-3.1	Gas-vapor front in heat pipe 1 moves in
-5.1	-99.5	-101.7	-9.8	rf output power increased
-----	-----	-----	-11.4	
-----	-----	-----	5.0	Anomaly retriggered
25.5	-101.7	-----	3.4	-----
27.1	-99.5	-101.7	7.1	-----
-----	-----	-----	5.5	Anomaly still present
25.6	-98.1	-----	9.0	-----
-----	-----	-----	-----	Telemetry lost because of power failure at Goldstone
-----	-----	-----	-----	Testing discontinued

TABLE VI. - OST EQUIVALENT THERMAL NETWORK AND ANALYSIS SUMMARY



Equivalent network

Anomaly day, 1977	Curve segment (fig. 23)	Curve slope, $\Delta T/\Delta t$, deg C/min	Experimental values		Calculated values					OST body temperature, BODY, °C
			OST body heat generated, W	Heat-loss components, W					Baseplate heat rejected, W	
				Q_1	Q_2	Q_A	Q_B	Q_C		
75	A+	1.36	138.0	22	116	-23.9	6.83	19.5	-4.3	56
	BC	.32	141.5	22.5	119	17.8	6.94	91.0	108.8	--
	C+	-1.51	20.0	12	8	23.2	6.94	100.5	123.8	75
	D	-1.03	20.0	12	8	48.7	----	76.6	125.2	--
82	A+	0.46	123	21	102	8.9	5.76	65.9	74.8	51
	BC	.132	125	21	104	22.1	5.9	89.4	111.5	--
	C+	-1.20	28	13	15	21.3	5.9	88.2	109.5	63
	D	-----	-----	-----	---	-----	----	-----	-----	--
101	A+	1.52	147	23	125	-28.5	7.37	16.5	-12.0	57
	BC	.455	147	23	124	13.7	7.25	86.8	100.5	--
	C+	-1.36	28	13	15	19.7	7.25	97.4	117.1	73
	D	-.93	28	13	15	46.5	----	76.5	123.0	--
253	A+	0.41	146	23	123	14.4	7.29	88.7	103.1	51
	Steady state	0	106+	20	86	-----	----	-----	106.0	71

TABLE VII. - ACCELERATED AGING OF
MAGNETS IN AIR AFTER
PRESTABILIZATION^a

[Prestabilization temperature, 200^o C;
aging time in air, 3046 hr; evalua-
tion temperature, 150^o C; magnet
length-diameter ratio, 0.4.]

Lot	Total additional loss, ^b percent
1	0.35
2	.20
3	.34
4	.38

^aExcerpted from table 12 in ref. 9.

^bDrop from flux after prestabilization
treatment, expressed in percent of
this value.

TABLE VIII. - ESTIMATED HEAT-REJECTION RATES TO BASEPLATE
FOR CTS OST'S 2022R1 AND 2030

Loss mechanism	OST 2022R1				OST 2030			
	Zero rf		Full rf		Zero rf		Full rf	
	Input saddle	Output saddle	Input saddle	Output saddle	Input saddle	Output saddle	Input saddle	Output saddle
Heater dissipation, W	4	---	4	---	4	---	4	---
Beam interception, W	8	8	11	37	8	8	10	30
Internal rf loss, W	--	---	9	83	--	---	9	82
External rf loss, W	--	---	--	11	--	---	--	10
Total to saddle, W	12	8	24	131	12	8	23	122
Total to baseplate, W	20		155		20		145	

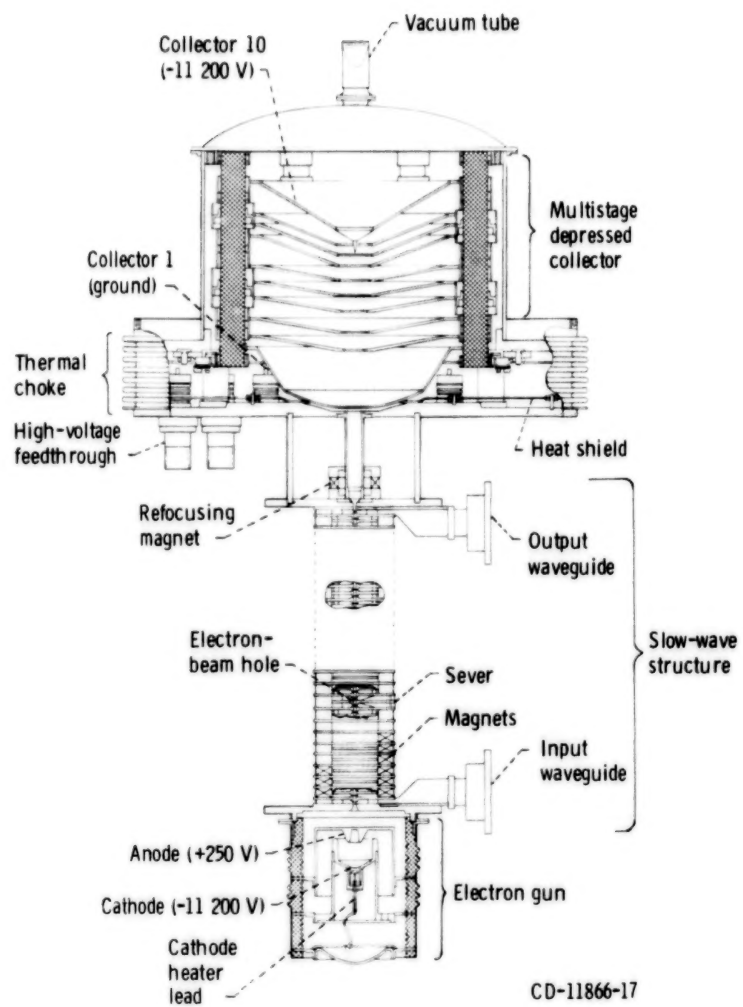


Figure 1. - CTS traveling-wave tube with multistage depressed collector.

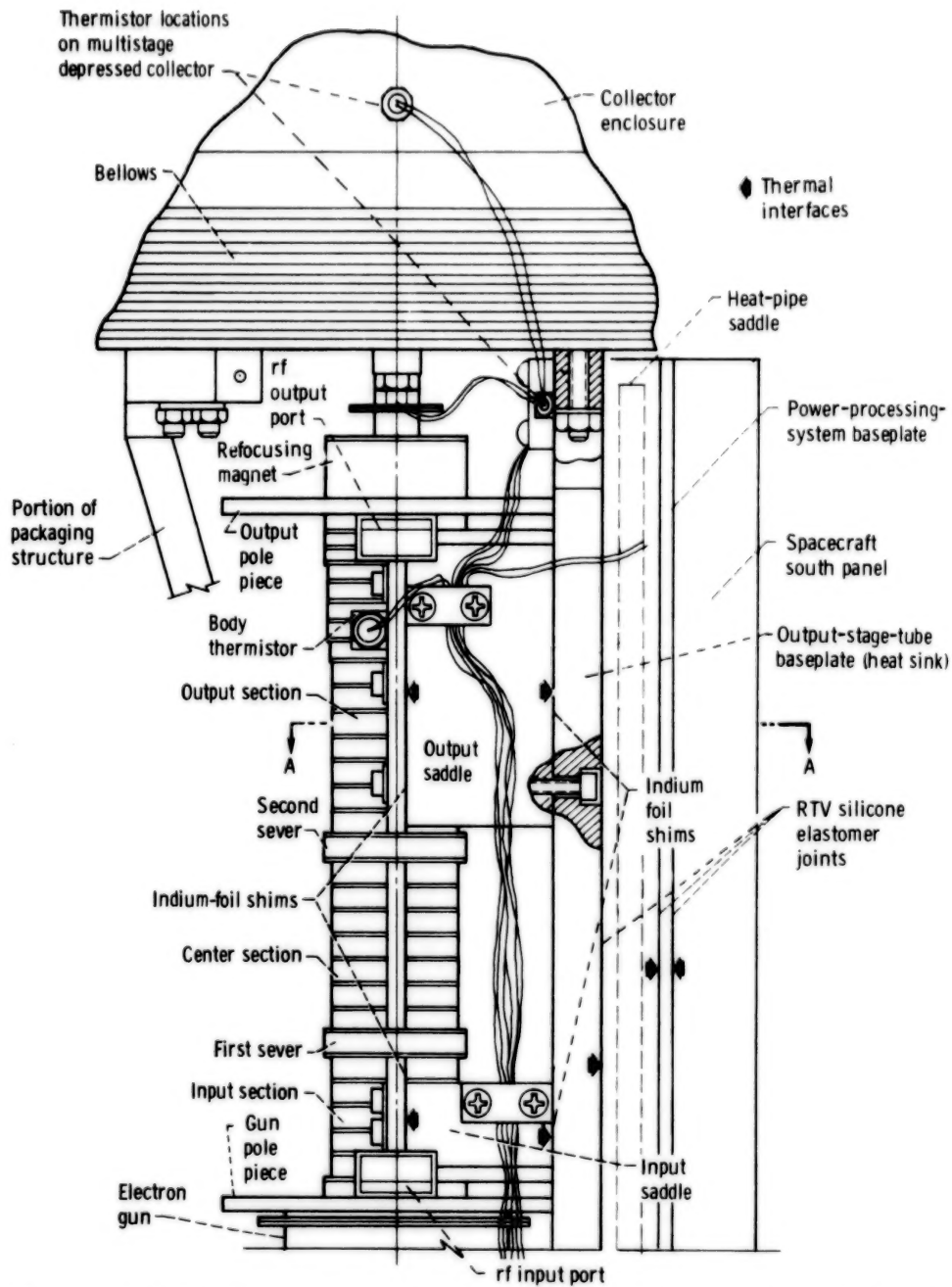


Figure 2 - Side view of CTS traveling-wave tube, showing heat-pipe saddle and spacecraft mounting details.

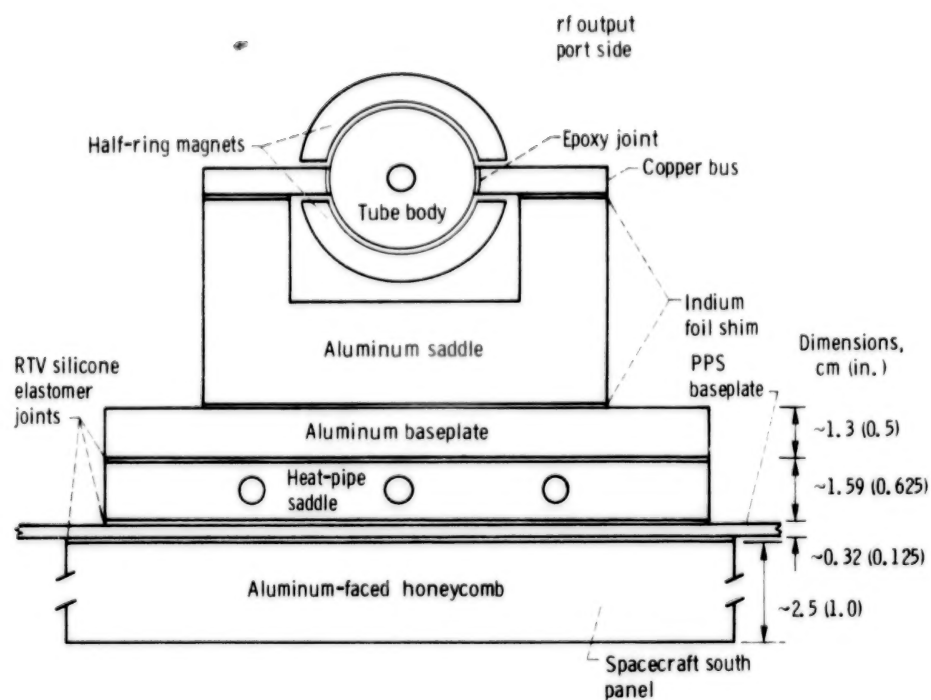


Figure 3. - Section of CTS traveling-wave tube, showing heat-pipe saddle and spacecraft mounting details. (Section taken at plane A-A of fig. 2; not to scale.)

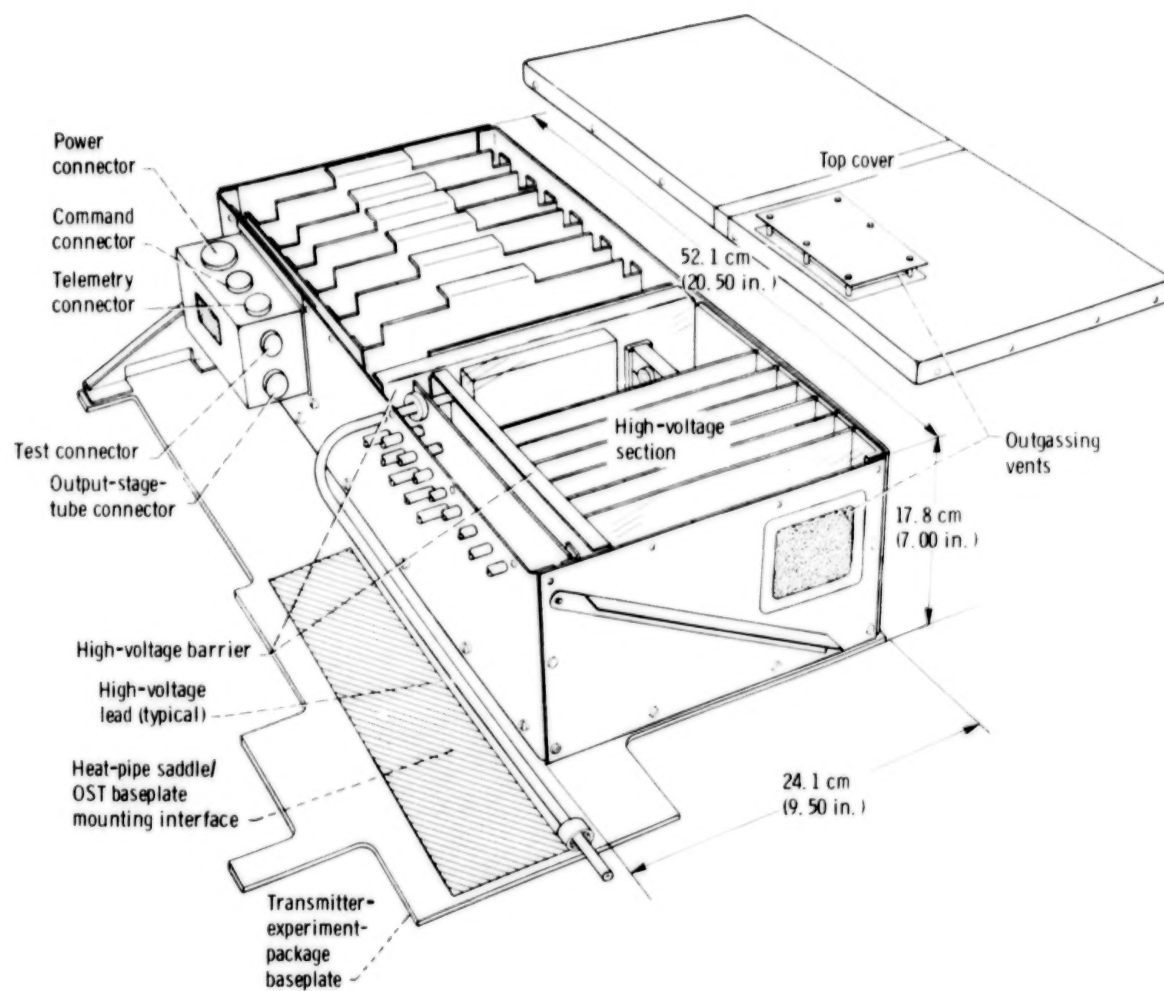


Figure 4. - CTS power-processing system.

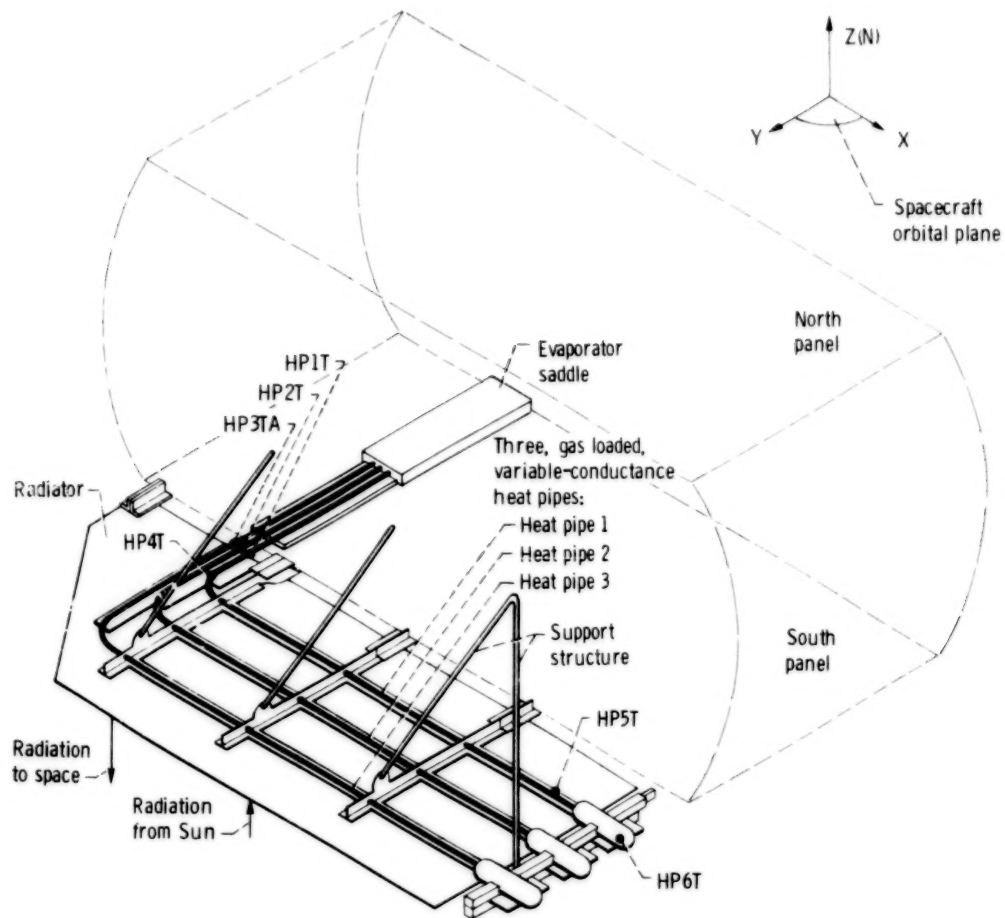


Figure 5. - CTS variable-conductance-heat-pipe system.

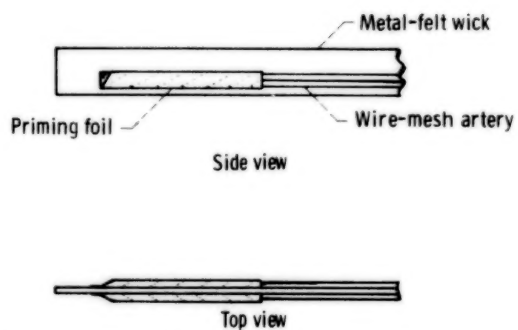


Figure 6. - CTS variable-conductance-heat-pipe wick assembly.

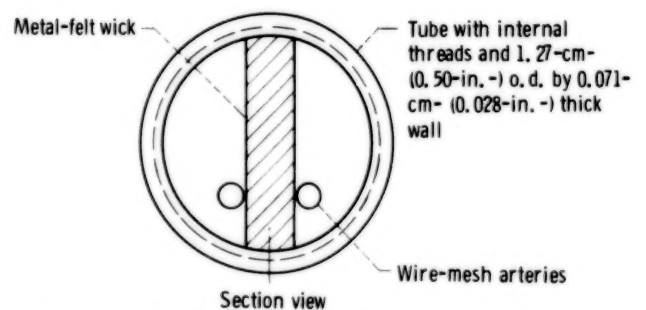


Figure 7. - CTS variable-conductance-heat-pipe wick configuration.

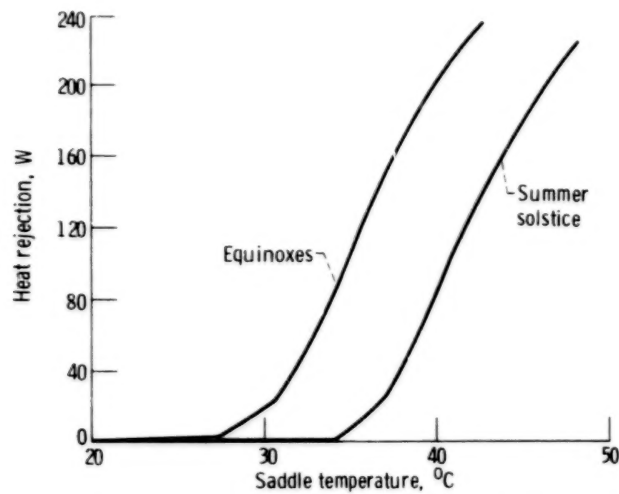


Figure 8. - Expected performance of CTS variable-conductance-heat-pipe system. (All pipes operational; design conditions.)

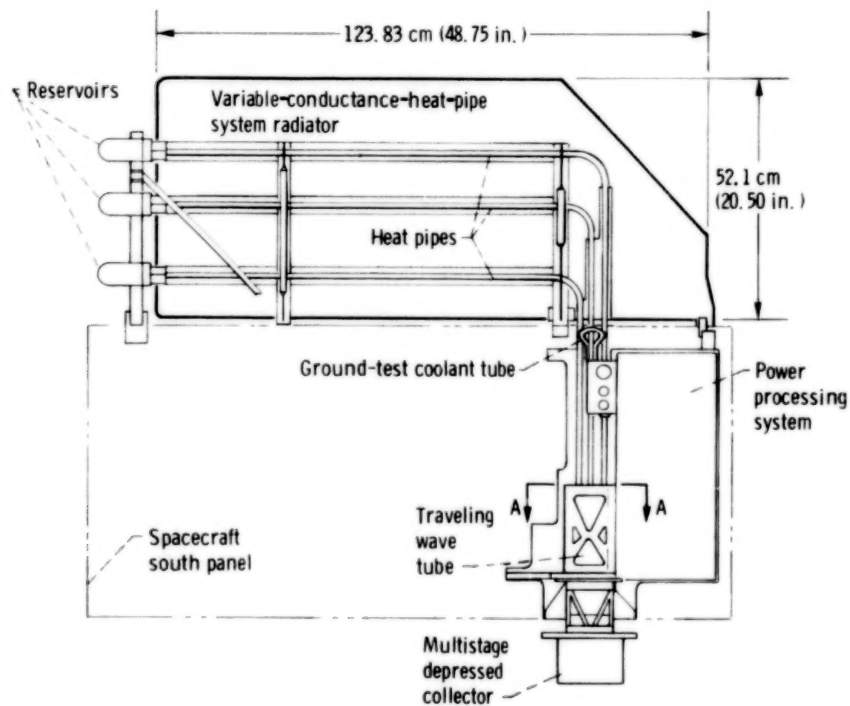
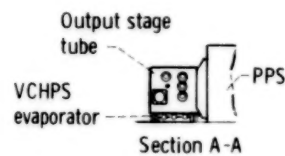
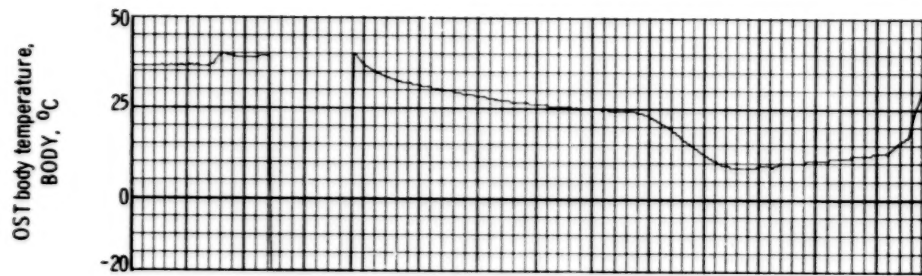
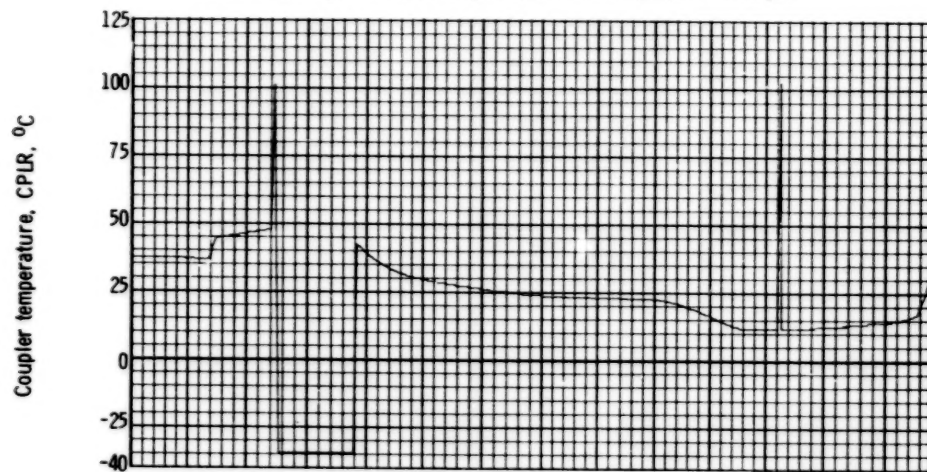


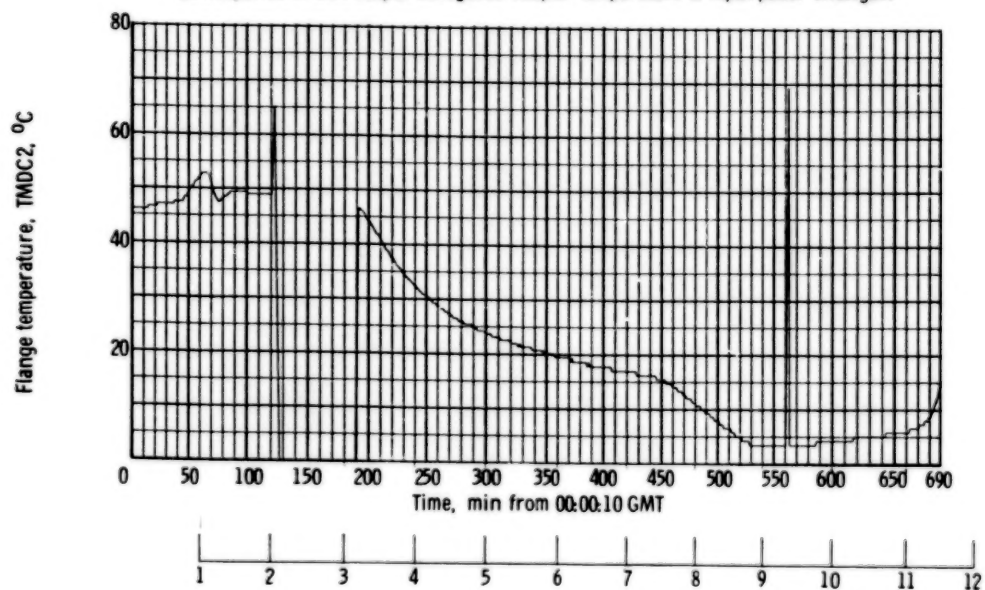
Figure 9. - CTS transmitter experiment package.



(a) Response of OST body temperature to input power changes.



(b) Response of OST output waveguide coupler temperature to input power changes.

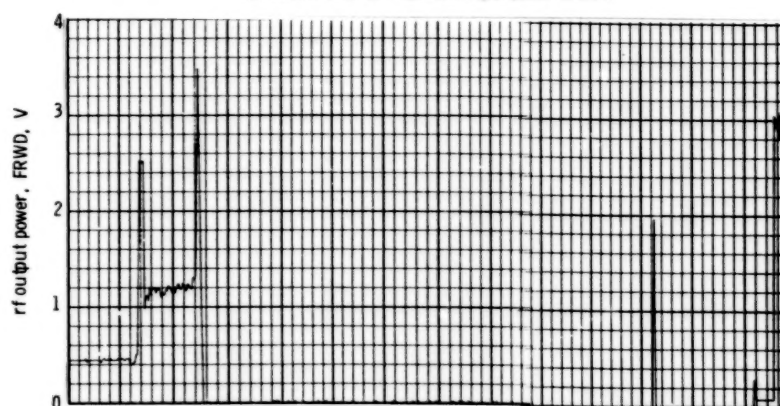


(c) Response of MDC cover flange temperature to OST input power changes.

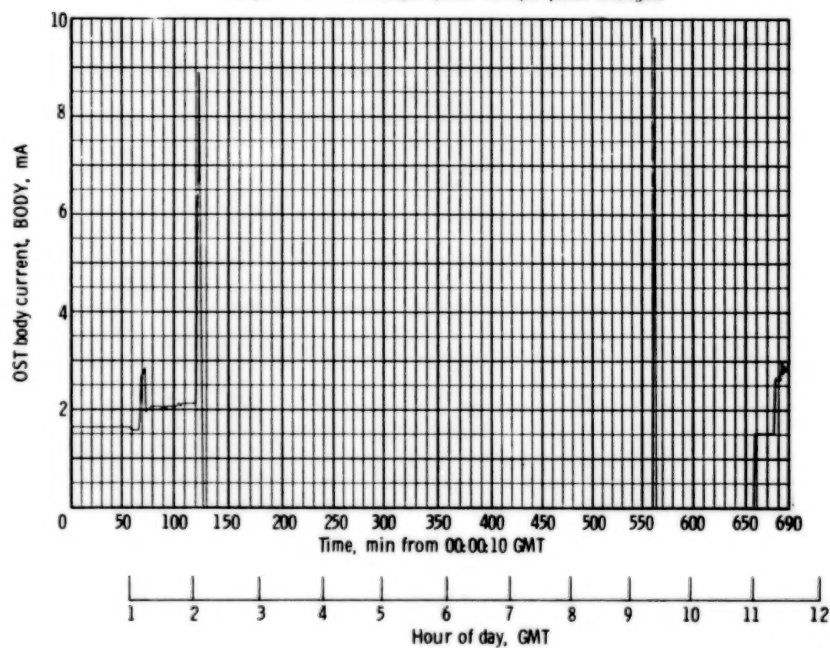
Figure 10. - Telemetry data for first half of day 89 (Mar. 30) 1977.



(d) Profile of direct-current input power to OST.

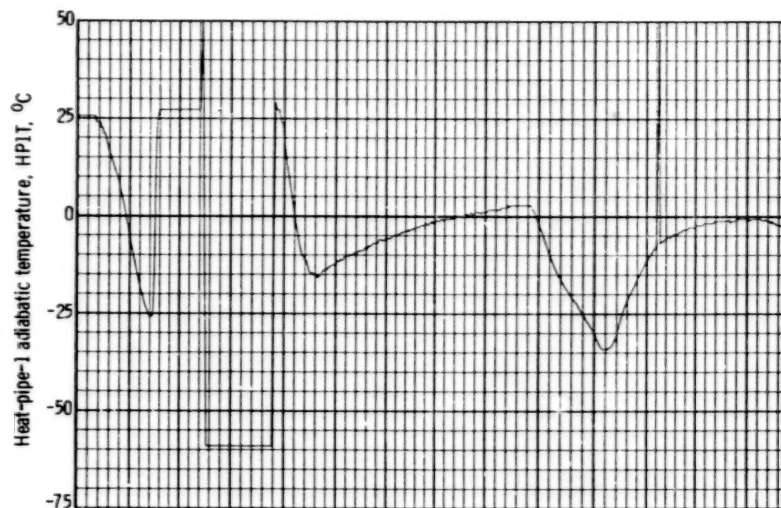


(e) Response of OST rf output power to input power changes.



(f) Response of OST body current to input power changes.

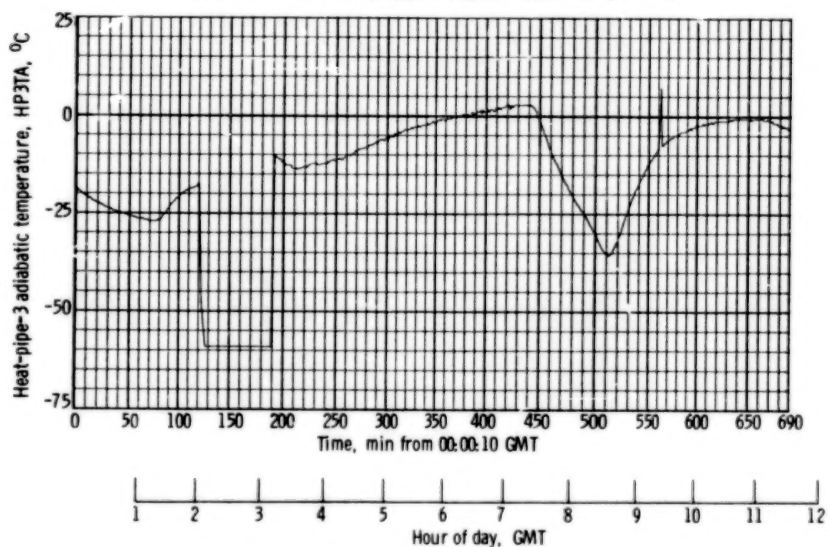
Figure 10. - Continued.



(g) Profile of VCHPS heat-pipe-1 adiabatic section temperature.

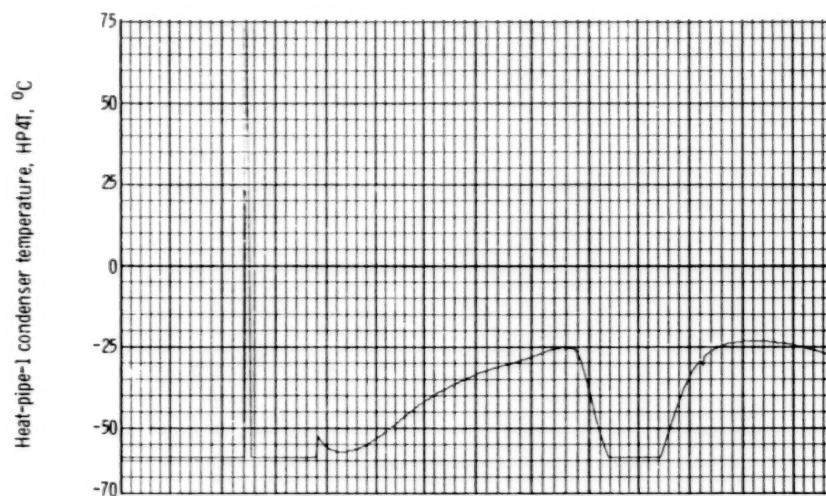


(h) Profile of VCHPS heat-pipe-2 adiabatic section temperature.

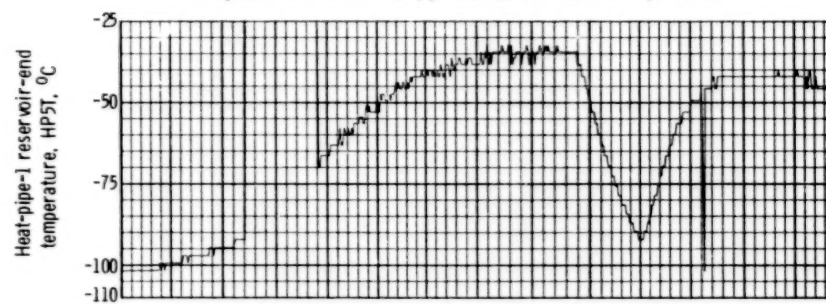


(i) Profile of VCHPS heat-pipe-3 adiabatic section temperature.

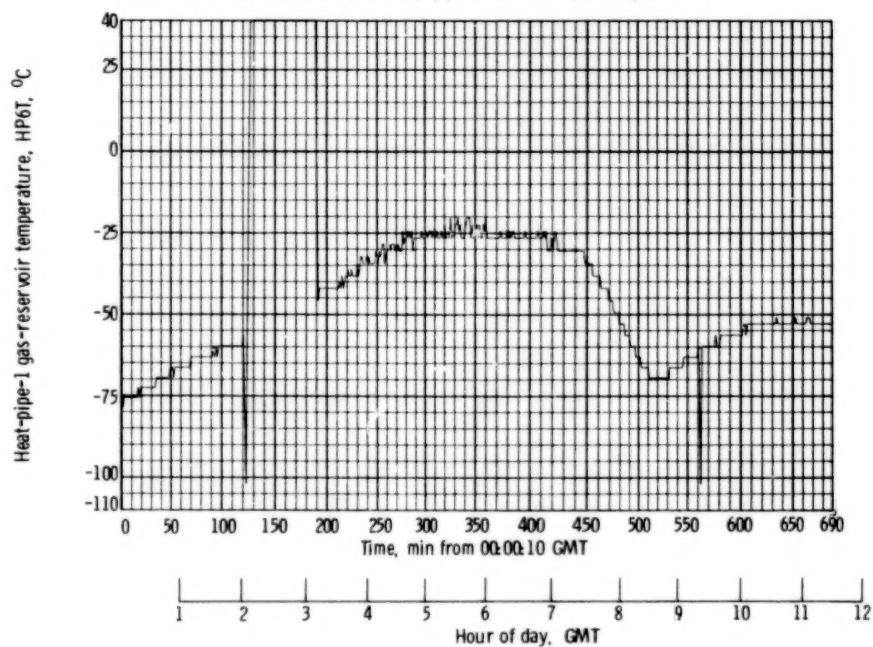
Figure 10. - Continued.



(j) Profile of VCHPS heat-pipe-1 condenser section temperature.

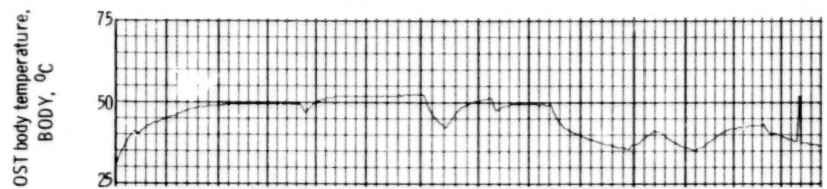


(k) Profile of VCHPS heat-pipe-1 reservoir-end temperature.

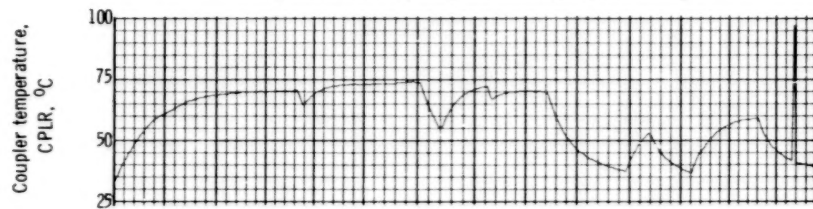


(l) Profile of VCHPS heat-pipe-1 gas-reservoir temperature.

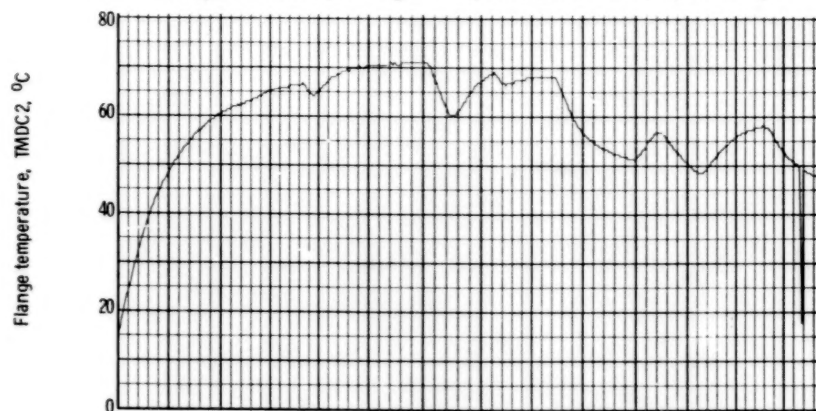
Figure 10. - Concluded.



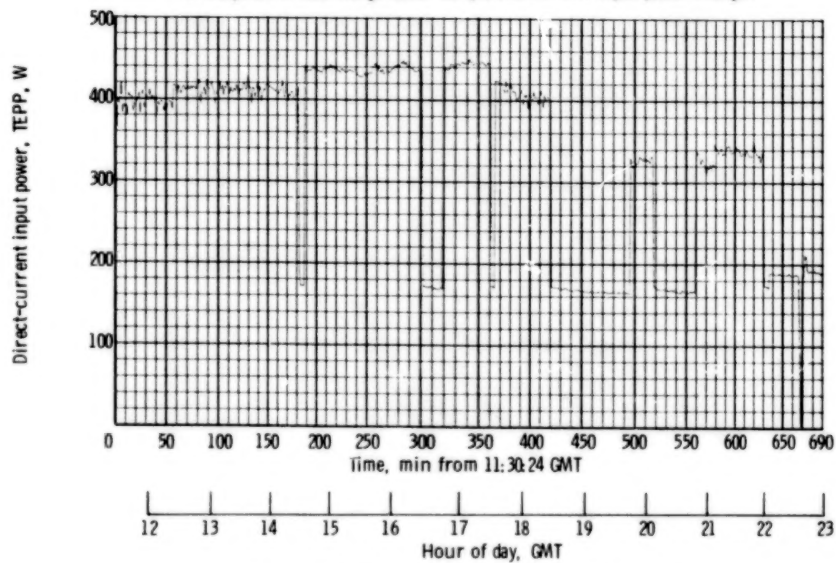
(a) Response of OST body temperature to input power changes.



(b) Response of OST output waveguide coupler temperature to input power changes.

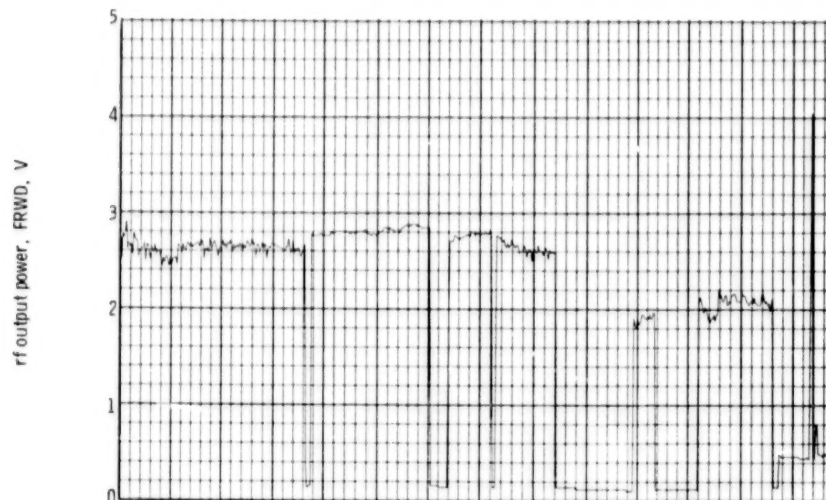


(c) Response of MDC flange cover temperature to OST input power changes.

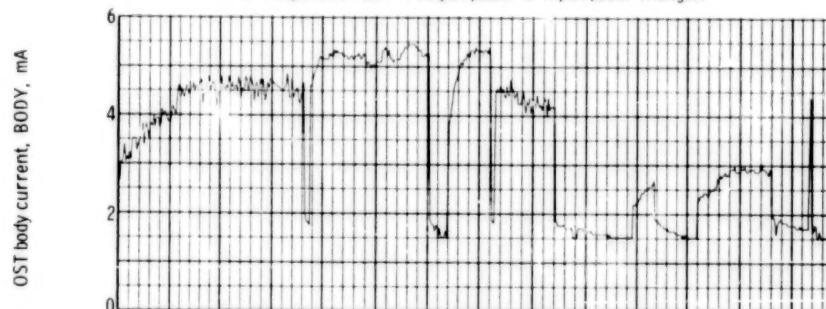


(d) Profile of direct-current electrical input power to OST.

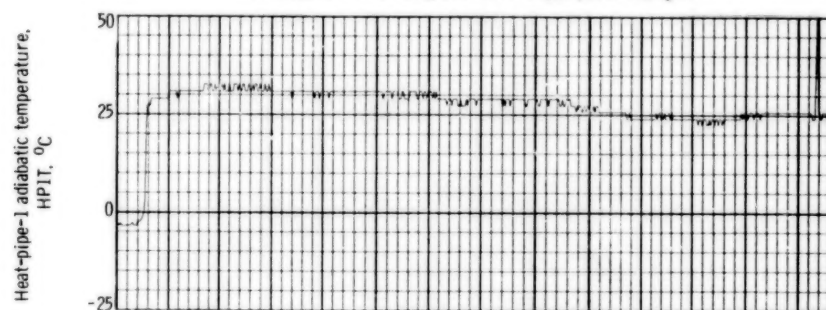
Figure 11. - Telemetry data for last half of day 89 (Mar. 30) 1977.



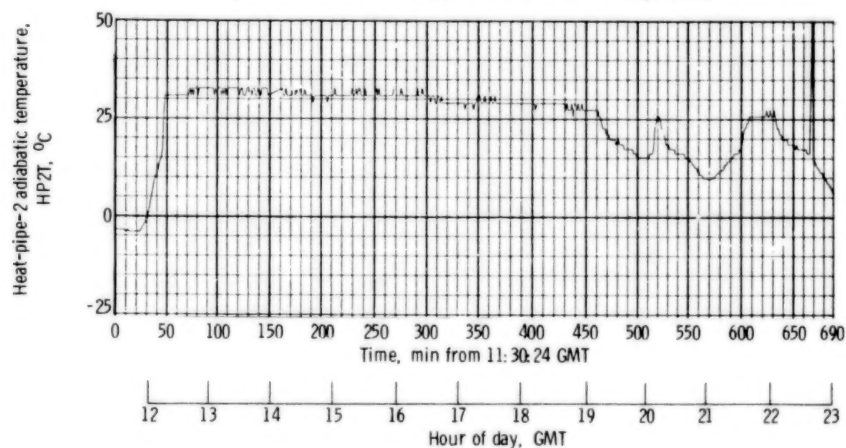
(e) Response of OST rf output power to input power changes.



(f) Response of OST body current to input power changes.



(g) Profile of VCHPS heat-pipe-1 adiabatic section temperature.

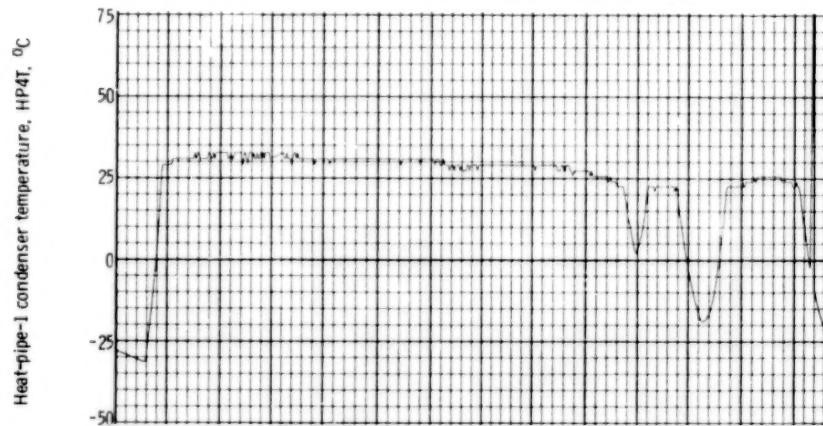


(h) Profile of VCHPS heat-pipe-2 adiabatic section temperature.

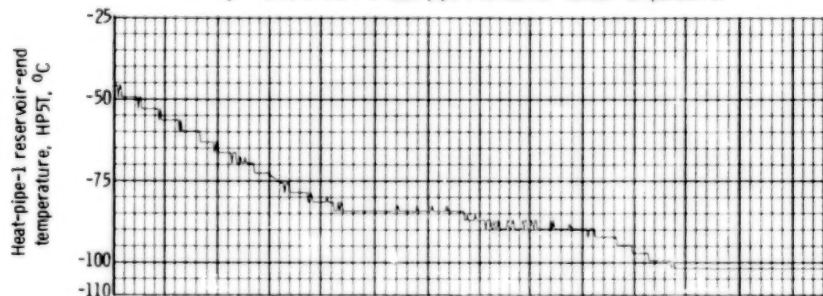
Figure 11. - Continued.



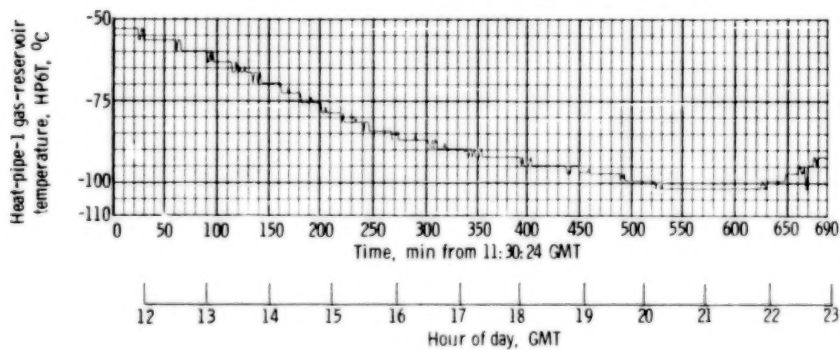
(i) Profile of VCHPS heat-pipe-3 adiabatic section temperature.



(j) Profile of VCHPS heat-pipe-1 condenser section temperature.



(k) Profile of VCHPS heat-pipe-1 reservoir-end temperature.



(l) Profile of VCHPS heat-pipe-1 gas-reservoir temperature.

Figure 11. - Concluded.

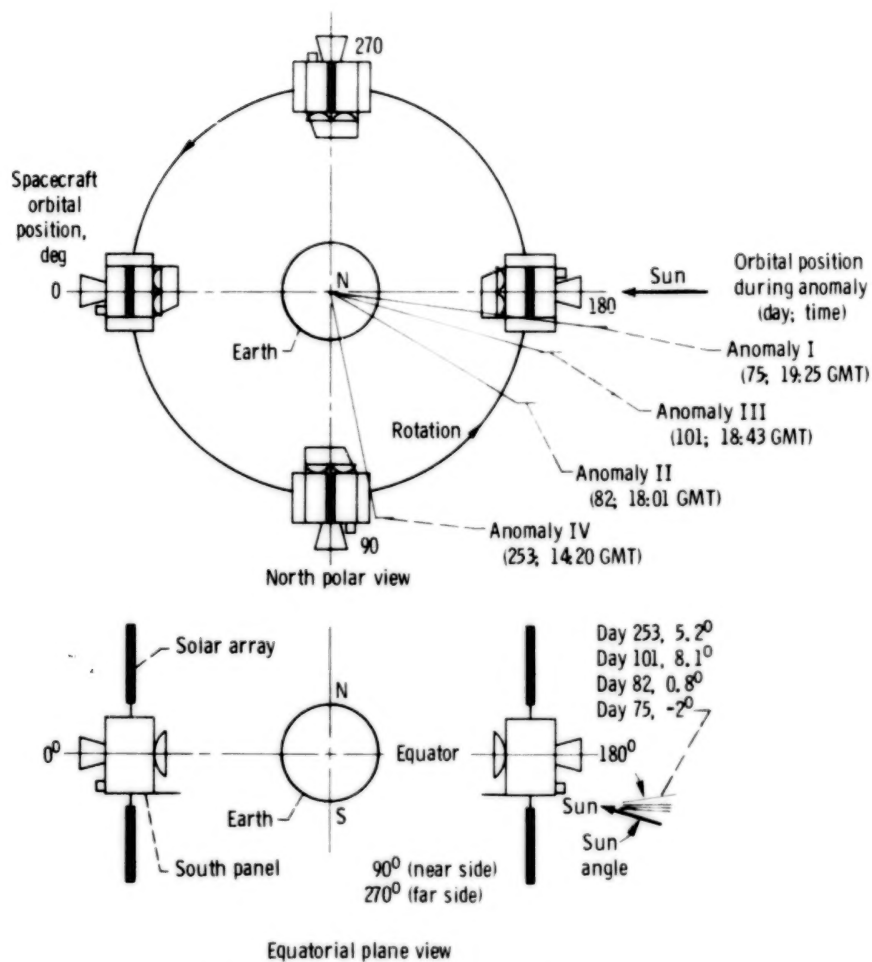


Figure 20. - CTS spacecraft orbital position and orientation with respect to Sun illumination for each TEP thermal-anomaly day.

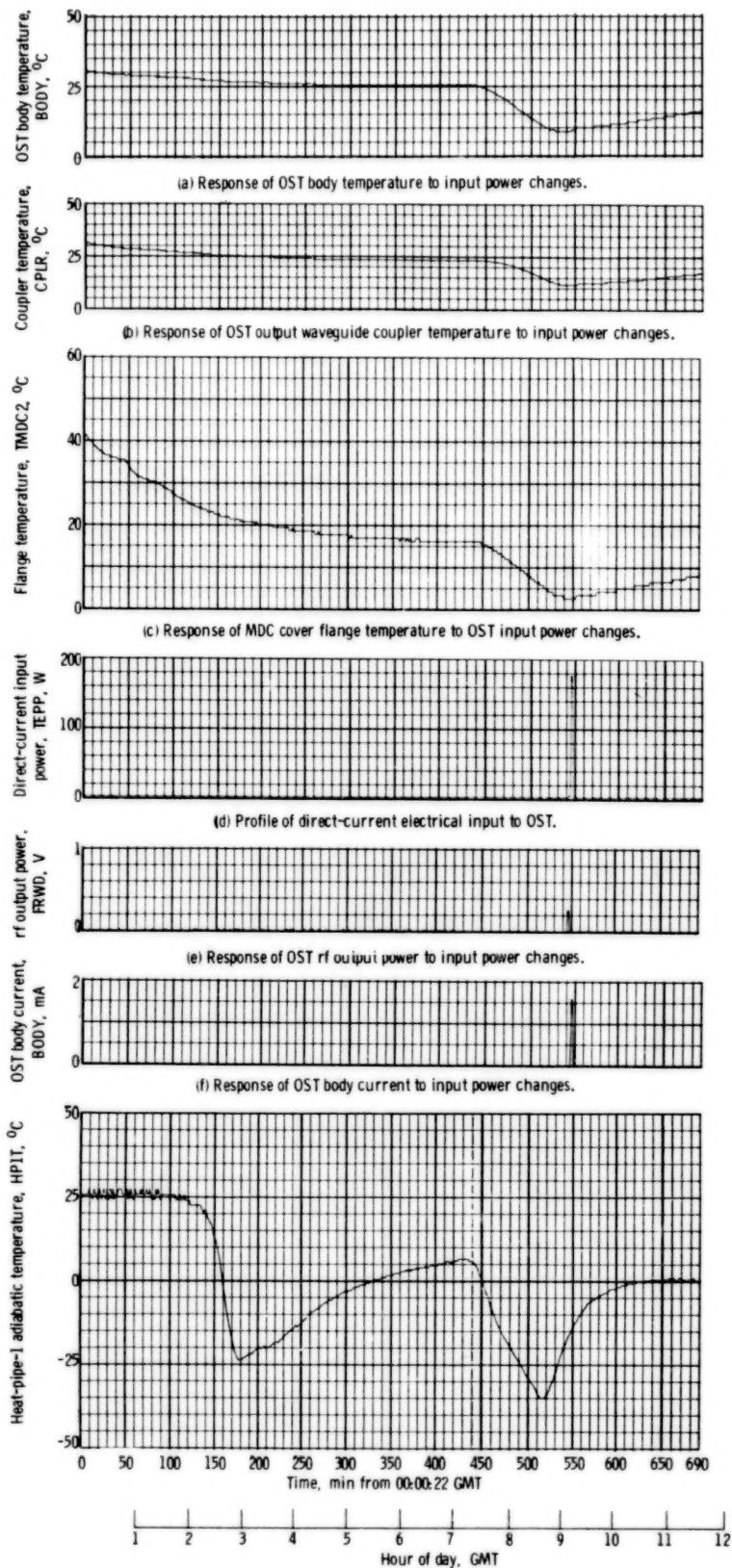
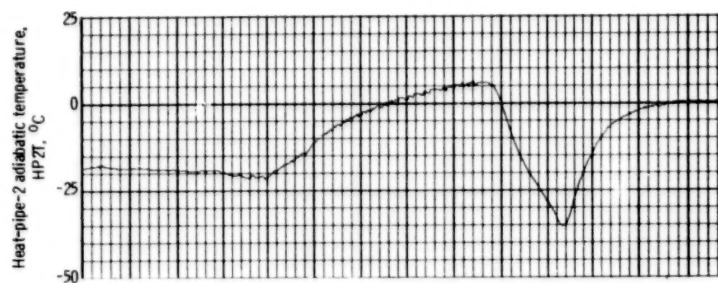
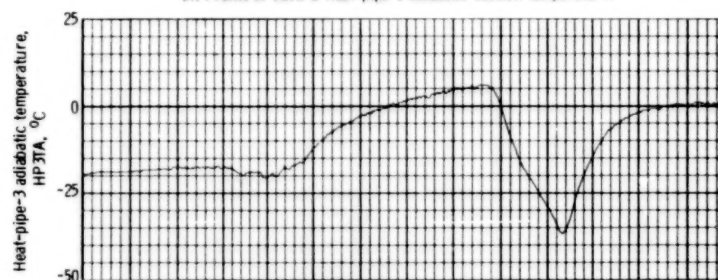


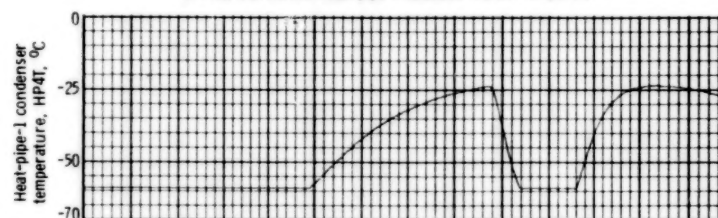
Figure 13. - Telemetry data for first half of day 75 (Mar. 16) 1977.



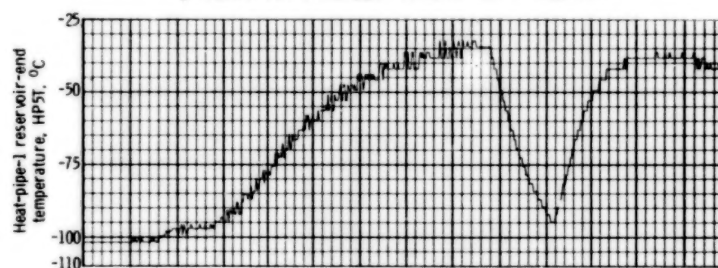
(h) Profile of VCHPS heat-pipe-2 adiabatic section temperature.



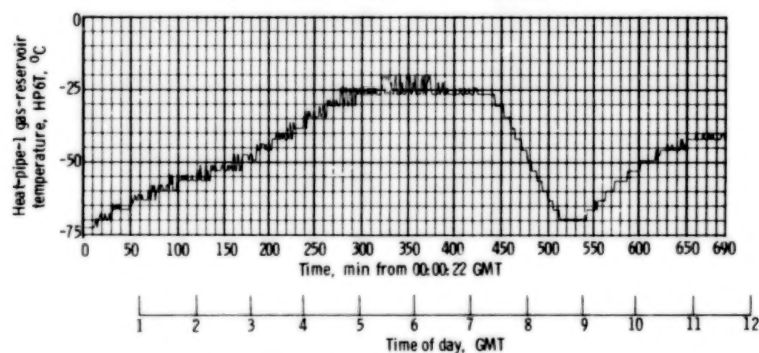
(i) Profile of VCHPS heat-pipe-3 adiabatic section temperature.



(j) Profile of VCHPS heat-pipe-1 condenser section temperature.



(k) Profile of VCHPS heat-pipe-1 reservoir-end temperature.



(l) Profile of VCHPS heat-pipe-1 gas-reservoir temperature.

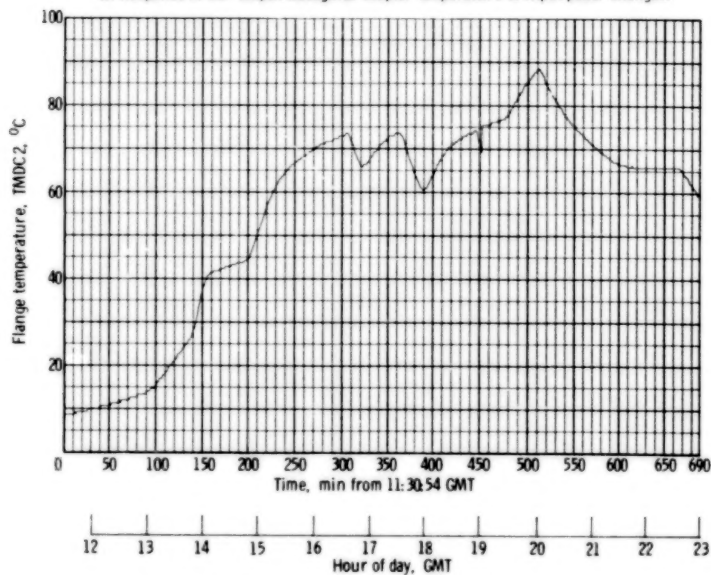
Figure 13. - Concluded.



(a) Response of OST body temperature to input power changes.

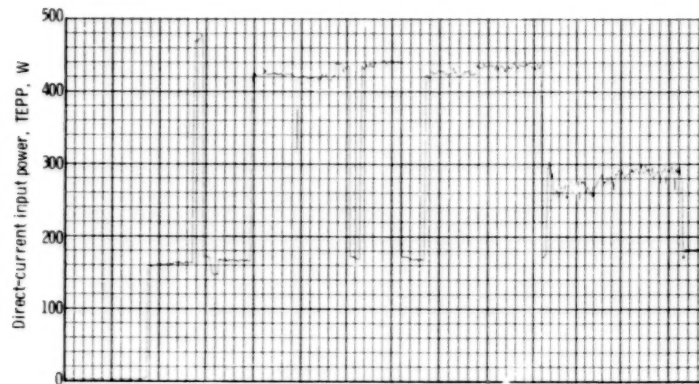


(b) Response of OST output waveguide coupler temperature to input power changes.



(c) Response of MDC cover flange temperature to OST input power changes.

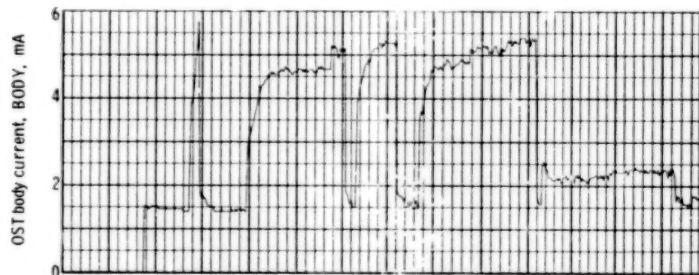
Figure 14. - Telemetry data for last half of day 75 (Mar. 16) 1977.



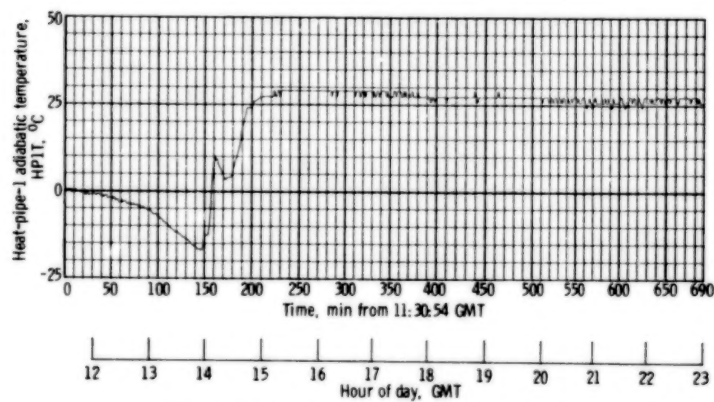
(d) Profile of direct-current electrical input power to OST.



(e) Response of OST rf output power to input power changes.

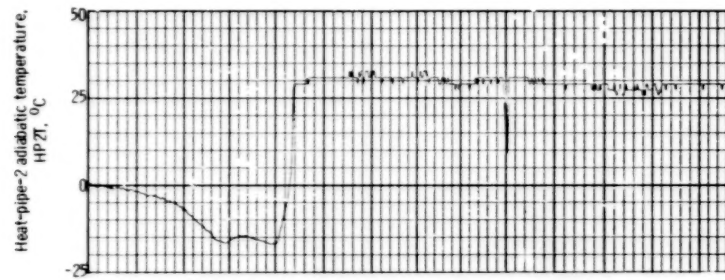


(f) Response of OST body current to input power changes.

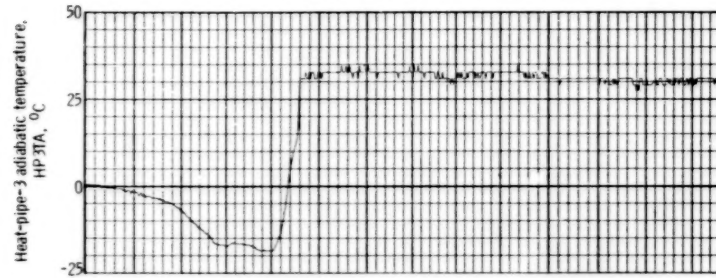


(g) Profile of VCHPS heat-pipe-1 adiabatic section temperature.

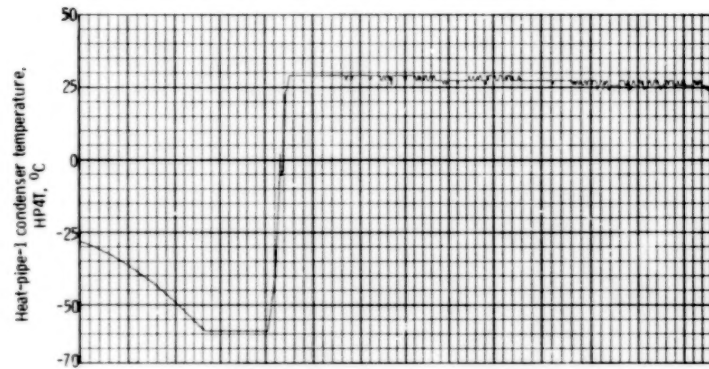
Figure 14. - Continued.



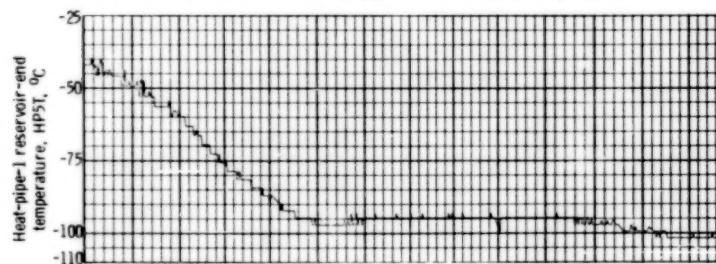
(h) Profile of VCHPS heat-pipe-2 adiabatic section temperature.



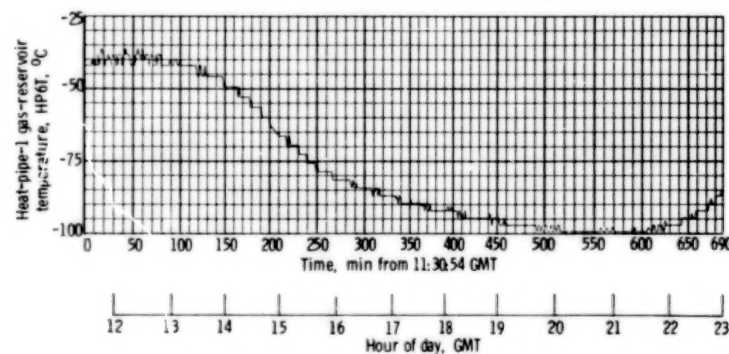
(i) Profile of VCHPS heat-pipe-3 adiabatic section temperature.



(j) Profile of VCHPS heat-pipe-1 condenser section temperature.



(k) Profile of VCHPS heat-pipe-1 reservoir-end temperature.



(l) Profile of VCHPS heat-pipe-1 gas-reservoir temperature.

Figure 14. - Concluded.

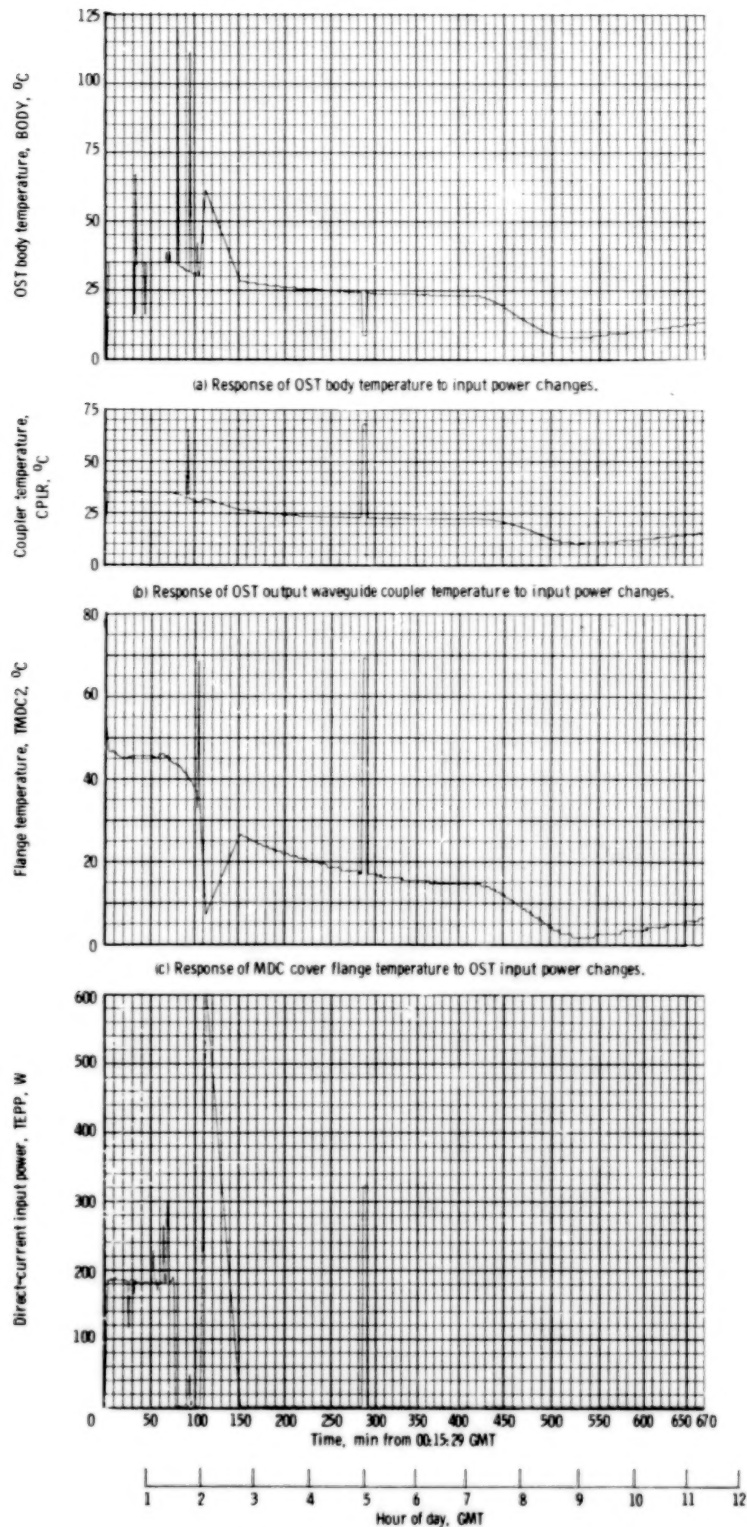
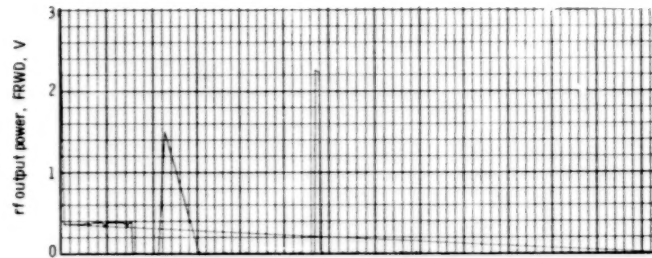
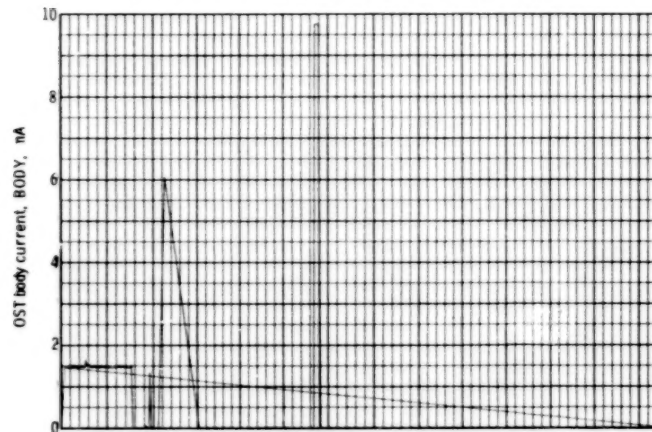


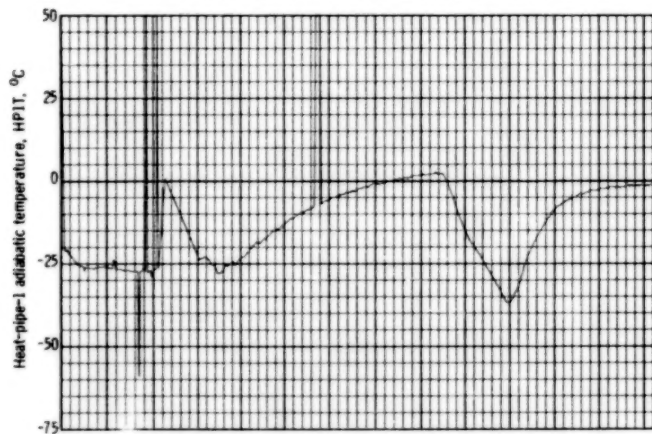
Figure 15. - Telemetry data for first half of day 82 (Mar. 23) 1977.



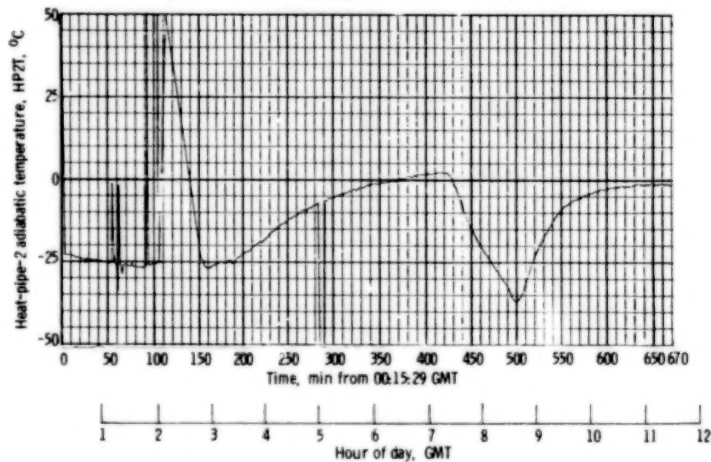
(e) Response of OST rf output power to input power changes.



(f) Response of OST body current to input power changes.

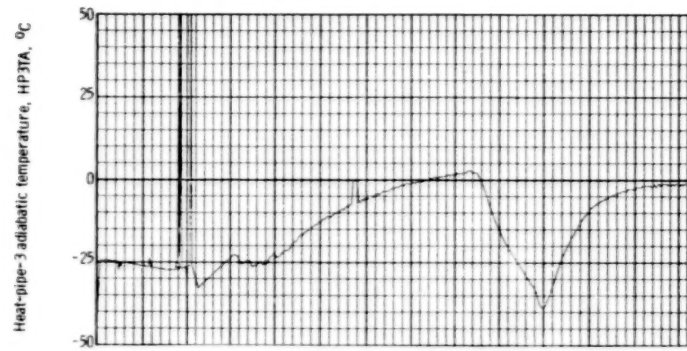


(g) Profile of VCHPS heat-pipe-1 adiabatic section temperature.

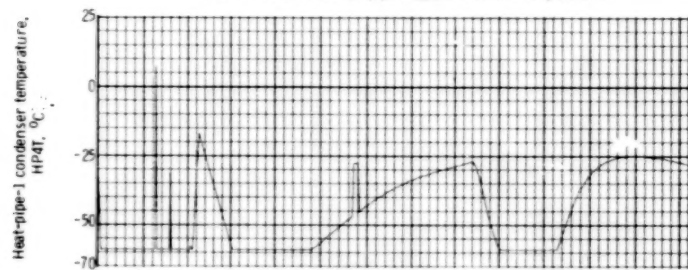


(h) Profile of VCHPS heat-pipe-2 adiabatic section temperature.

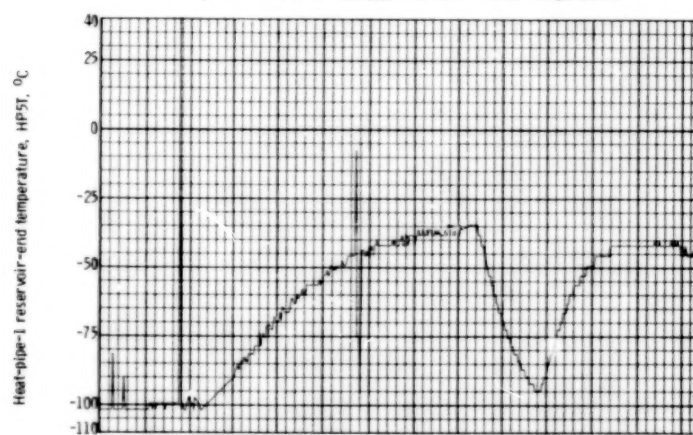
Figure 15. - Continued.



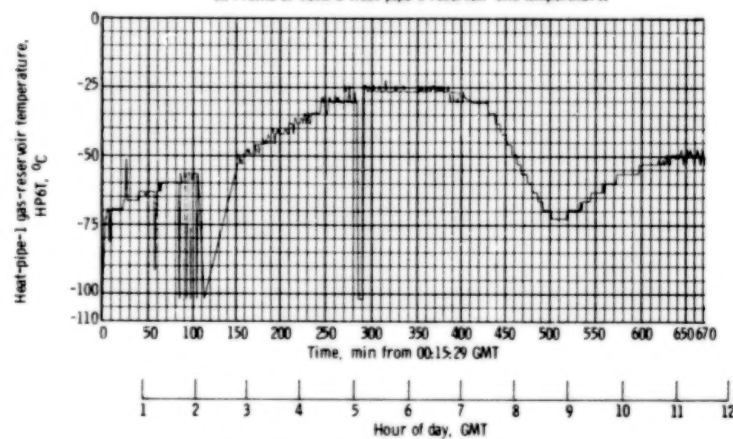
(i) Profile of VCHPS heat-pipe-3 adiabatic section temperature.



(j) Profile of VCHPS heat-pipe-1 condenser section temperature.

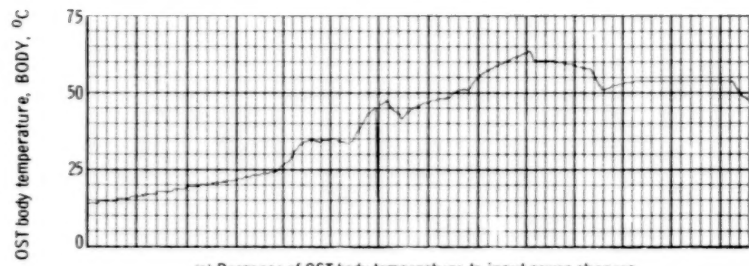


(k) Profile of VCHPS heat-pipe-1 reservoir-end temperature.

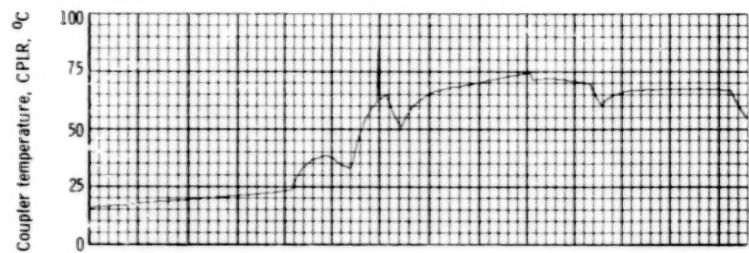


(l) Profile of VCHPS heat-pipe-1 gas-reservoir temperature.

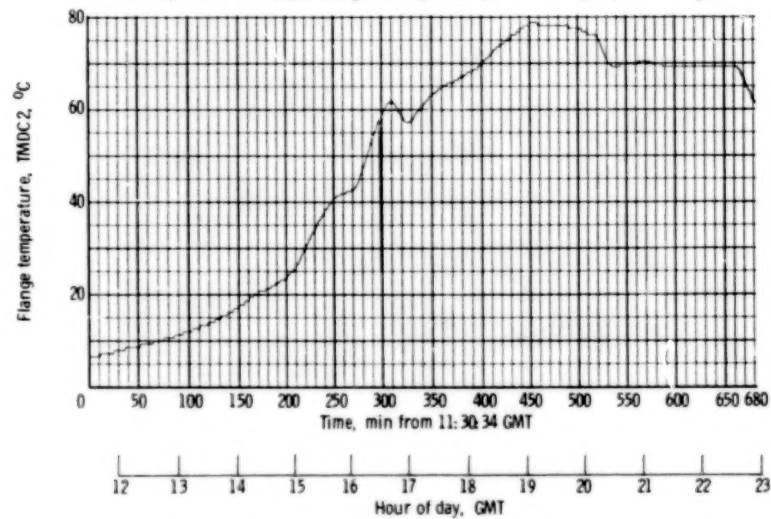
Figure 15. - Concluded.



(a) Response of OST body temperature to input power changes.

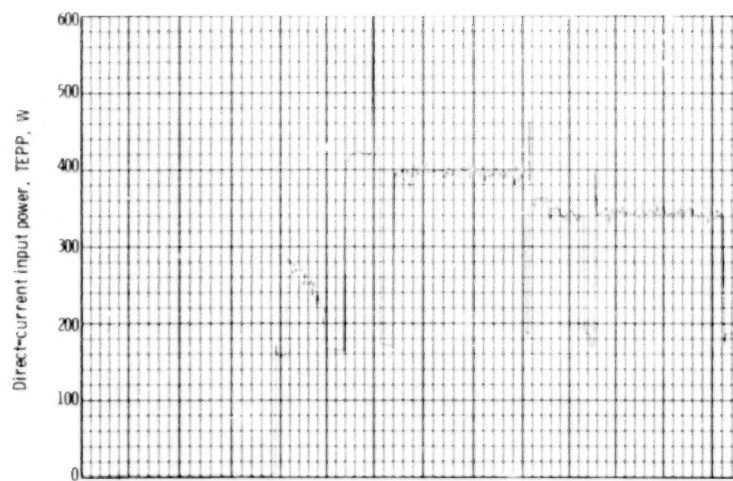


(b) Response of OST output waveguide coupler temperature to input power changes.

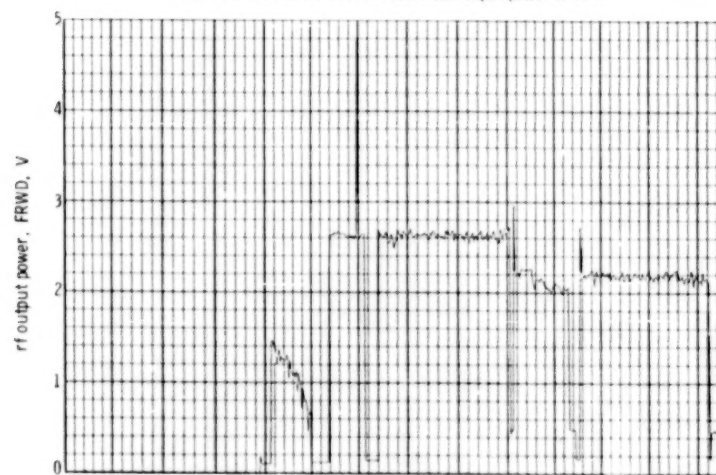


(c) Response of MDC cover flange temperature to OST input power changes.

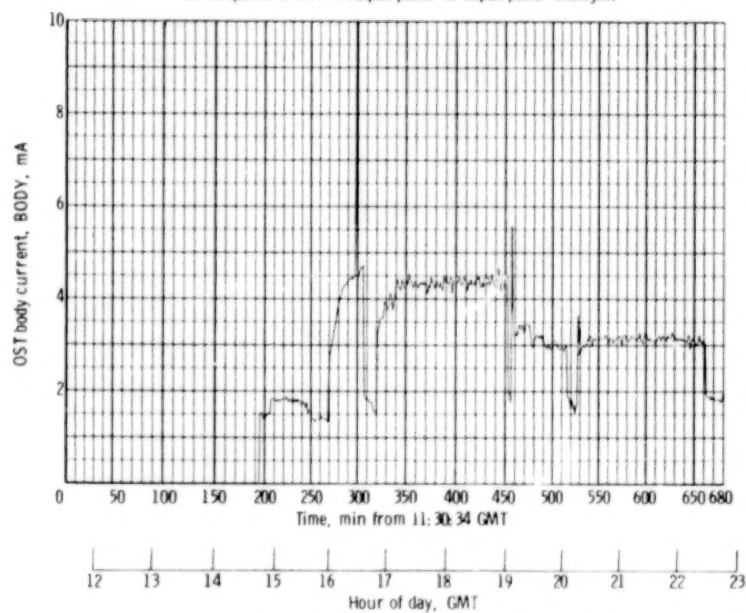
Figure 16. - Telemetry data for last half of day 82 (Mar. 23) 1977.



(d) Profile of direct-current electrical input power to OST.

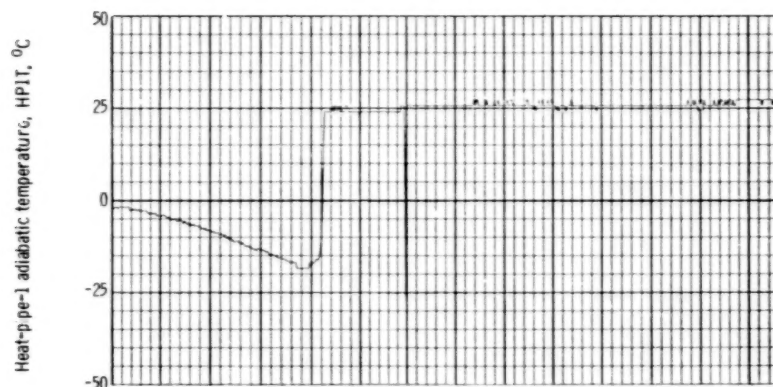


(e) Response of OST rf output power to input power changes.

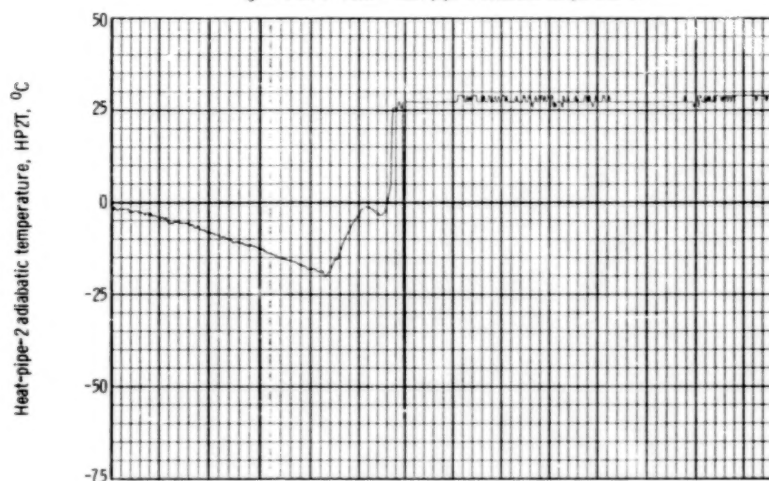


(f) Response of OST body current to input power changes.

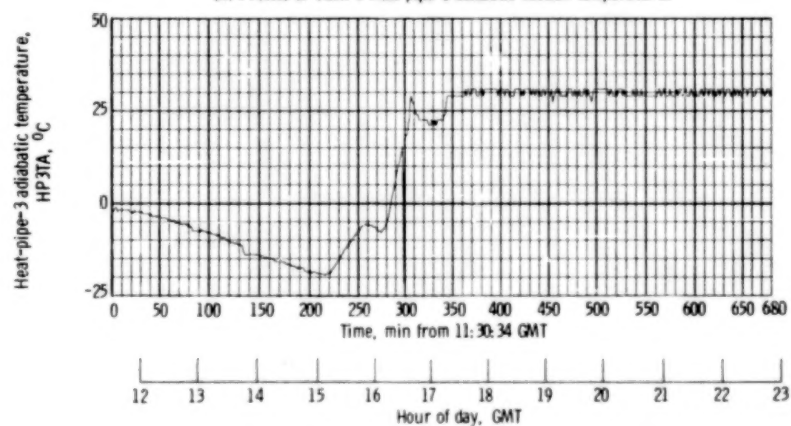
Figure 16. - Continued.



(g) Profile of VCHPS heat-pipe-1 adiabatic temperature.

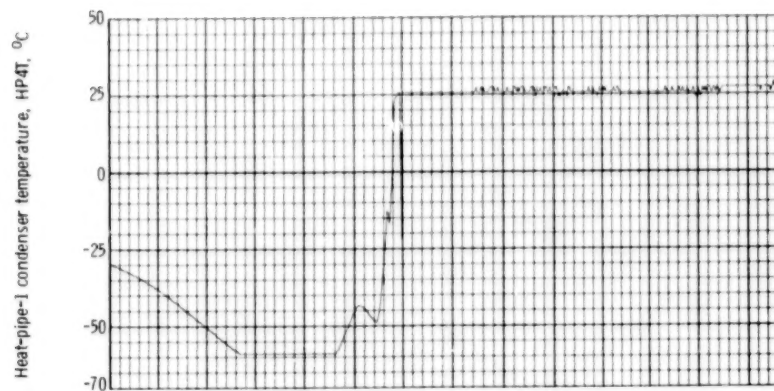


(h) Profile of VCHPS heat-pipe-2 adiabatic section temperature.

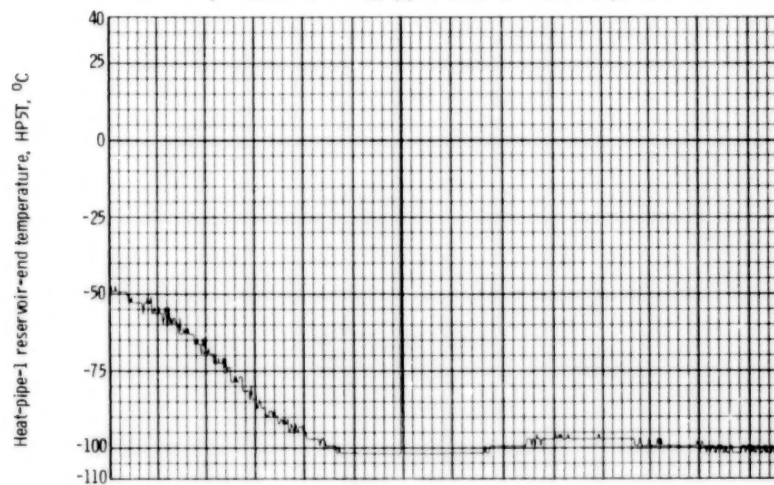


(i) Profile of VCHPS heat-pipe-3 adiabatic section temperature.

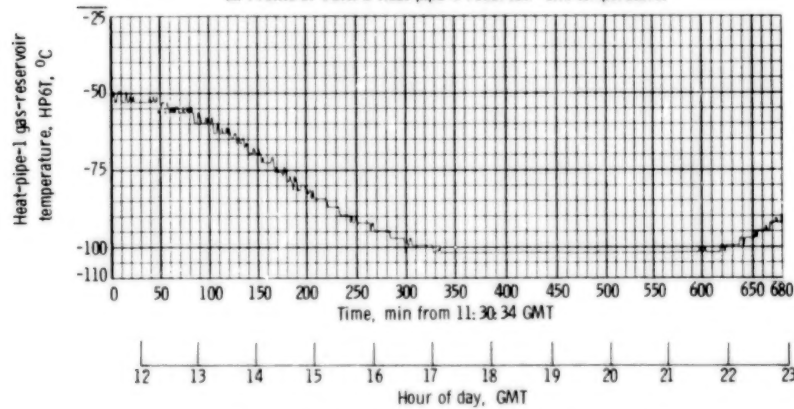
Figure 16. - Continued.



(j) Profile of VCHPS heat-pipe-1 condenser section temperature.



(k) Profile of VCHPS heat-pipe-1 reservoir-end temperature.

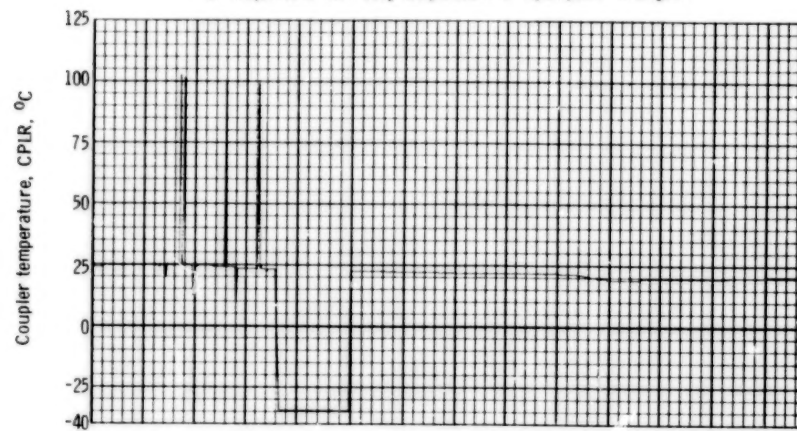


(l) Profile of VCHPS heat-pipe-1 gas-reservoir temperature.

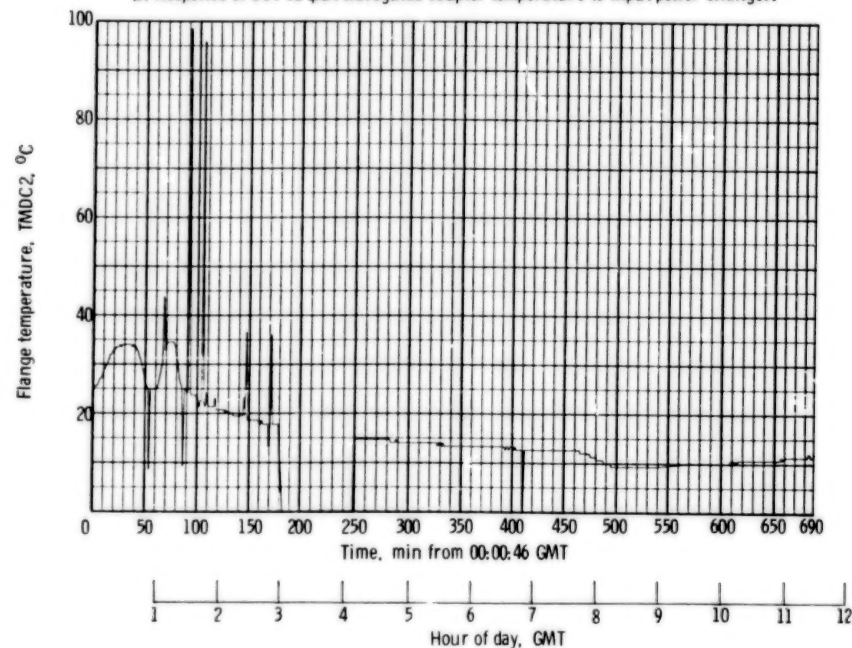
Figure 16. - Concluded.



(a) Response of OST body temperature to input power changes.



(b) Response of OST output waveguide coupler temperature to input power changes.



(c) Response of MDC cover flange temperature to OST input power changes.

Figure 17. - Telemetry data for first half of day 101 (Apr. 11) 1977.

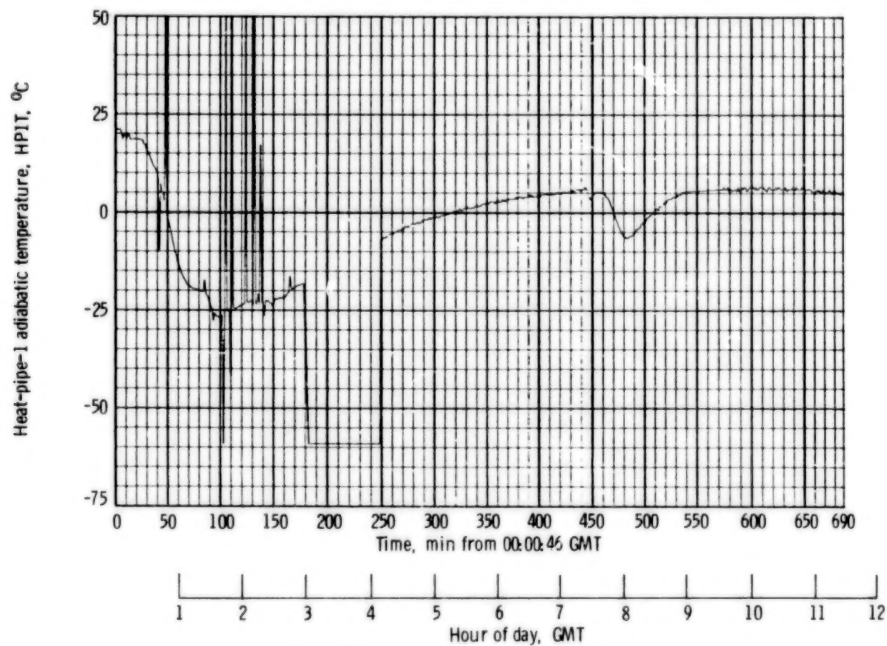
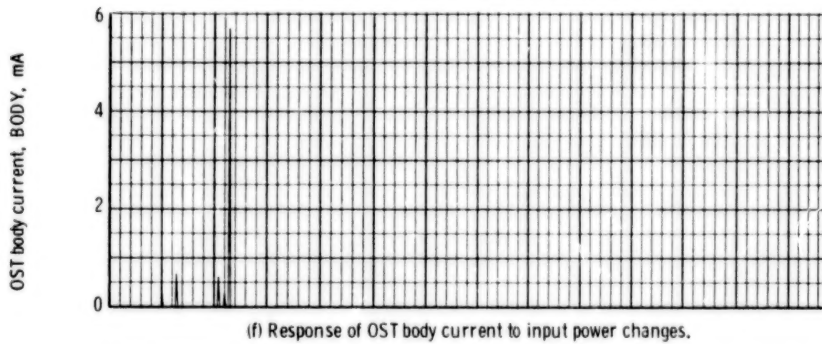
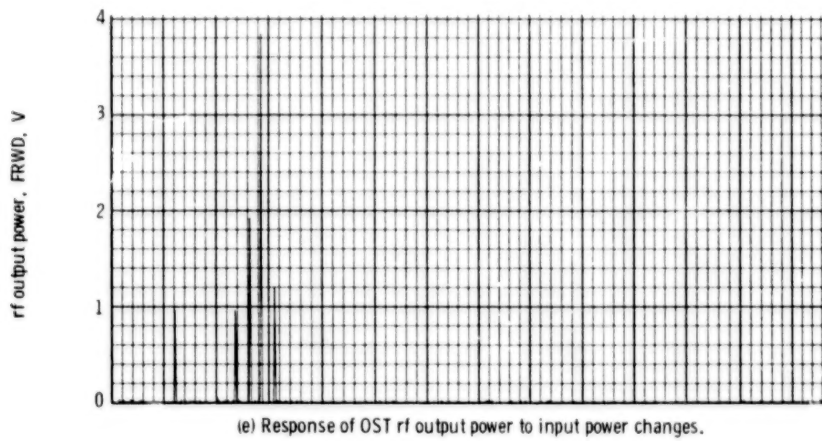
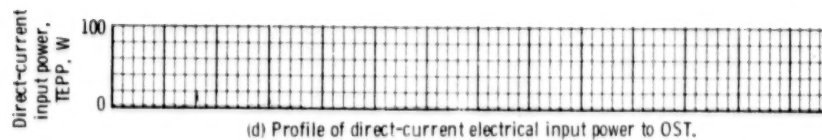
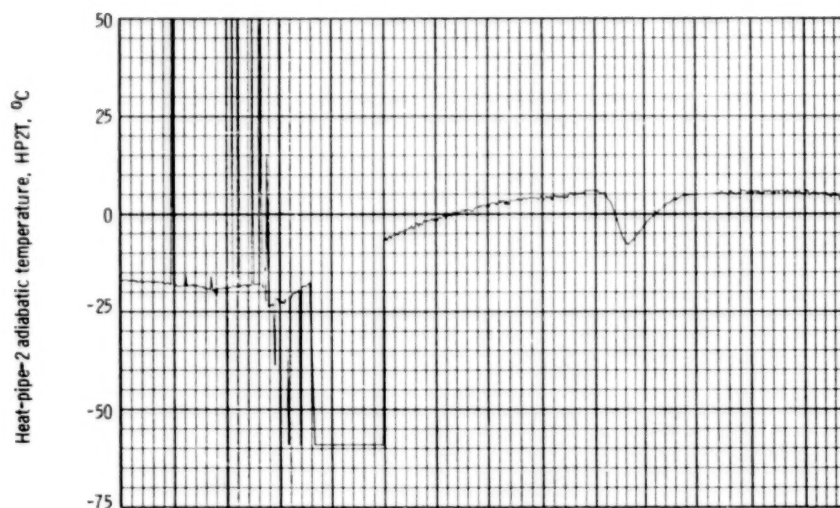
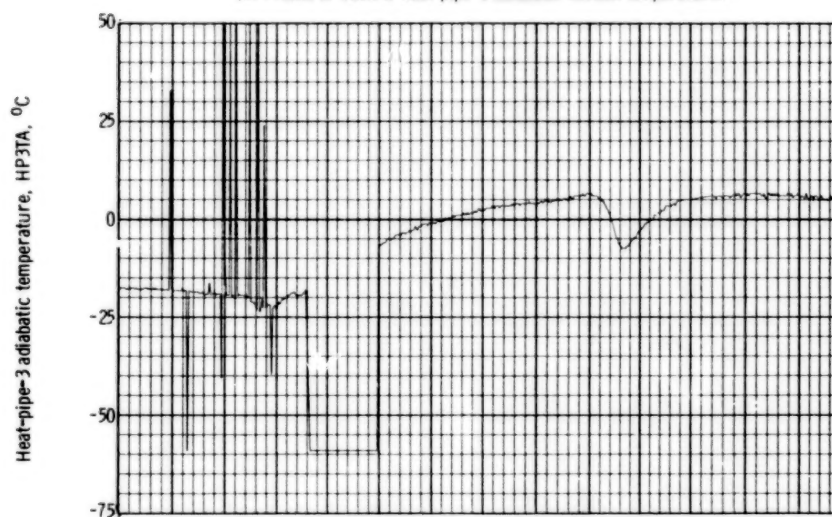


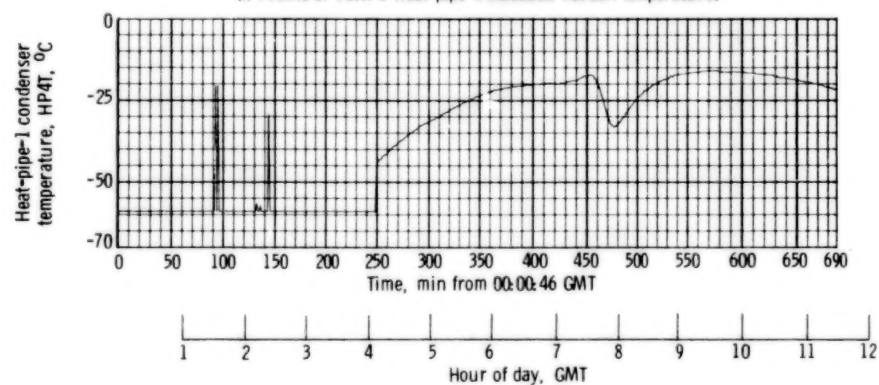
Figure 17. - Continued.



(h) Profile of VCHPS heat-pipe-2 adiabatic section temperature.

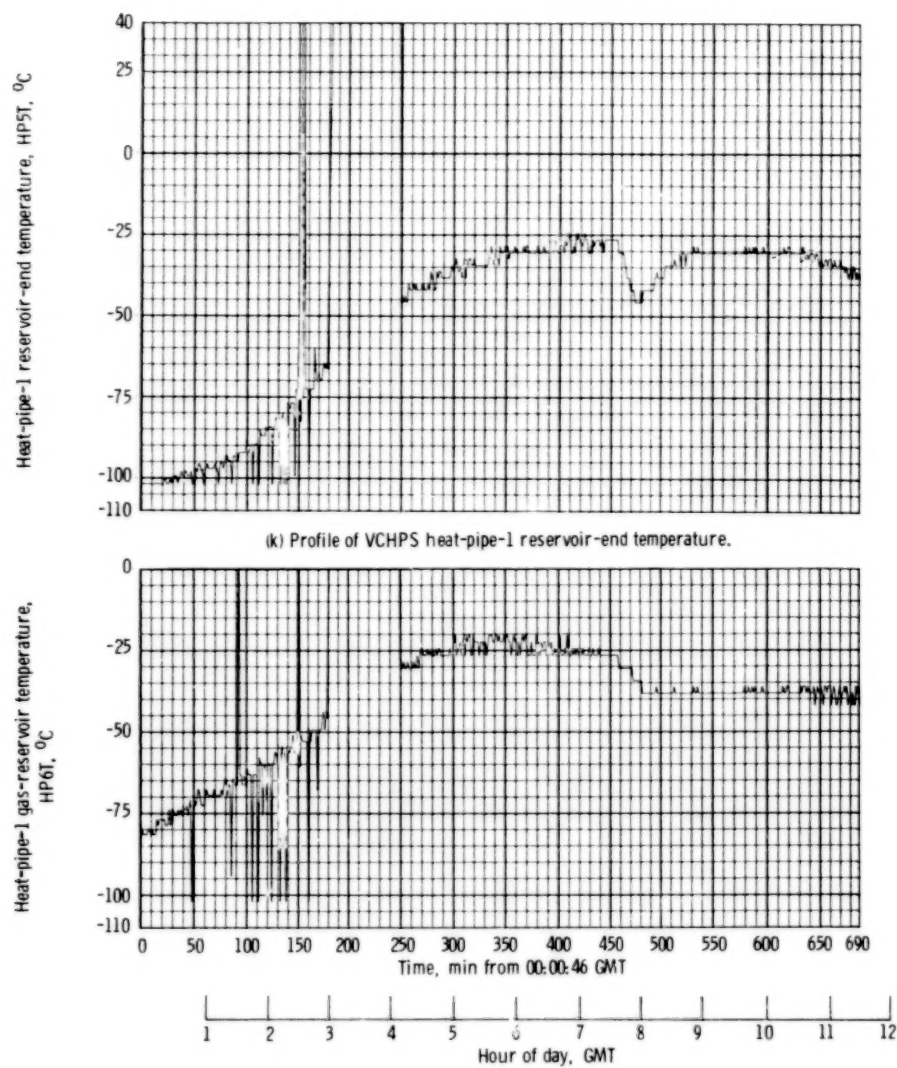


(i) Profile of VCHPS heat-pipe-3 adiabatic section temperature.



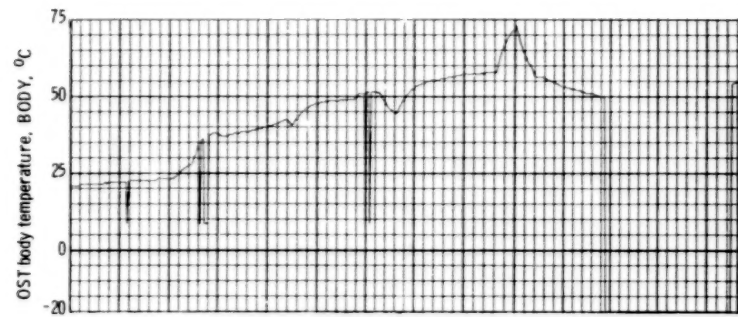
(j) Profile of VCHPS heat-pipe-1 condenser section temperature.

Figure 17. - Continued.

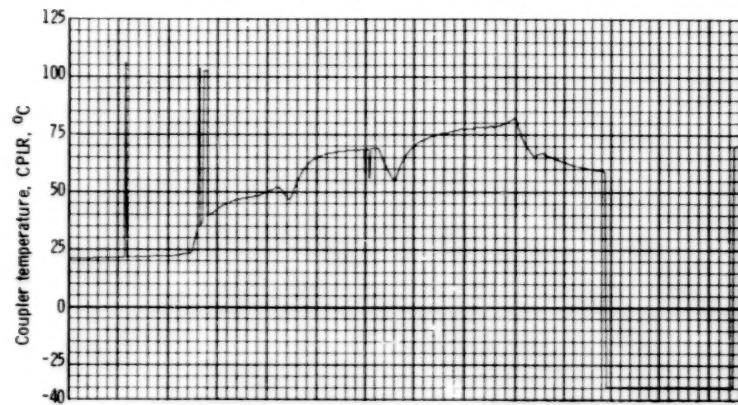


(l) Profile of VCHPS heat-pipe-1 gas-reservoir temperature.

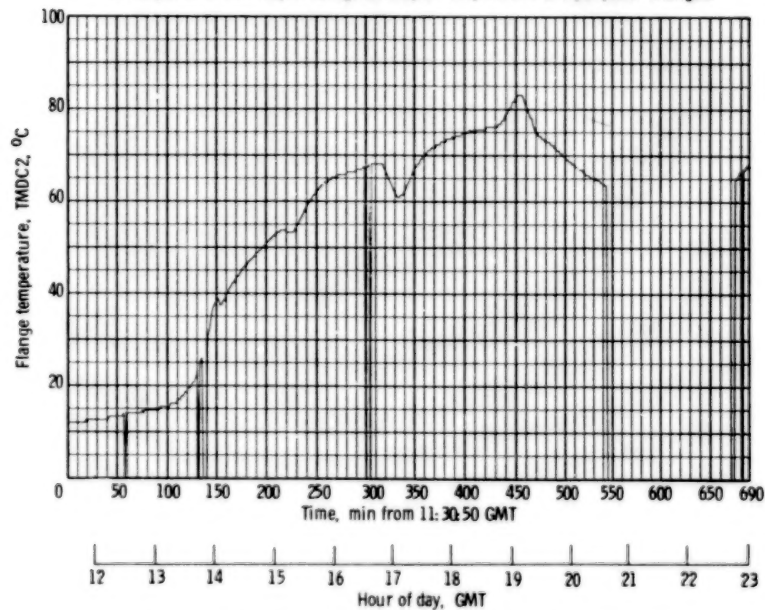
Figure 17. - Concluded.



(a) Response of OST body temperature to input power changes.

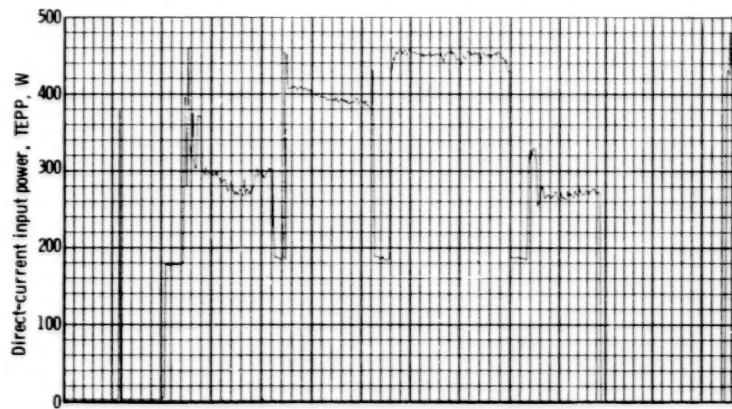


(b) Response of OST output waveguide coupler temperature to input power changes.

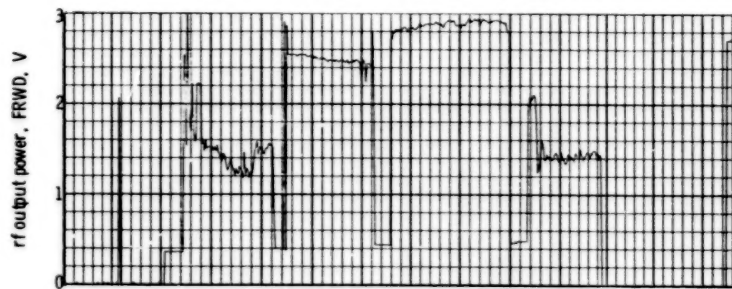


(c) Response of MDC cover flange temperature to OST input power changes.

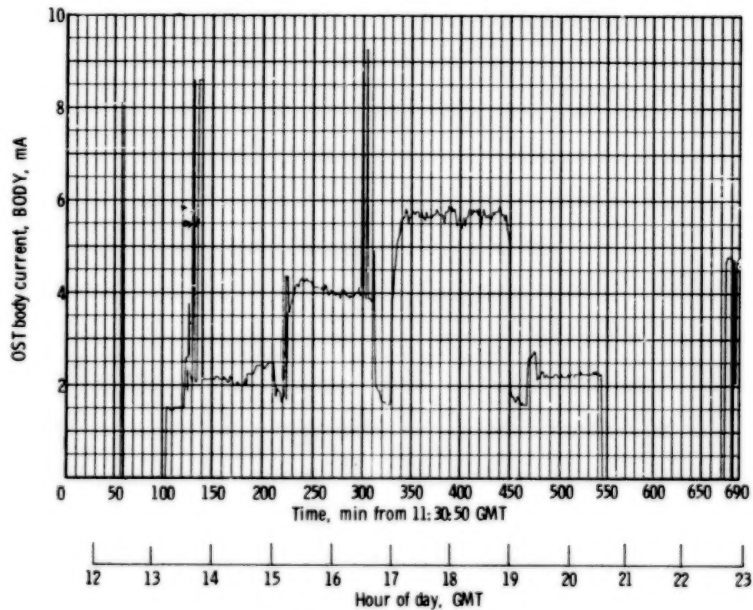
Figure 18. - Telemetry data for last half of day 101 (Apr. 11) 1977.



(d) Profile of direct-current electrical input power to OST.

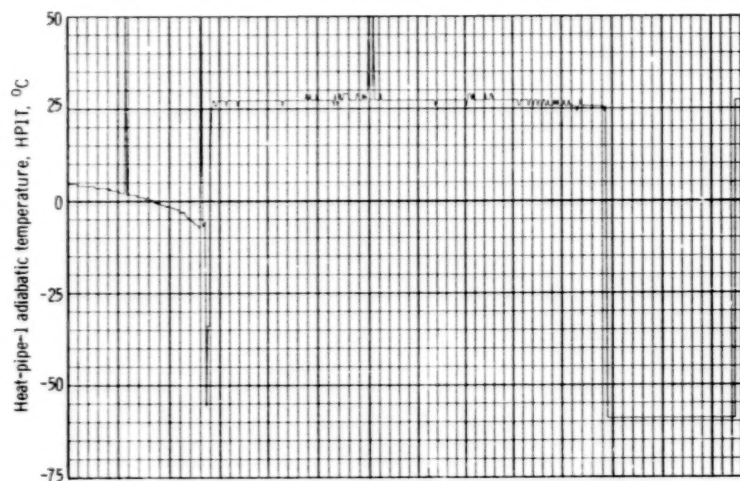


(e) Response of OST rf output power to input power changes.

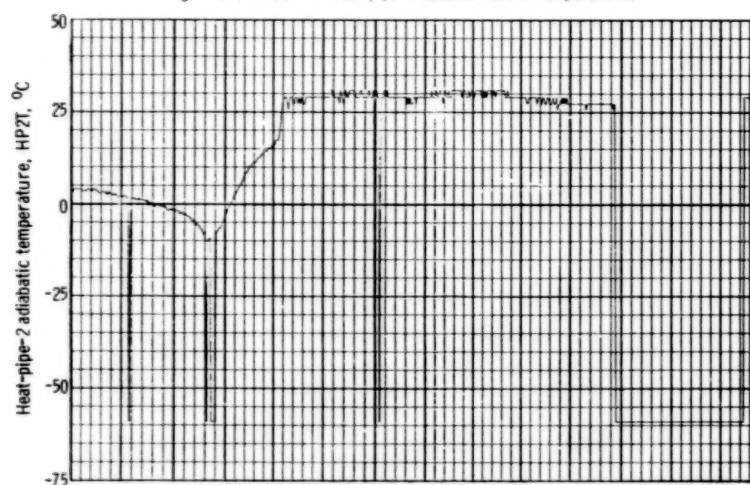


(f) Response of OST body current to input power changes.

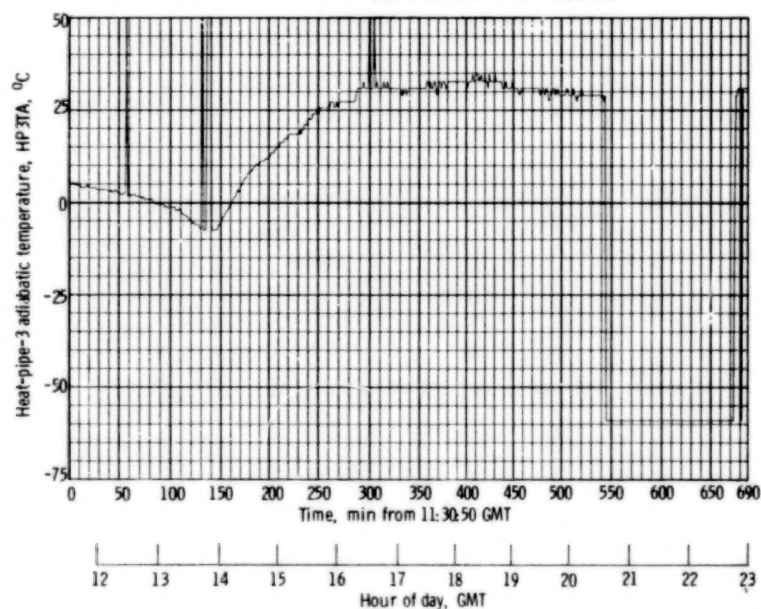
Figure 18. - Continued.



(g) Profile of VCHPS heat-pipe-1 adiabatic section temperature.

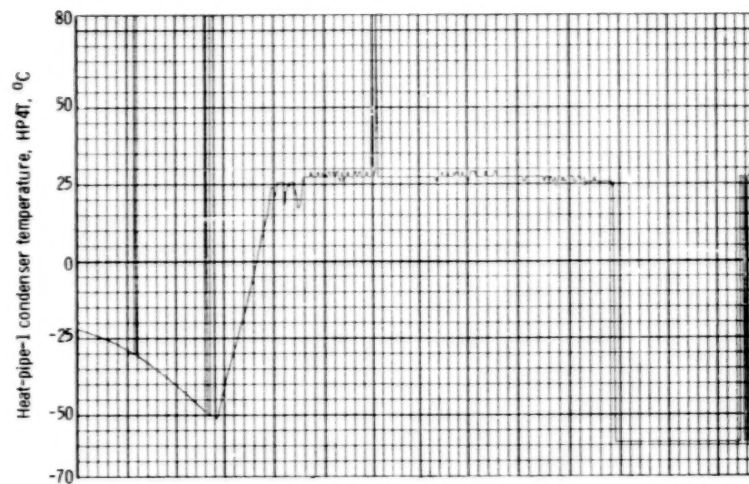


(h) Profile of VCHPS heat-pipe-2 adiabatic section temperature.

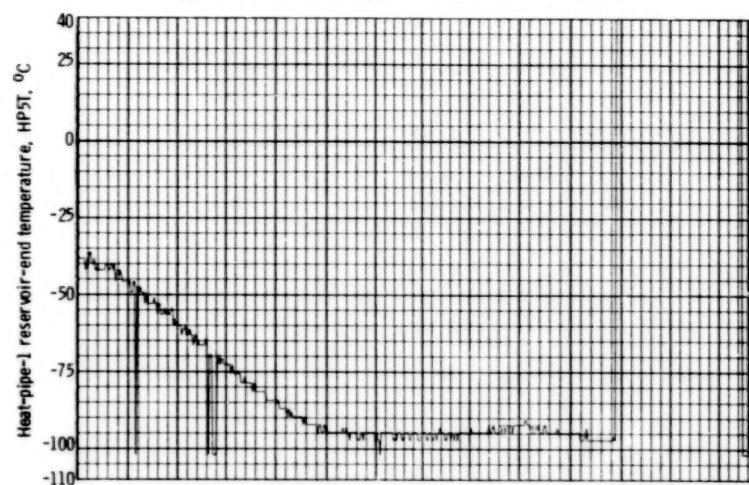


(i) Profile of VCHPS heat-pipe-3 adiabatic section temperature.

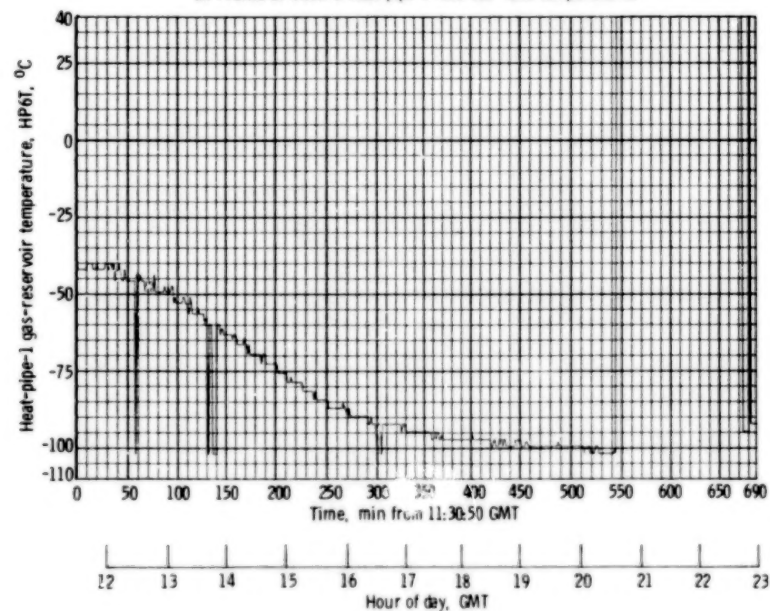
Figure 18. - Continued.



(j) Profile of VCHPS heat-pipe-1 condenser section temperature.



(k) Profile of VCHPS heat-pipe-1 reservoir-end temperature.



(l) Profile of VCHPS heat-pipe-1 gas-reservoir temperature.

Figure 18. - Concluded.

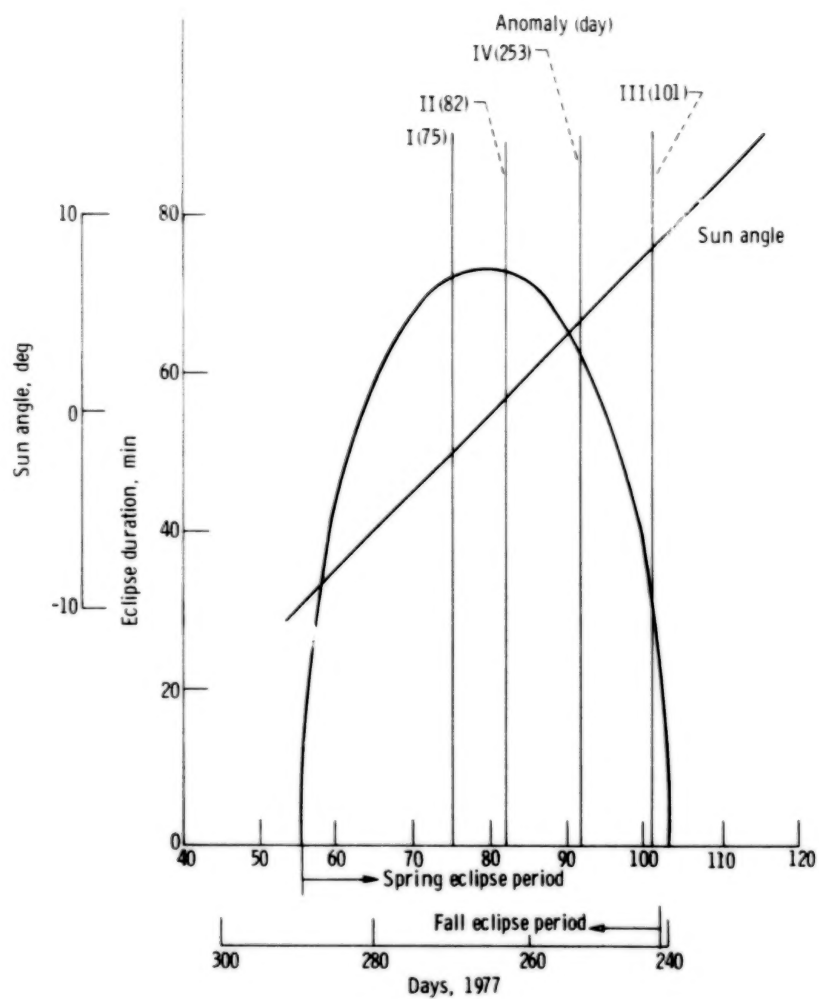


Figure 19. - CTS spacecraft Earth eclipse duration and Sun angles with respect to spacecraft orbital plane for TEP thermal-anomaly days.

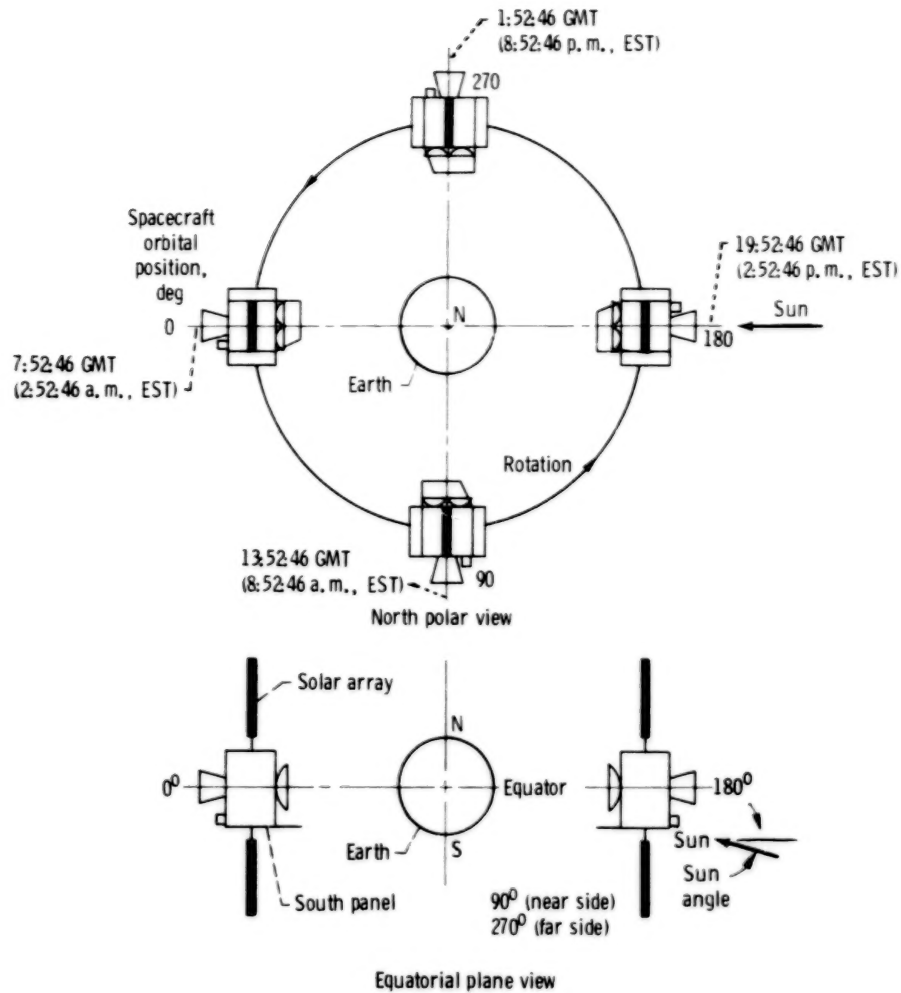


Figure 12. - CTS spacecraft orbital positions. (Orbital position times shown are for day 75.)

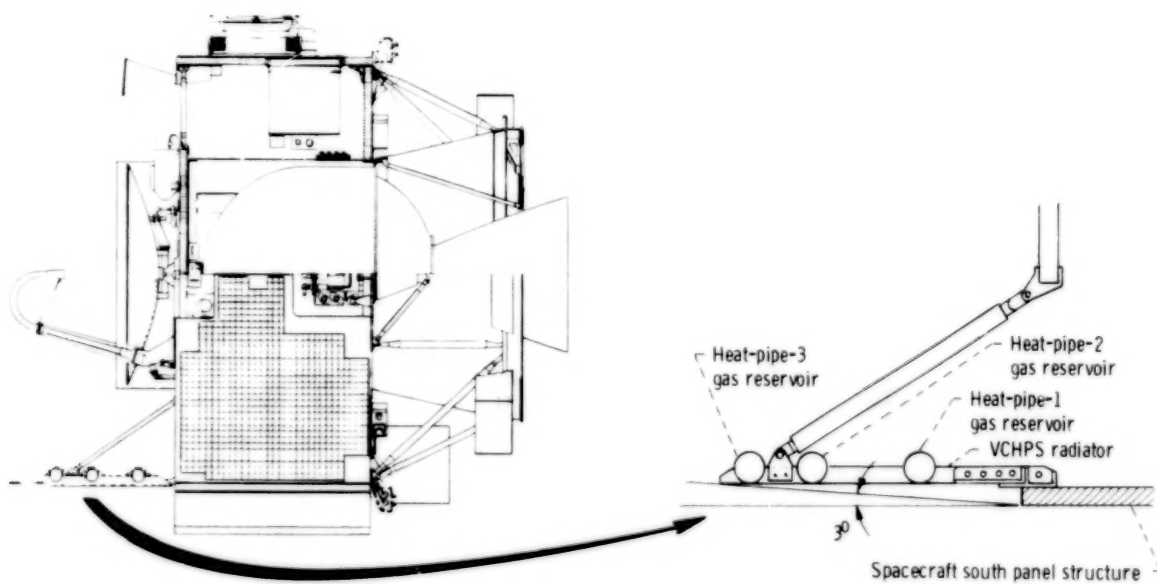


Figure 21. - West-elevation view of CTS spacecraft (half section), showing angle of VCHPS radiator shadowing by spacecraft body.

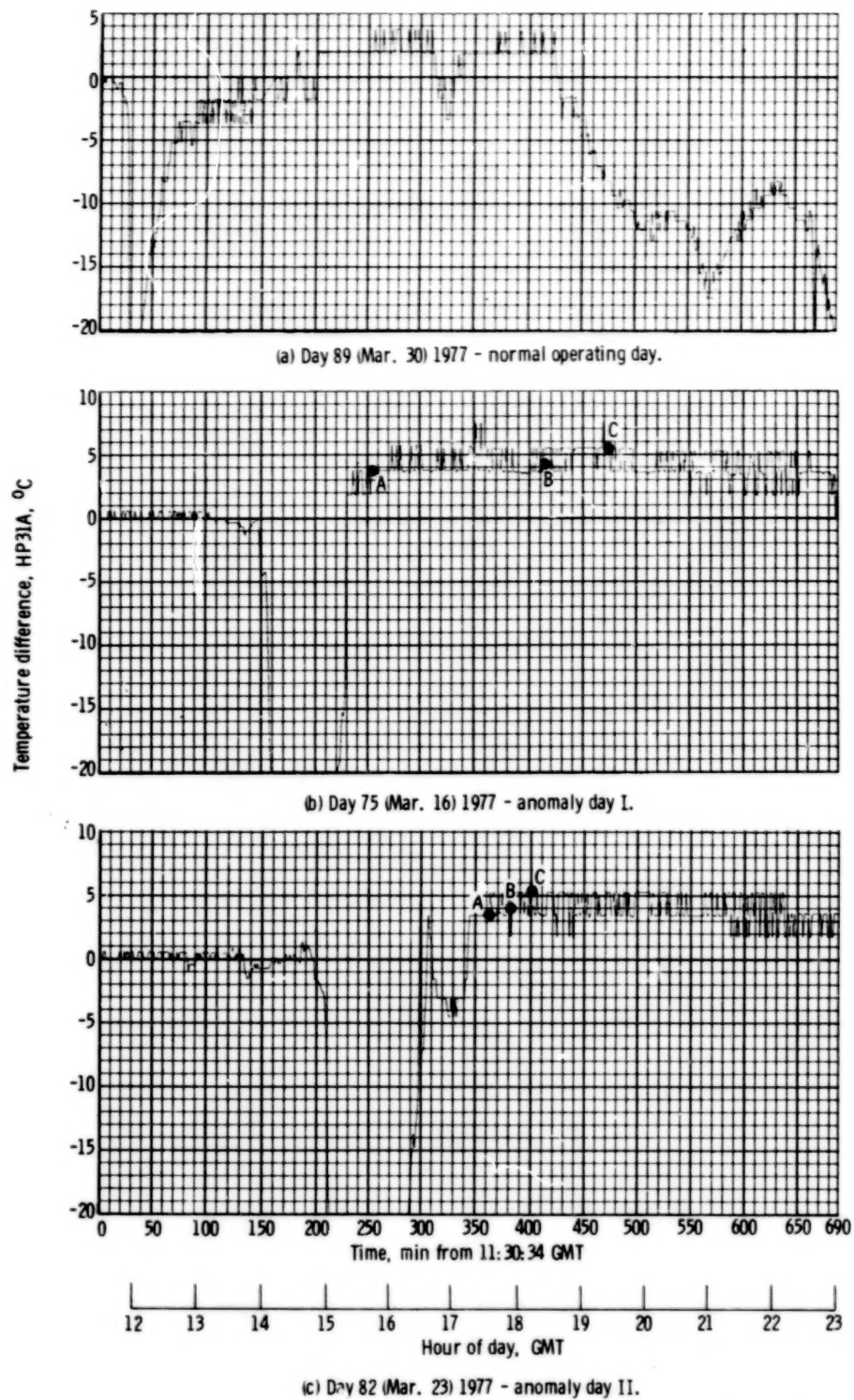
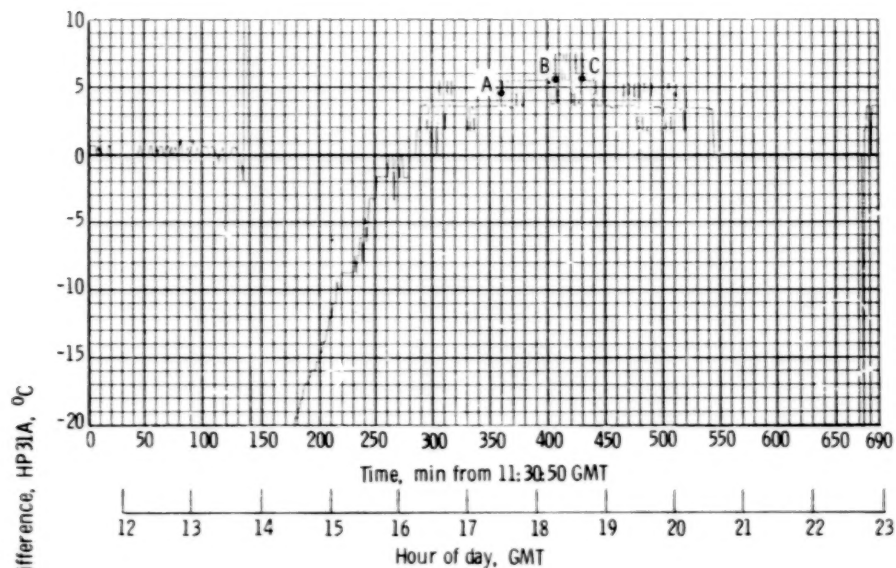
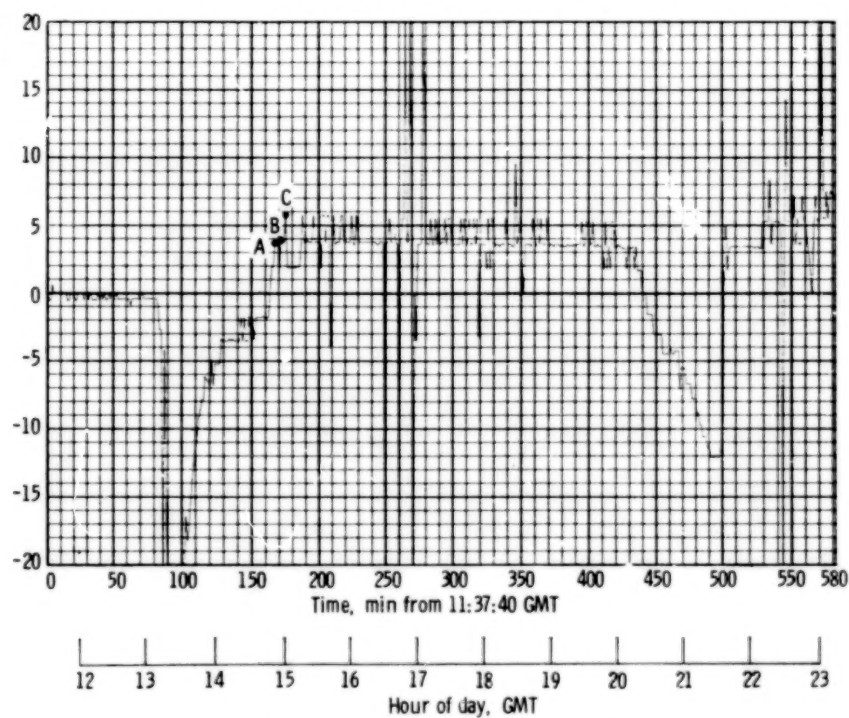


Figure 22. - Profiles of temperature differences between adiabatic sections of heat pipes 1 and 3 (HP3T - HP1T).



(d) Day 101 (Apr. 11) 1977 - anomaly day III.



(e) Day 253 (Sept. 10) 1977 - anomaly day IV.

Figure 22. - Concluded.

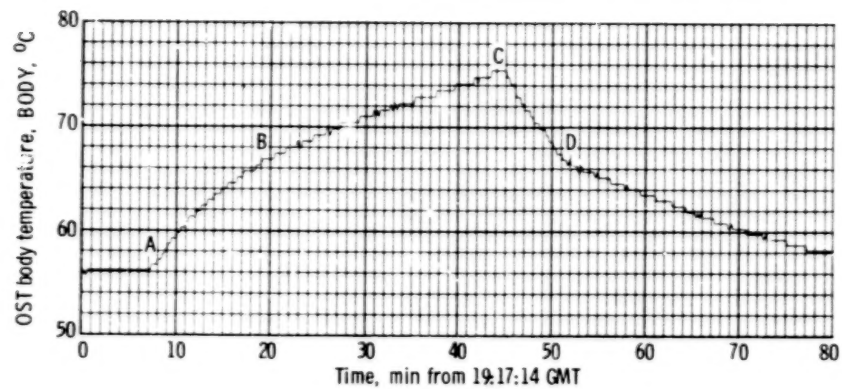


Figure 23. - Response of OST body temperature during TEP thermal-anomaly period of day 75 - telemetry data.

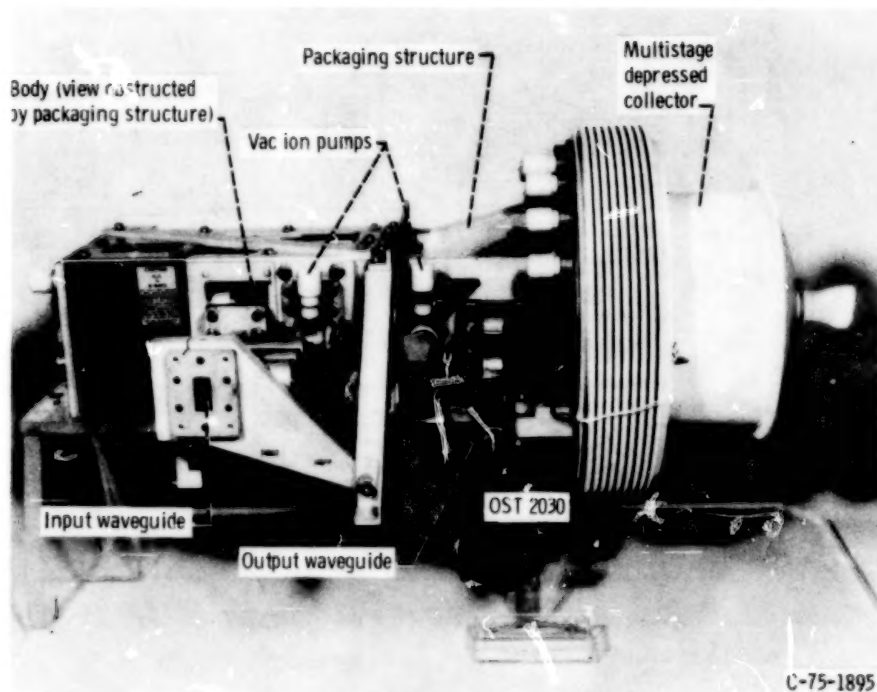


Figure 24. - CTS output stage tube.

CONTENTS

	Page	
SUMMARY	1	1/A5
INTRODUCTION	1	1/A5
TRANSMITTER EXPERIMENT PACKAGE	2	1/A6
Output Stage Tube	2	1/A6
Power-Processing System	3	1/A7
Variable-Conductance Heat-Pipe System	4	1/A8
TEP Position in Spacecraft	5	1/A9
THERMAL ANOMALIES	5	1/A9
Normal Operating Characteristics	6	1/A10
Anomaly of Day 75	8	1/A12
Anomaly of Day 82	10	1/A14
Anomaly of Day 101	11	1/B1
Anomaly of Day 253	13	1/B3
Similarities and Comparisons	13	1/B3
Reasons for Concern	14	1/B4
STUDIES AND FINDINGS	15	1/B5
Room-Ambient OST Tests	16	1/B6
Computer Studies	17	1/B7
Thermal-Vacuum OST Tests	17	1/B7
CTS In-Orbit Tests	20	1/B10
Room-Ambient VCHPS Tests	21	1/B11
Study of a TEP Anomaly in Progress	23	1/B13
Contractual Investigation	24	1/B14
Analysis of Thermal-Anomaly Transient Behavior	25	1/C1
Assessment of Anomaly Causes	29	1/C5
SUMMARY AND CONCLUSIONS	32	1/C8
APPENDIXES		
A - MAJOR-ACTIVITIES CHRONOLOGY OF CTS TEP THERMAL ANOMALY INVESTIGATING COMMITTEE	38	1/C14
B - TEMPERATURE EFFECTS ON FOCUS MAGNETS	40	1/D2
C - THERMAL OUTPUT OF OST 2022R1 AND OST 2030	45	1/D7
REFERENCES	47	1/D9

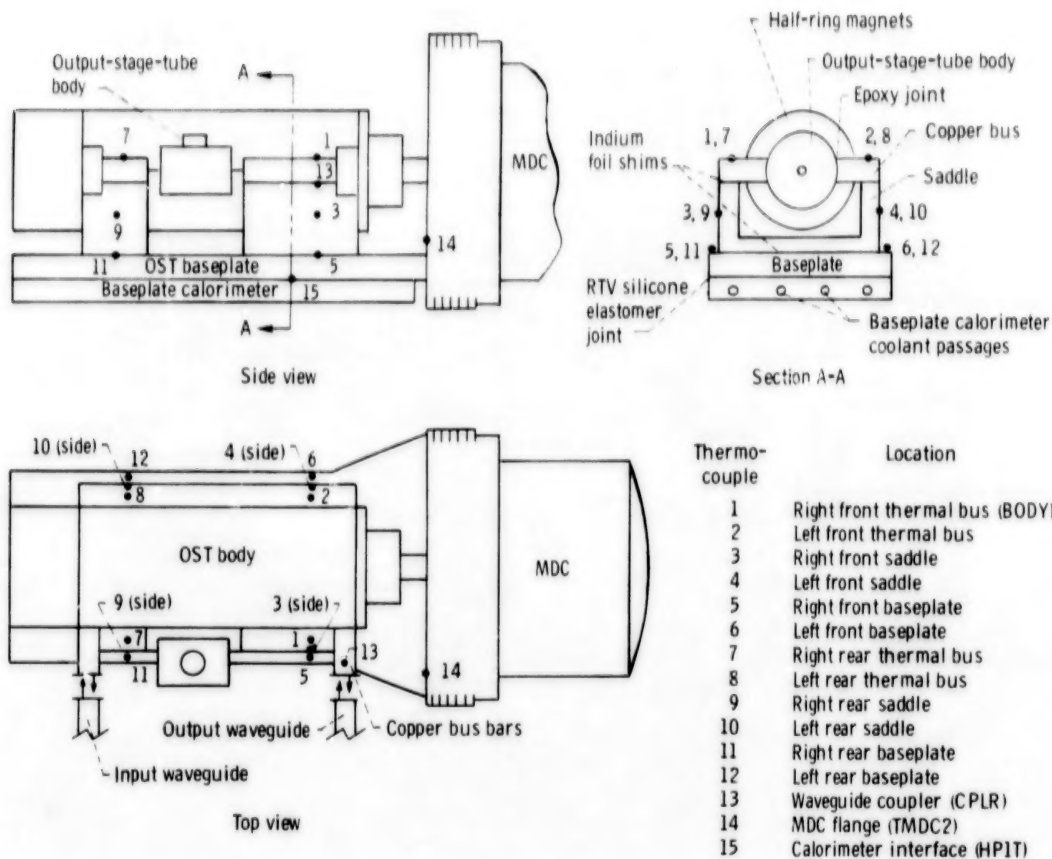


Figure 25. - Schematic of thermal instrumentation on CTS OST 2030 (no scale intended).

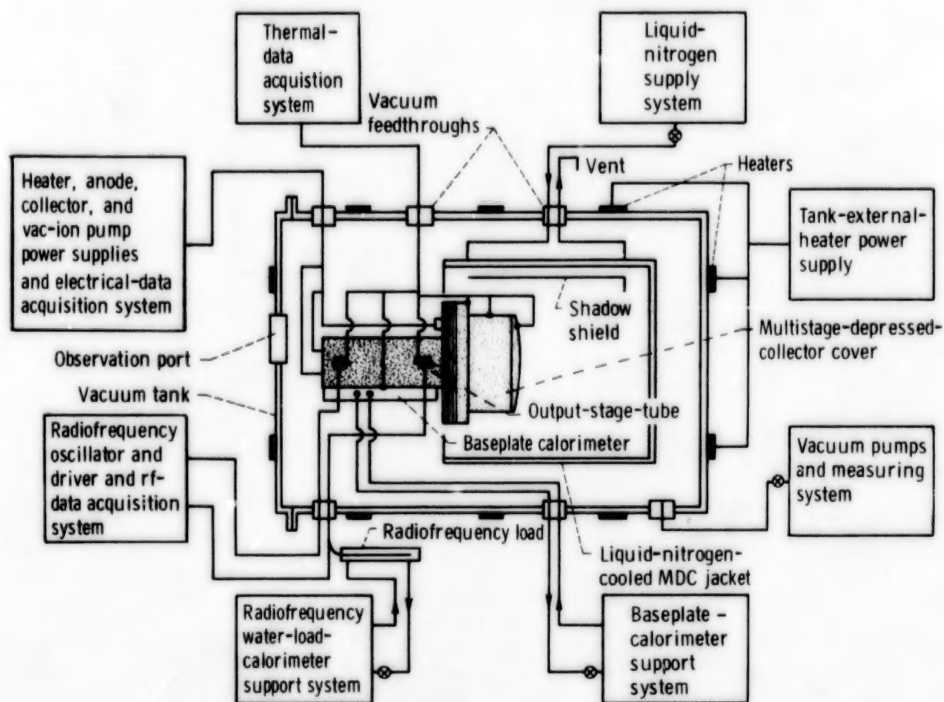


Figure 26. - Schematic of CTS OST thermal-vacuum test facility.

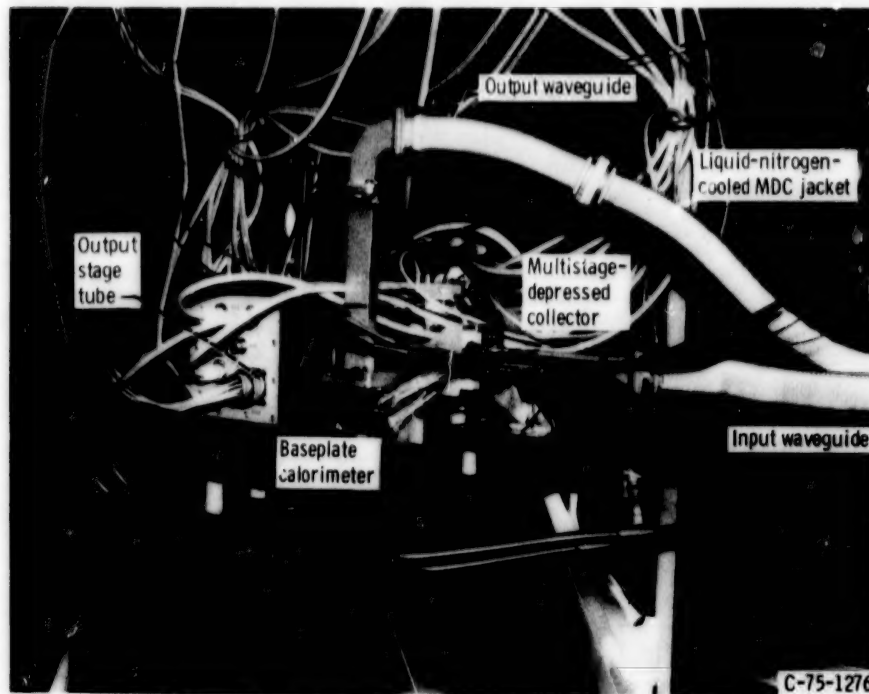


Figure 27. - CTS output stage tube mounted in thermal-vacuum test facility, showing liquid-nitrogen-cooled, space-simulating jacket of multistage depressed collector.

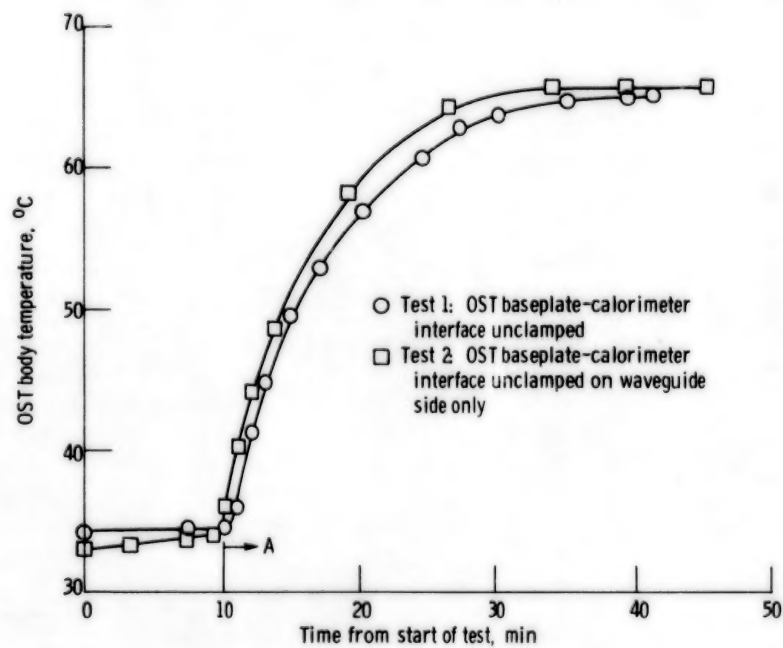


Figure 28. - Response of OST body temperature to thermal interface compromises. Operating conditions from point A: saturated rf output power, 200 W (nominal); center-band frequency, 12.080 GHz; baseplate temperature, 35° C (nominal).

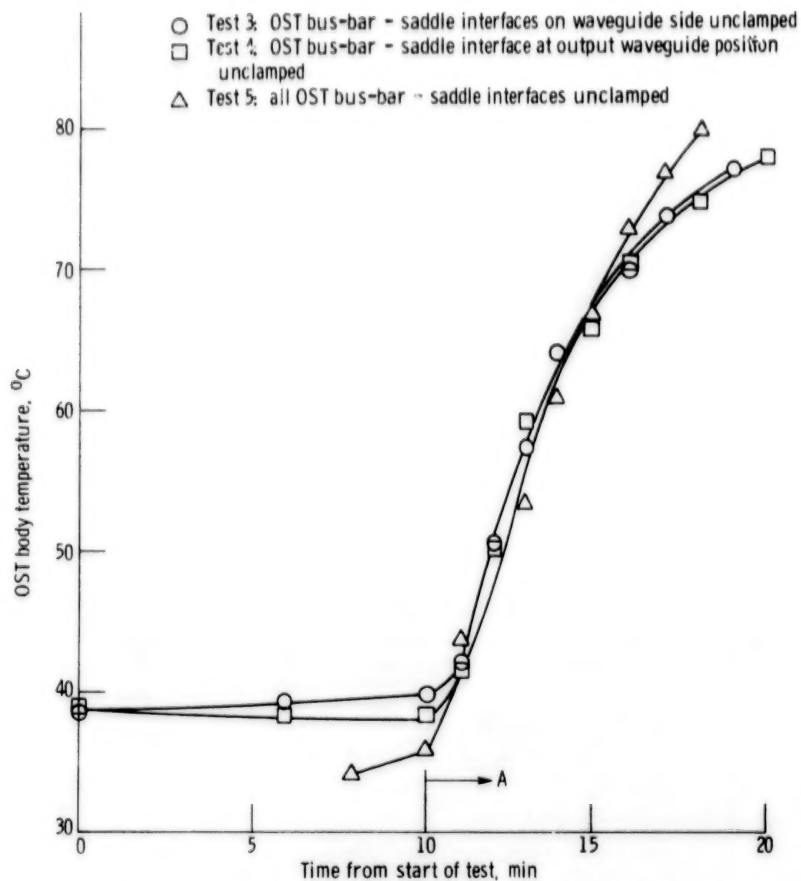


Figure 29. - Response of OST body temperature to bus-bar - saddle interface compromises. Operating conditions from point A: saturated rf output power, 200 W (nominal); center-band frequency, 12.080 GHz; baseplate temperature, 35° C (nominal).

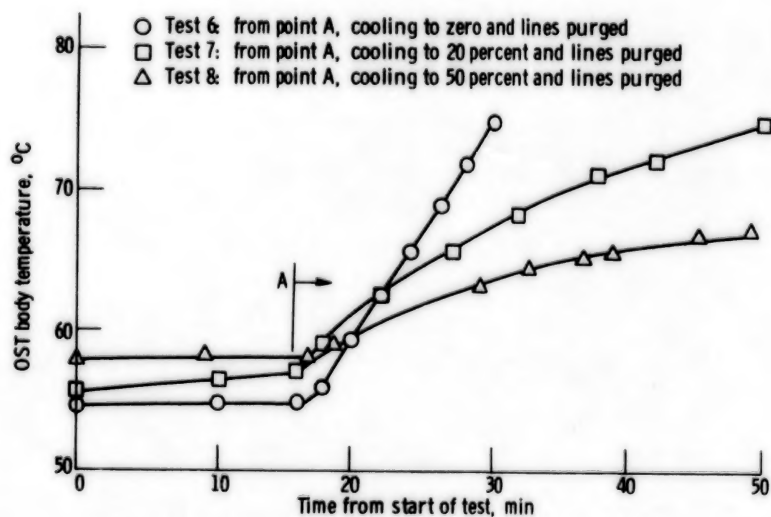


Figure 30. - Response of OST body temperature to changes in cooling. Operating conditions from point A: saturated rf output power, 200 W (nominal); center-band frequency, 12.080 GHz; equilibrium baseplate temperature to point A.

Parameter	Test		Anomaly day			
	8	7	75	82	101	253
	Approximate initial temperature change, deg C/min					
BODY	0.48	1.23	1.36	0.46	1.52	0.41
CPLR	.13	.21	.19	.10	.24	.11
TMDC2	.27	.43	.43	.20	.45	.23

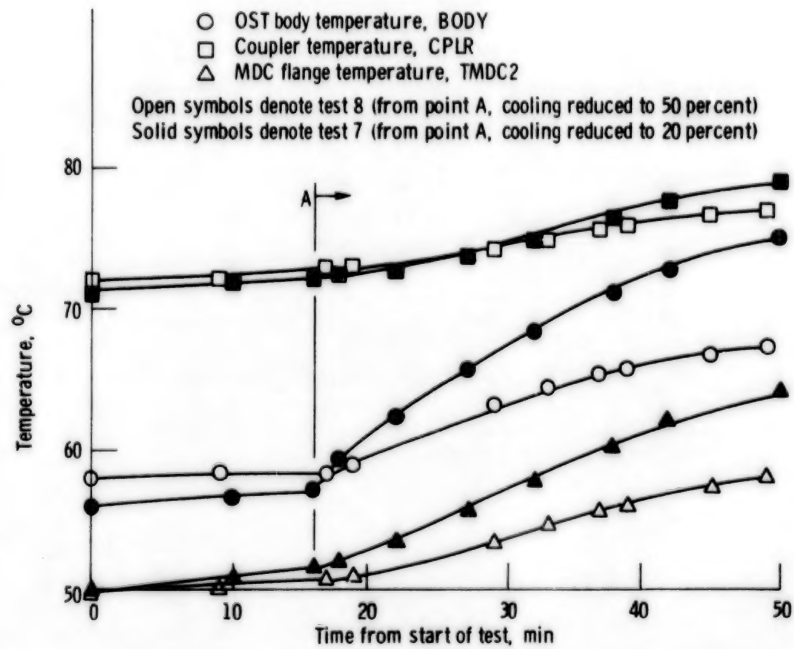


Figure 31. - Response of OST body, waveguide coupler, and MDC flange temperature to cooling reductions. Operating conditions from point A: thermal equilibrium at saturated rf output power, 200 W (nominal); center-band frequency, 12.080 GHz; baseplate temperature, 56° C (nominal).

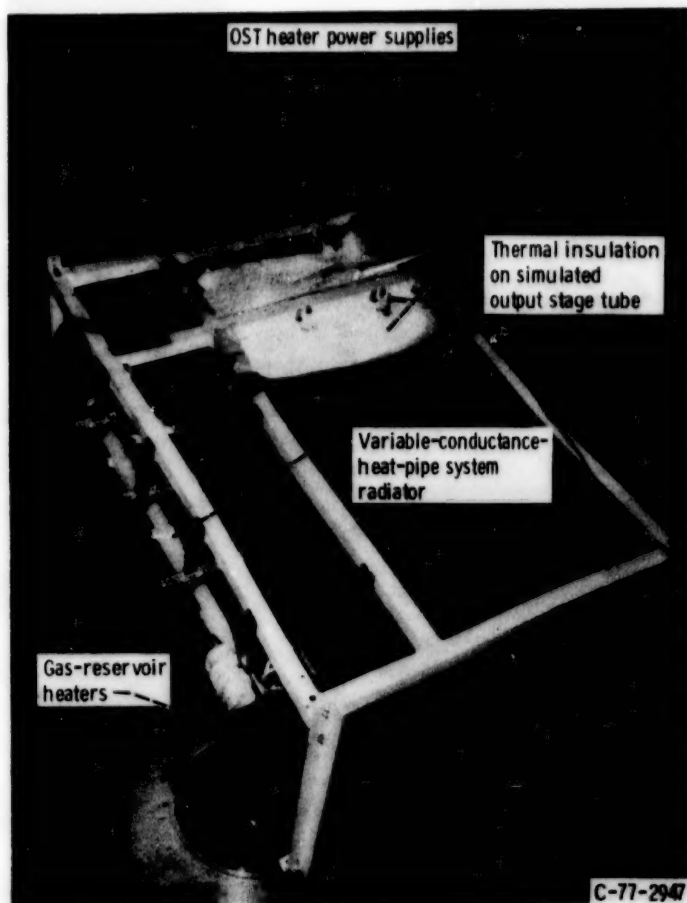


Figure 32. - Facility used in variable-conductance-heat-pipe system tests.

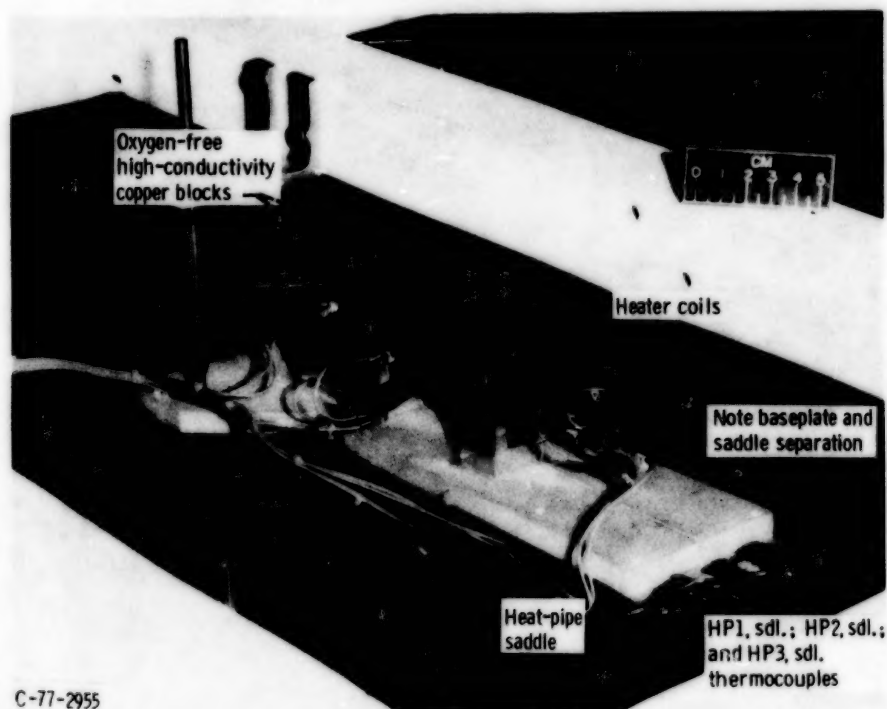


Figure 33. - Thermal model of output stage tube, showing heat-pipe instrumentation details.

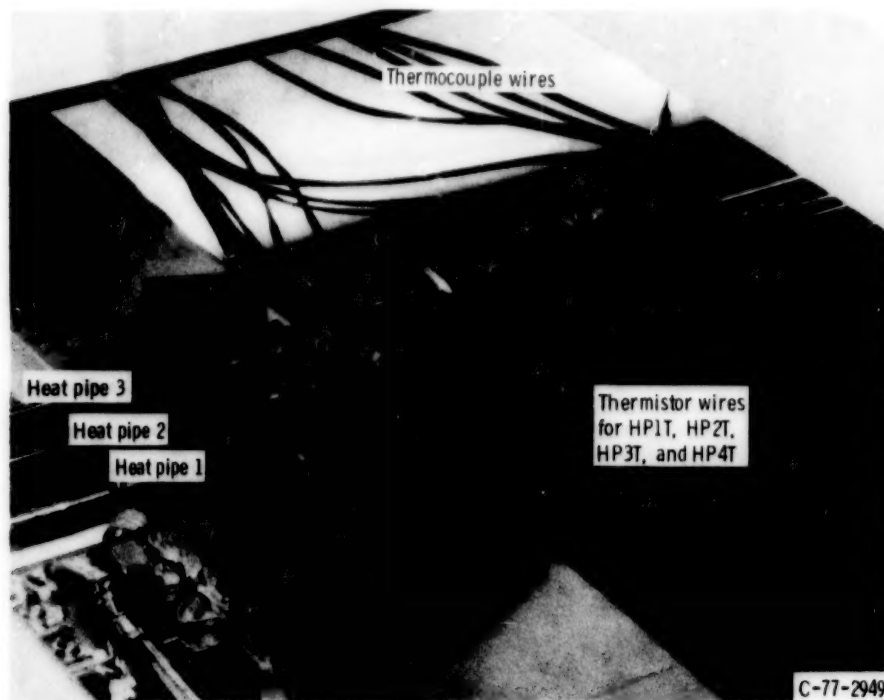


Figure 34. - Adiabatic section of variable-conductance-heat-pipe system, showing general instrumentation locations.

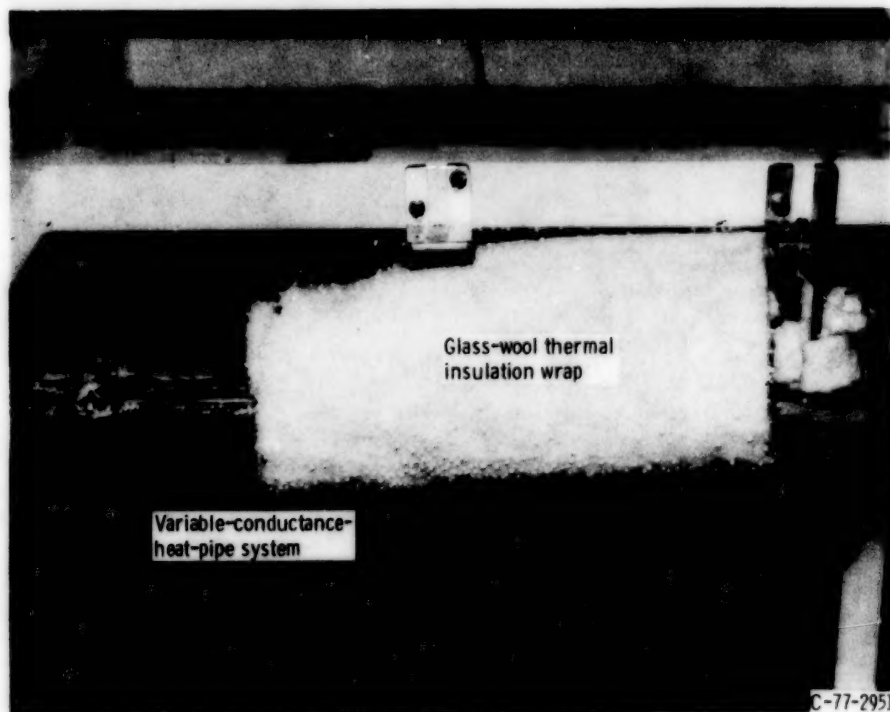
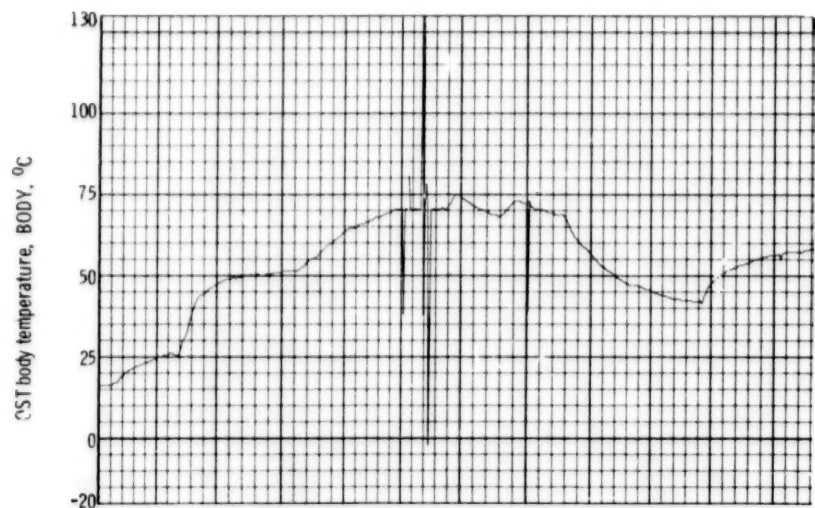
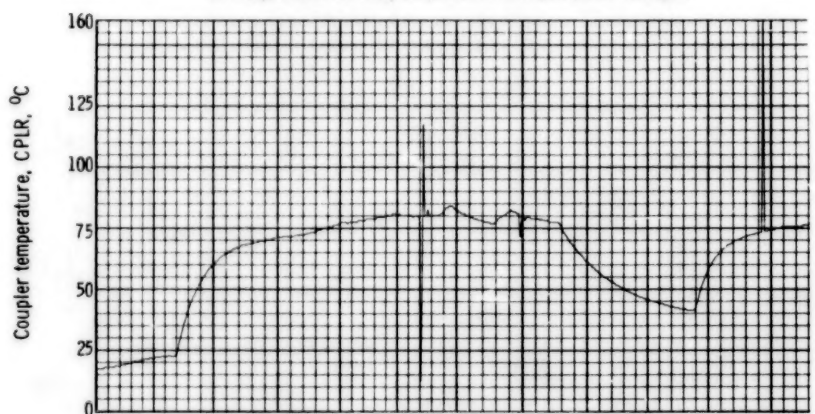


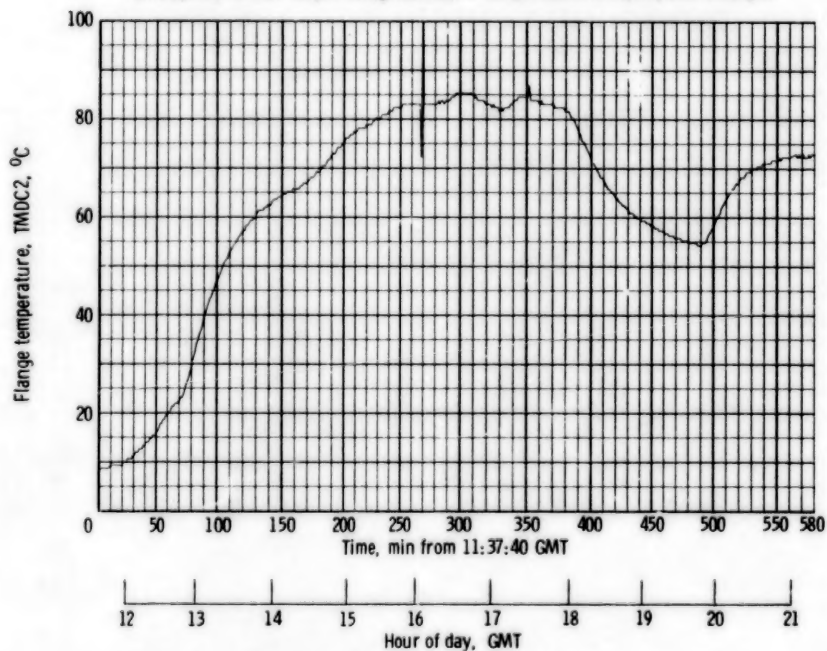
Figure 35. - Thermal insulation on simulated output stage tube.



(a) Response of OST body temperature to input power changes.

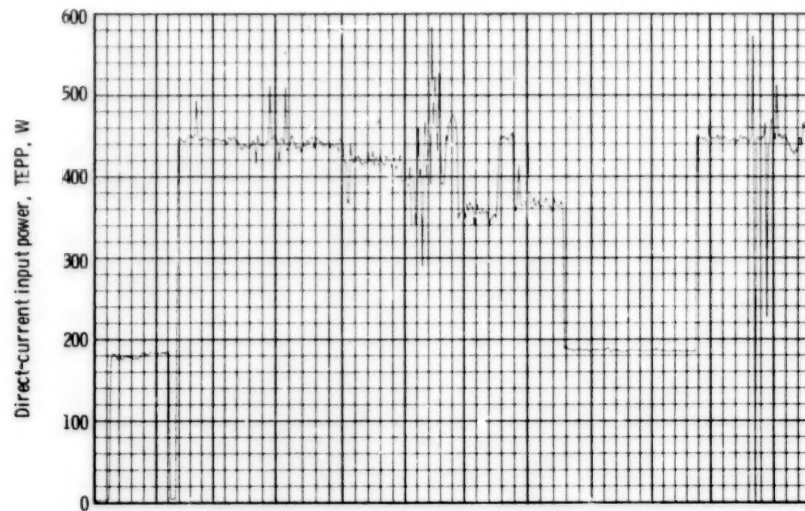


(b) Response of OST output waveguide coupler temperature to input power changes.

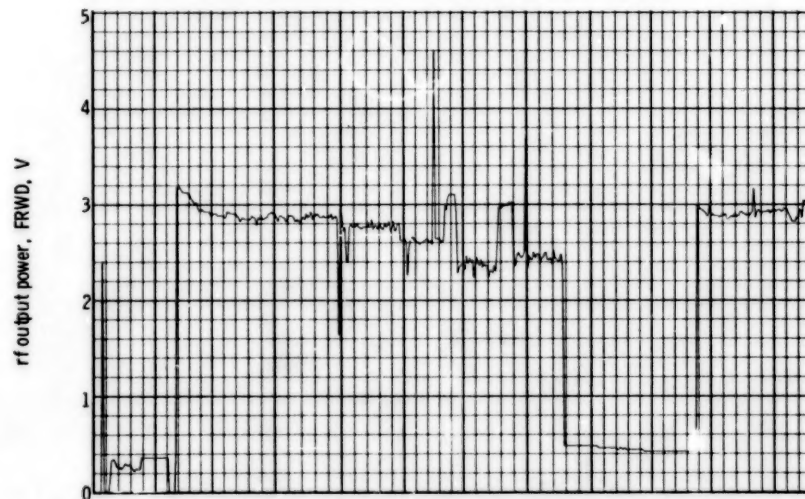


(c) Response of MDC cover flange temperature to OST input power changes.

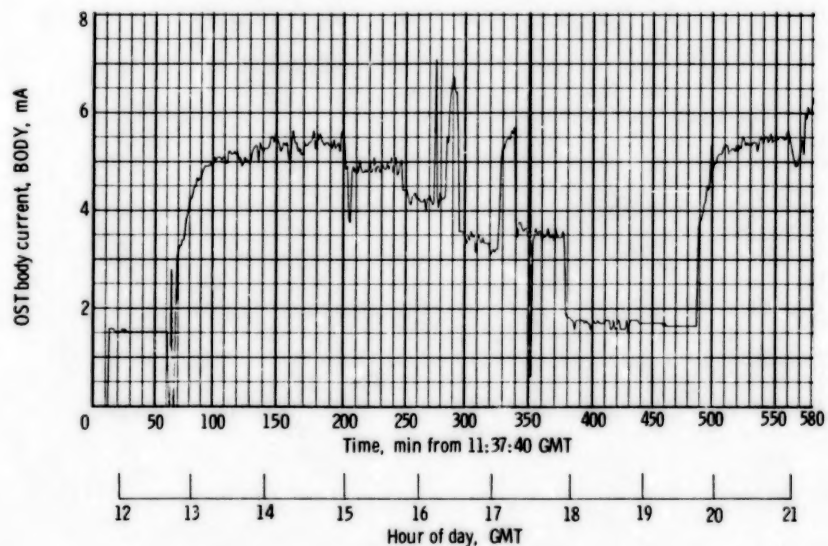
Figure 36. - Telemetry data for last half of day 253 (Sept. 10) 1977.



(d) Profile of direct-current electrical input power to OST.

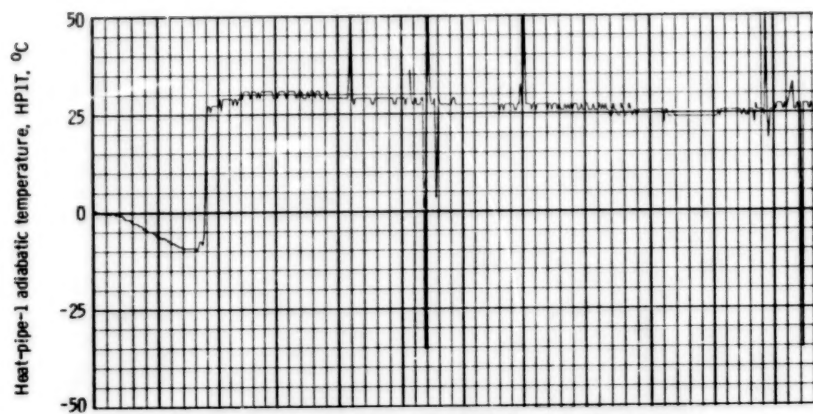


(e) Response of OST rf output power to input power changes.

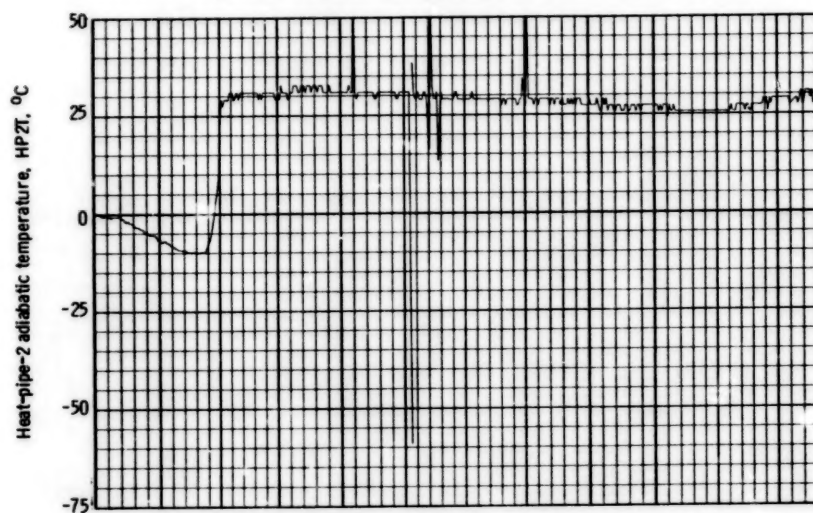


(f) Response of OST body current to input power changes.

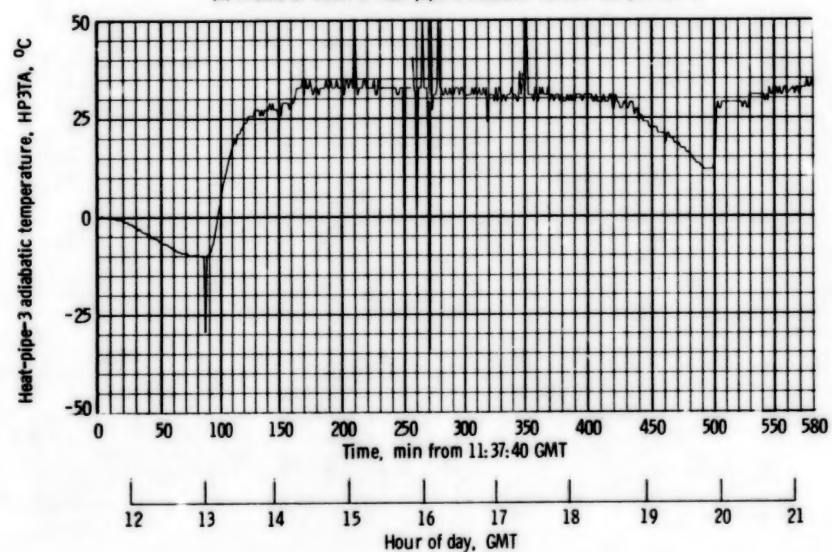
Figure 36. - Continued.



(g) Profile of VCHPS heat-pipe-1 adiabatic section temperature.

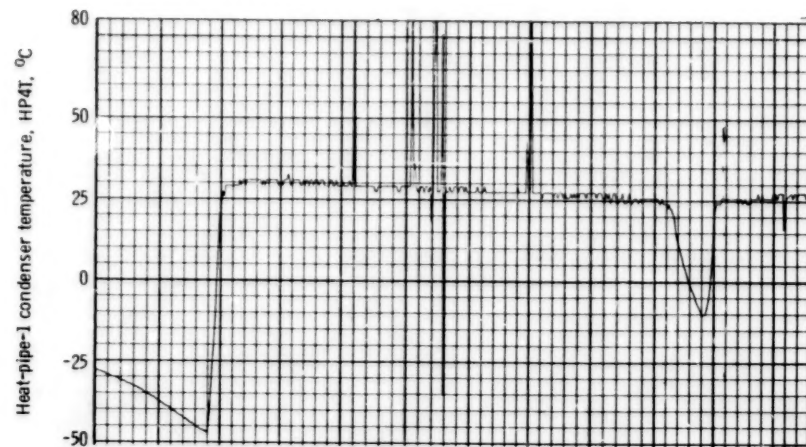


(h) Profile of VCHPS heat-pipe-2 adiabatic section temperature.

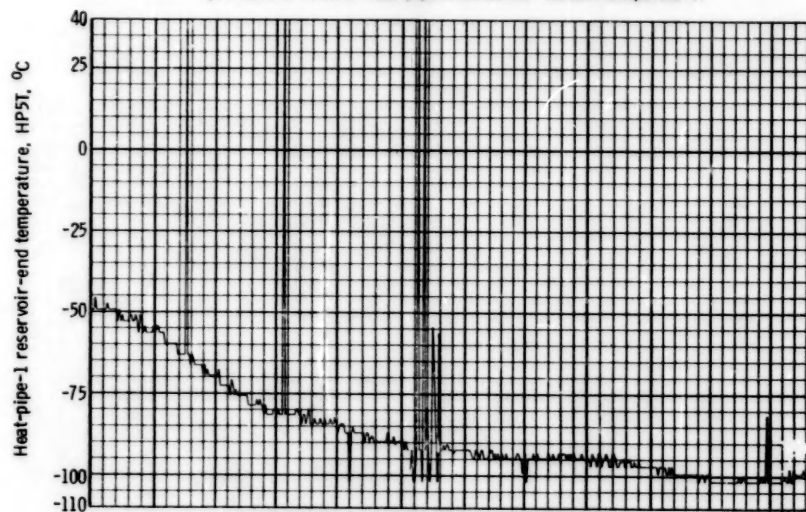


(i) Profile of VCHPS heat-pipe-3 adiabatic section temperature.

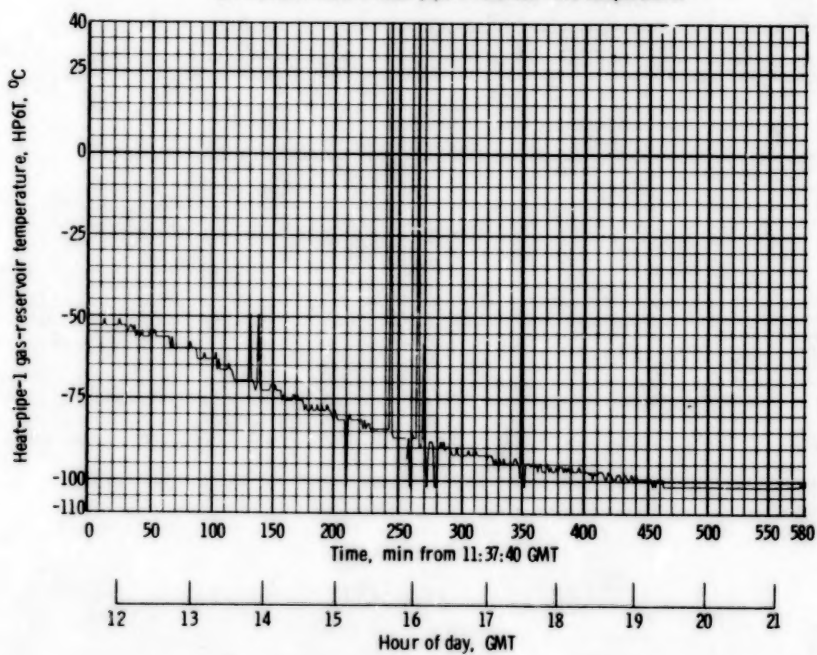
Figure 36. - Continued.



(j) Profile of VCHPS heat-pipe-1 condenser section temperature.



(k) Profile of VCHPS heat-pipe-1 reservoir-end temperature.



(l) Profile of VCHPS heat-pipe-1 gas-reservoir temperature.

Figure 36. - Concluded.

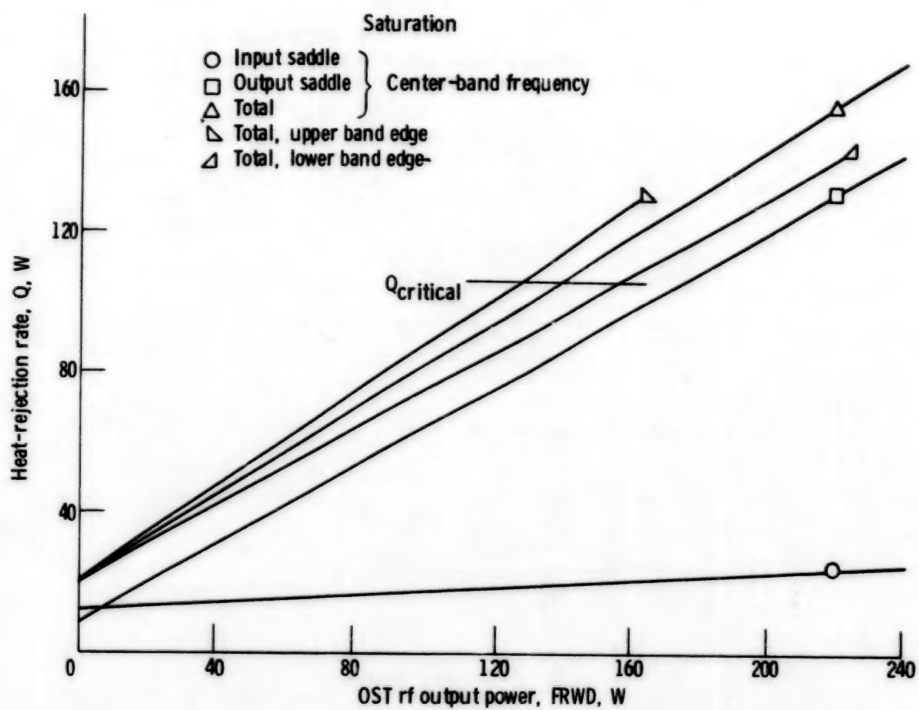
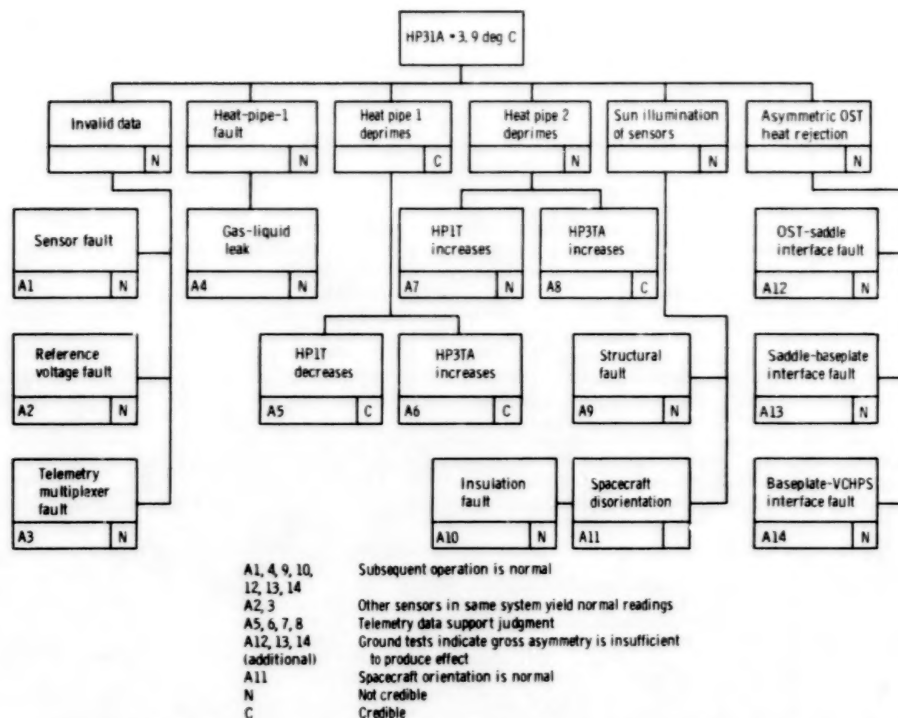
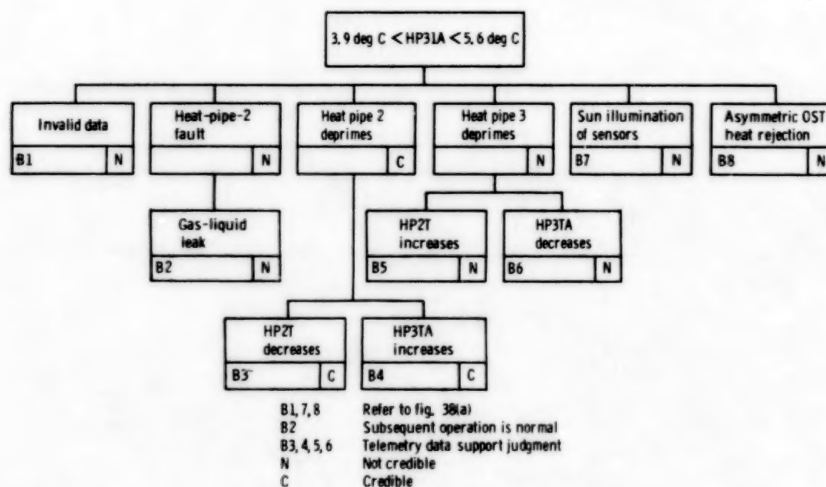


Figure 37. - CTS output-stage-tube body heat-rejection characteristics as function of rf output power.

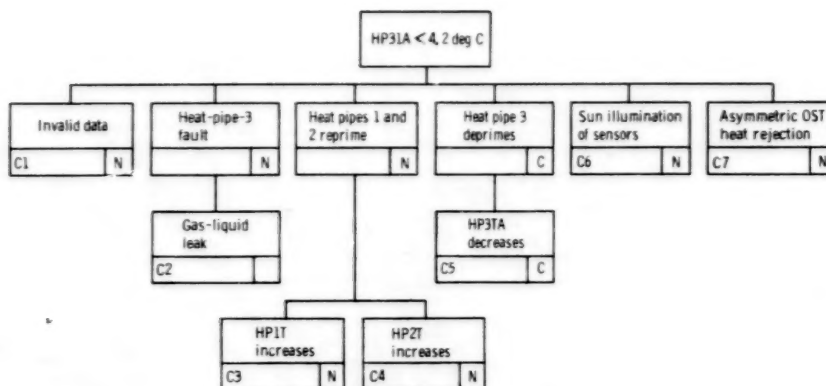


(a) Temperature difference HP31A, 3.9 degrees C. Approximate time, GMT: day 75, 15:46; day 82, 17:32; day 101, 17:31; day 253, 14:20.



(b) Temperature difference HP31A, 3.9 to 5.6 degrees C. Approximate time, GMT: day 75, 18:23; day 82, 17:51; day 101, 18:18; day 252, 14:31.

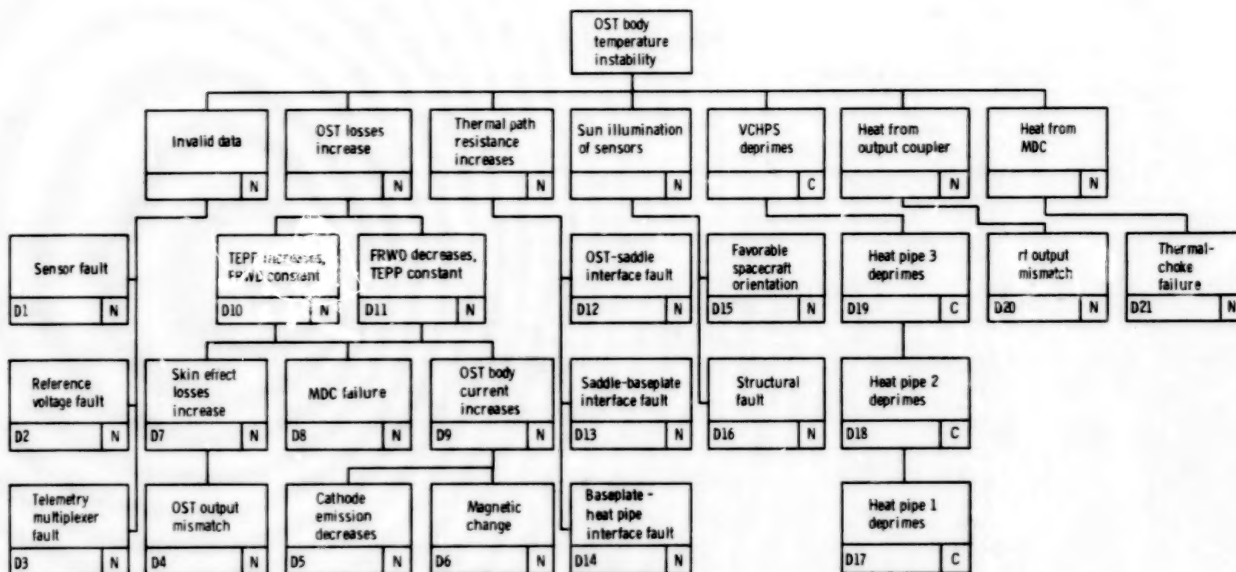
Figure 38. - Logic diagram for thermal-anomaly analysis of CTS transmitter experiment package.



C1, 6, 7
C2
C3, 4, 5
N
C

Refer to fig. 38(a)
Subsequent operation is normal
Telemetry data support judgment
Not credible
Credible

(c) Temperature difference HP31A, less than 4.2 degrees C. Approximate time, GMT: day 75, 19:25; day 82, 18:01; day 101, 18:43; day 253, 14:33.

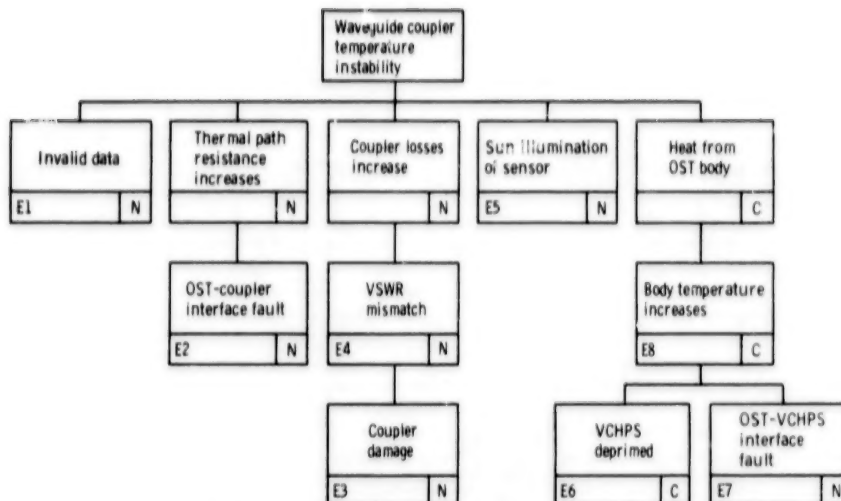


D1, 6, 12, 13, 14, 21
D2, 3
D17, 18, 19
D4-11, 20
D15
N
C

Subsequent operation is normal
Other sensors in same system yield normal readings
See figs. 38(a) to (c)
Telemetry data support judgment
Spacecraft orientation is normal
Not credible
Credible

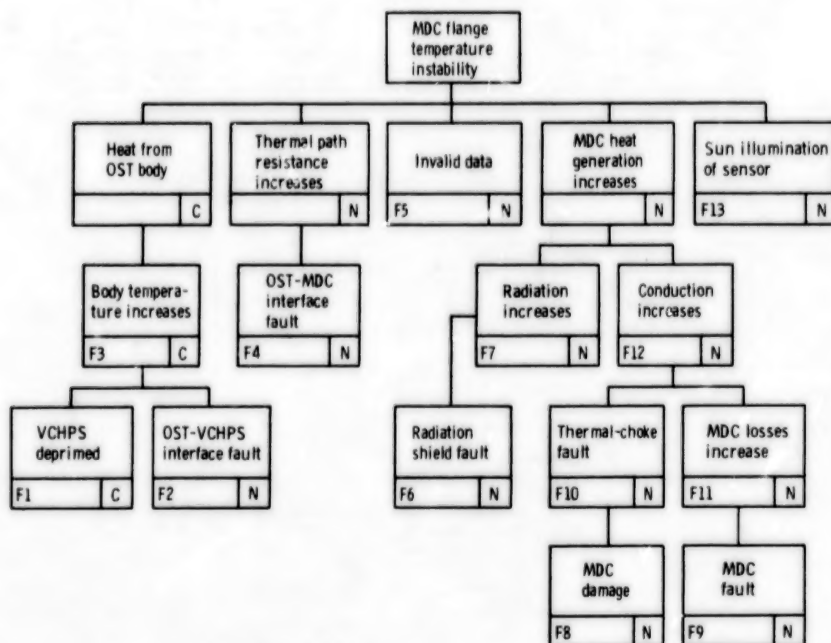
(d) OST body temperature instability. Approximate time, GMT: day 75, 19:25; day 82, 18:01; day 101, 18:43; day 253, 14:33.

Figure 38. - Continued.



E1, 5 See fig. 38(d)
 E2, 3, 7 Subsequent operation is normal
 E4 Telemetry data do not support judgment
 E6 See figs. 38(a) to (c)
 E8 Telemetry data support judgment; also see fig. 38(d)
 N Not credible
 C Credible

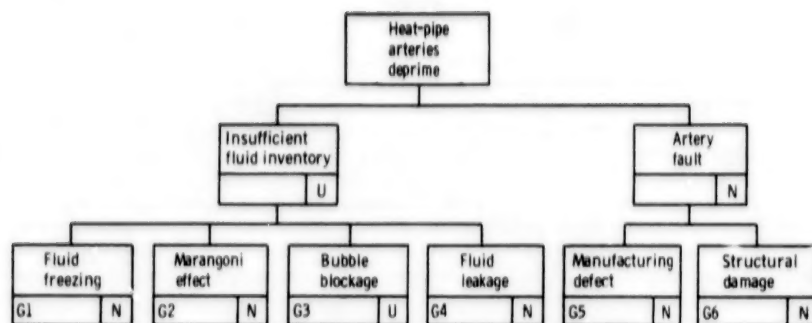
(e) Waveguide coupler temperature instability. Approximate time, GMT: day 75, 19:25; day 82, 18:01; day 101, 18:43; day 253, 14:33.



F1 See figs. 38(a) to (c)
 F2, 4, 6, 8, 9, 10 Subsequent operation is normal
 F3 Telemetry data support judgment; see also fig. 38(d)
 F5, 13 See fig. 38(d)
 F7, 12 MDC temperatures (other than flange) are normal
 F11 MDC voltages and currents are normal
 N Not credible
 C Credible

(f) MDC flange temperature instability. Approximate time, GMT: day 75, 19:25; day 82, 18:01; day 101, 18:43; day 253, 14:33.

Figure 38. - Continued.



- G1 Telemetry data indicate favorable temperatures except for day 253; depriming by this method has been demonstrated in a normal gravity field
- G2 Telemetry data indicate favorable temperature gradient; analysis (ref. 7) does not support as a significant factor
- G3 Telemetry data indicate favorable temperatures; limited experiments (ref. 7) do not support as a significant factor
- G4,6 Subsequent operation is normal
- G5 Intermittent malfunction (due to expansion, etc.) not supported by complete telemetry data review
- N Not credible
- C Credible
- U Unknown

(g) Heat-pipe arteries deprime.

Figure 38. - Concluded.

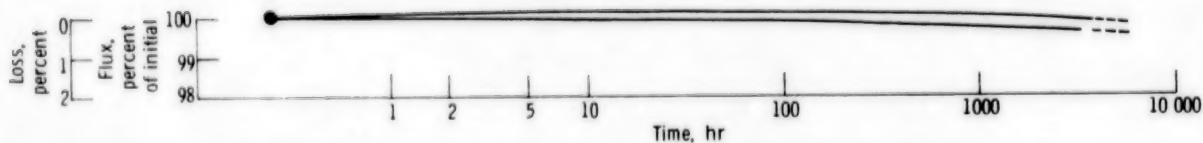


Figure 39. - Long-term aging of samarium-cobalt magnets after prestabilization. Magnet length-diameter ratio, 0.4; temperature, 150°C. (From ref. 9.)

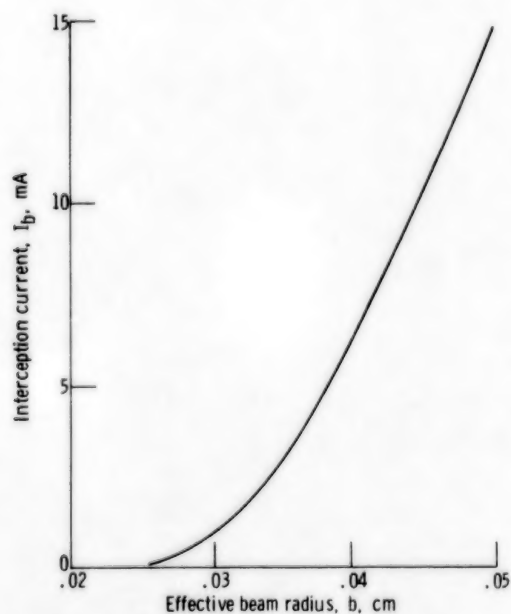


Figure 40. - Body current as function of effective beam radius.

1. Report No. NASA TP-1410		2. Government Accession No.		3. Recipient's Catalog No.	
4. Title and Subtitle THERMAL ANOMALIES OF THE TRANSMITTER EXPERIMENT PACKAGE ON THE COMMUNICATIONS TECHNOLOGY SATELLITE				5. Report Date April 1979	
				6. Performing Organization Code	
7. Author(s) Robert E. Alexovich and Arthur N. Curren				8. Performing Organization Report No. E-9735	
9. Performing Organization Name and Address National Aeronautics and Space Administration Lewis Research Center Cleveland, Ohio 44135				10. Work Unit No. 610-22	
				11. Contract or Grant No.	
12. Sponsoring Agency Name and Address National Aeronautics and Space Administration Washington, D. C. 20546				13. Type of Report and Period Covered Technical Paper	
				14. Sponsoring Agency Code	
15. Supplementary Notes APPENDIX B - TEMPERATURE EFFECTS ON FOCUS MAGNETS and APPENDIX C - THERMAL OUTPUT OF OST 2022R1 AND OST 2030, both by Denis J. Connolly					
16. Abstract <p>This report details an investigation of the causes of four temporary thermal-control-system malfunctions that gave rise to unexpected temperature excursions in the 12-gigahertz, 200-watt transmitter experiment package (TEP) on the Communications Technology Satellite. The TEP consists of a nominal 200-watt output stage tube (OST), a supporting power-processing system (PPS), and a variable-conductance heat-pipe system (VCHPS). The VCHPS, which uses three heat pipes to conduct heat from the body of the OST to a radiator fin, was designed to maintain the TEP at safe operating temperatures at all operating conditions. On four occasions during 1977, all near the spring and fall equinoxes, the OST body temperature and related temperatures displayed sudden, rapid, and unexpected rises above normal levels while the TEP was operating at essentially constant, normal conditions. The temperature excursions were all terminated without TEP damage by reducing the radiofrequency (rf) output power of the OST. Between the anomalies and since the fourth, the thermal control system has apparently functioned as designed. The results of the investigation indicate the most probable cause of the temperature anomalies is depriving of the arteries in the variable-conductance heat pipes. Further, a mode has been identified in which the TEP, as presently configured, may operate with stable temperatures and with minimum change in performance level.</p>					
17. Key Words (Suggested by Author(s)) Communications Technology Satellite Traveling wave tube Variable-conductance heat pipes				18. Distribution Statement Unclassified - unlimited STAR Category 17	
19. Security Classif. (of this report) Unclassified		20. Security Classif. (of this page) Unclassified		21. No. of Pages 112	
				22. Price* A06	

* For sale by the National Technical Information Service, Springfield, Virginia 22161

NASA-Langley, 1979

90

50

END

Sept. 14, 1979